

~~Volume 21, Number 5~~

November, 1966

~~Handwritten initials~~
JD

~~Handwritten initials~~
MCP
JT
66

NSD
LSD

SOVIET ATOMIC ENERGY

АТОМНАЯ ЭНЕРГИЯ
(ATOMNAYA ENERGIYA)

TRANSLATED FROM RUSSIAN



CONSULTANTS BUREAU

SOVIET ATOMIC ENERGY

Soviet Atomic Energy is a cover-to-cover translation of *Atomnaya Energiya*, a publication of the Academy of Sciences of the USSR.

An arrangement with Mezhdunarodnaya Kniga, the Soviet book export agency, makes available both advance copies of the Russian journal and original glossy photographs and artwork. This serves to decrease the necessary time lag between publication of the original and publication of the translation and helps to improve the quality of the latter. The translation began with the first issue of the Russian journal.

Editorial Board of *Atomnaya Energiya*:

Editor: M. D. Millionshchikov

Deputy Director, Institute of Atomic Energy
imeni I. V. Kurchatov
Academy of Sciences of the USSR,
Moscow, USSR

Associate Editors: N. A. Kolokol'tsov

N. A. Vlasov

A. I. Alikhanov

A. A. Bochvar

N. A. Dollezhal

V. S. Fursov

I. N. Golovin

V. F. Kalinin

A. K. Krasin

A. I. Leipunskii

V. V. Matveev

M. G. Meshcheryakov

P. N. Palei

V. B. Sherchenko

D. L. Simonenko

V. I. Smirnov

A. P. Vinogradov

A. P. Zefirov

Copyright © 1967 Consultants Bureau, a division of Plenum Publishing Corporation, 227 West 17th Street, New York, N. Y. 10011. All rights reserved. No article contained herein may be reproduced for any purpose whatsoever without permission of the publishers.

Subscription
(12 Issues): \$95

Single Issue: \$30
Single Article: \$15

Order from:



CONSULTANTS BUREAU

227 West 17th Street, New York, New York 10011

SOVIET ATOMIC ENERGY

A translation of *Atomnaya Énergiya*

Volume 21, Number 5

November, 1966

CONTENTS

	Engl./Russ.	
Interaction of Fast H_1^+ Ions with Metal Surfaces in Very High Vacuum - E. S. Borovik, N. P. Katrich, and G. T. Nikolaev	1019	339
Method of Calculating the Intensity of Back-Scattered γ -Radiation - B. P. Bulatov	1026	345
Limiting Current Density in a Linear Ion Accelerator - A. V. Zotov and V. A. Teplyakov	1034	356
Use of the Calculated-Expense Method for Choosing The Characteristics of a Fast Reactor - V. B. Lytkin, M. F. Troyanov, and A. I. Novozhilov	1039	360
IR-100 Research and Training Reactor - Yu. M. Bulkhin, A. D. Zhirnov, G. N. Zhemchuzhnikov, L. V. Konstantinov, V. A. Nikolaev, I. A. Stenbok, V. S. Lobanov, N. A. Khryastov, and A. G. Filippov	1042	363
Evaporation Rates of Cathodes Made of Uranium Carbide, Zirconium Carbide, and their Solid Solutions - B. S. Kul'varskaia	1047	368
Formation of Polymer Products in the Radiolysis of Mixtures of Hexafluorobenzene with Perfluorocyclohexane and Perfluorononane - V. A. Khramchenkov	1054	375
Changes in the Properties of Ion Exchangers After Prolonged Use in the Purification of Radioactive Waste Water - F. V. Rauzen and Z. Ya. Solov'eva	1058	378
ABSTRACTS		
Propagation of Capture γ -Radiation in a Uniform Spherical Shield - B. K. Fedyushin ...	1062	382
Approximate Solution of the Dynamic Equations of a Nuclear Reactor - N. G. Chelintsev	1064	383
Solution of the Diffusion Equation in Periodic Lattices in Terms of Trigonometric Series - G. Ya. Rummyantsev	1064	384
A Very Simple Mathematical Model for Studying the Dynamics of Self-Regulating Water-Cooled Water-Moderated Reactors - F. M. Mitenkov, B. I. Motorov, and É. A. Motorova	1065	385
Improved System of Stationary Dosimetric Monitoring at the VVR-M Reactor - E. A. Kononov, L. M. Ploshchanskii, and V. A. Solov'ev	1067	386
Calculation of the Absorption of Epithermal Neutrons in an Infinite Lattice of Absorbing Slabs - V. N. Gurin	1068	386
LETTERS TO THE EDITOR		
Possibilities of the Photonutron Method for Determining Hydrogen in Heavy Metals - N. P. Mazuykevich and V. A. Shkoda-Ul'yanov	1069	388
Calculating Photoelectric Attenuation Coefficients for Gamma Radiation - O. S. Marenkov	1071	389
Neutron Yield Curve for a Tritium Target - L. N. Katsaurov and A. N. Kuznetsov	1073	390
Angular Distribution of Fast Neutrons Emerging from a Medium which Contains Hydrogen - S. F. Degtyarev, V. I. Kukhtevich, A. P. Suvorov, V. V. Tarasov, V. K. Tikhonov, and S. G. Tsypin	1076	392

CONTENTS

(continued)

	Engl./Russ.	
Passage of Fast Neutrons Through Thick Layers of Lithium Hydride - G. M. Bozin, S. F. Degtyarev, V. I. Kukhtevich, B. I. Sinitsyn, V. B. Staroverov, V. K. Tikhonov, and S. G. Tsypin	1079	394
Build-up Factor of Fast Neutrons Versus the Relative Positions of Shielding and Detector - S. F. Degtyarev, V. I. Kukhtevich, V. K. Tikhonov, and S. G. Tsypin ...	1081	395
Passage of Gamma Rays Through Spherical and Cylindrical Shielding Barriers - A. V. Larichev, O. F. Partolin, E. D. Chistov, and O. M. Zараev	1084	398
Yields of Nuclear Reactions for Making Na ²² in a Cyclotron - N. N. Krasnov and P. P. Dmitriev	1087	400
Effect of Accelerating Voltage on Intensity in the Dubna Synchrocyclotron - V. I. Danilov, I. B. Enchevich, E. A. Polferov, and A. N. Safonov	1089	402
Determination of Accelerator Perturbations from Information on Particle Loss Distribution - I. P. Karabekov	1092	404
Effective Method of Performing Multigroup Reactor Calculations - V. V. Khromov and A. M. Kuz'min	1095	406
Calculating the Doppler Temperature Coefficient of Reactivity for Homogeneous Reactors - F. M. Mitenkov, B. A. Averbakh, L. M. Gorbunov, and O. B. Samoilov	1098	408
Effectiveness of a System of Control Rods Distributed Through a Reactor Core and Reflector - V. I. Nosov	1101	410
Semiconductor (Germanium) γ -Ray Spectrometer Determines Burnup in Fuel Elements - L. V. Groshev, A. M. Demidov, G. A. Kotel'nikov, and O. A. Miller	1104	412
Fluorite Activation Analysis Assay in Ore Samples and in Ore Beneficiation Products - V. I. Prokopchik and T. I. Subbotina	1108	415
Vapor-Phase Chromatographic Separation and Gamma-Ray Spectrometric Analysis of Gaseous Effluents of the VVR-M Reactor - V. A. Solov'ev, O. V. Stepanets, and V. D. Trenin	1110	417
 NEWS OF SCIENCE AND TECHNOLOGY		
[Conference of Experts on Microbiological Problems in Irradiation Preservation of Foodstuffs - N. N. Mazokhina		419]
All-Union Conference on Phase Diagrams of Metallic Systems - I. A. Markova	1113	420
Soviet Delegation Visits Canada - E. Kulish		422]
[Nucleonic Instrumentation at the British Industrial Exhibit in Moscow - Yu. K.		425]
 BRIEF COMMUNICATIONS		
[Third International Congress on Radiation Research		426]
Soviet Scientists Visit Radiobiological Centers in the USA		426]
British Scientists Visit the USSR	1116	426
 BOOK REVIEWS		
K. Röhrdanz - Nuclear Engineering in a Nutshell	1117	427
Proceedings of the Third International Conference on the Peaceful Uses of Atomic Energy, Vol.2, Reactor Physics - Reviewed by Yu. I. Mityaev	1117	427
A. B. Clegg - High Energy Nuclear Reactions	1118	427
D. C. Layman and G. Thornton - Remote Handling of Mobile Nuclear Systems - Reviewed by M. Orlov	1119	427
Criticality Control of Fissile Materials - Reviewed by Yu. K.	1120	428
Radioisotope Instruments in Industry and Geophysics - Reviewed by L. P.	1120	428
Radioisotope Sample Measurement Techniques in Medicine and Biology - Reviewed by Yu. V. Sivintsev	1122	430

CONTENTS

(continued)

	Engl./Russ.	
Radioisotopes in Endocrinology. First Anniversary of the Society for Nuclear Medicine in Freiburg im Breisgau, October 17-19, October 1963	1124	431
Dosimetry of Ionizing Radiations (Basic Concepts and their Terminology) USSR Academy of Sciences, Committee on Scientific and Technical Terminology. Collections of Recommended Terms. No.70	1124	431
J. S. Strettan - Ionizing Radiations	1125	431
G. W. Reed - Proceedings of the International "Enrico Fermi" School of Physics Course XXX - Radiation Dosimetry - Reviewed by Yu. V. Sivintsev	1125	431
E. I. Vorob'ev et al. Radiobiology and Clinical Radiology. Proceedings of the Central X-Ray and Radiological Scientific Research Institute. Volume V	1126	432
Rules and Regulations for Safe Transportation of Radioactive Materials. Revised 1964 Edition. No.6 in Series on Safety	1127	432
ERRATA	1128	

NOTE

The Table of Contents lists all material that appeared in the original Russian journal. Items originally published in English or generally available in the West are not included in the translation and are shown in brackets. Whenever possible, the English-language source containing the omitted items is given.

The Russian press date (podpisano k pechatu) of this issue was 10/29/1966. Publication therefore did not occur prior to this date, but must be assumed to have taken place reasonably soon thereafter.

INTERACTION OF FAST H_1^+ IONS WITH METAL SURFACES IN VERY HIGH VACUUM

E. S. Borovik, N. P. Katrich,
and G. T. Nikolaev

UDC 532.6:533.9

The results of experiments on the interaction of fast hydrogen ions (H_1^+) with metals forming weak chemical bonds (nickel, stainless steel) and metals forming strong chemical bonds (tantalum and titanium) with hydrogen are presented. The weighing method was used under very-high vacuum conditions to determine the sputtering coefficient α of stainless steel bombarded by 35-keV H_1^+ ions and the penetration coefficient η of H_1^+ ions entering the stainless steel ($\alpha = 9 \cdot 10^{-3}$, $\eta = 0.5$ for hydrogen concentrations greatly exceeding 10^{19} atoms/cm²). The variation of η with the density of the hydrogen introduced and the temperature of the metals was determined by the pressure-variation method. The results indicate that metals of the titanium type are suitable for use in capturing fast hydrogen atoms in magnetic traps.

The collision of fast particles with metal surfaces is accompanied by three main processes: the desorption of adsorbed gases, the atomization or sputtering of the metals, and the penetration of fast particles into the metals. In magnetic traps, the desorption of adsorbed gases and the sputtering of the metals leads to contamination of the plasma, while the penetration of the fast particles has a favorable influence, since under certain conditions this may lighten the burden of the pumping system.

Many papers have been written on the sputtering of metals, but so far no one has measured the sputtering coefficient of metals under very-high vacuum conditions.

The penetration of hydrogen ions H_1^+ and D_1^+ was studied in [1, 2], but the results were not in agreement. The difference was as follows. The penetration coefficient of D_1^+ ions found in [1] was 0.2 to 0.35 for incident particles of energy 7 to 25 keV. For a concentration of $3 \cdot 10^{17}$ hydrogen atoms/cm² in stainless steel, saturation set in, this being defined by the authors as the condition in which the flows of hydrogen into and out of the target were equal. The penetration coefficient of H_1^+ ions obtained in [2] was 0.9, no saturation being observed up to a concentration of $2 \cdot 10^{19}$ cm⁻².

Since the number of hydrogen atoms introduced into the metal may exceed 10^{19} (according to [2]), there is a distinct possibility of determining the penetration factor gravimetrically. We employed this method to measure the sputtering coefficient α of stainless steel bombarded by 35-keV H_1^+ ions and the penetration coefficient η of the H_1^+ ions into the steel; we also studied the variation of the penetration coefficient of H_1^+ ions into titanium, tantalum, nickel, and stainless steel with the temperature of the target bombarded and the density of the hydrogen thus introduced.

DETERMINATION OF α AND η GRAVIMETRICALLY

The apparatus on which our experiments were conducted consisted of a system of hydrogen and helium condensation pumps (HCP and HeCP respectively), a high-frequency ion source, and a measuring chamber. The heated measuring chamber was assembled with copper gaskets. A detailed description of the apparatus is given in [2].

Figure 1 shows the arrangement of the measuring chamber. The chamber was degassed by heating to approximately 600°C for 3 h. The stainless steel target, 1.5 g in weight, already mechanically polished, was washed in gasoline, then in alcohol, and fixed in the holder 1. The target holder was insulated from the measuring chamber by means of a glass junction, which enabled the ion current to be

Translated from *Atomnaya Energiya*, Vol. 21, No. 5, pp. 339-345, November, 1966. Original article submitted May 1, 1966.

TABLE 1. Values of the Coefficients η and α

N_0	Δp_t	Δp_c	N_1	η	α
$3.8 \cdot 10^{19}$	$+2 \cdot 10^{-6}$	$+3 \cdot 10^{-5}$	$1.85 \cdot 10^{19}$	0.49	$9 \cdot 10^{-3}$
$2.1 \cdot 10^{19}$	$+2 \cdot 10^{-6}$	$+1.6 \cdot 10^{-5}$	$1 \cdot 10^{19}$	0.48	$8.5 \cdot 10^{-3}$
$3.4 \cdot 10^{19}$	$+1 \cdot 10^{-6}$	$+2.7 \cdot 10^{-5}$	$1.7 \cdot 10^{19}$	0.5	$9 \cdot 10^{-3}$

Note: N_0 is the number of ions striking the target; N_1 is the number of ions entering into the target.

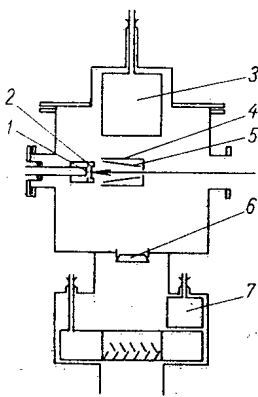


Fig. 1. Arrangement of measuring chamber: 1) target holder; 2) target; 3), 7) hydrogen condensation pumps; 4) screen; 5) collector; 6) metal valve.

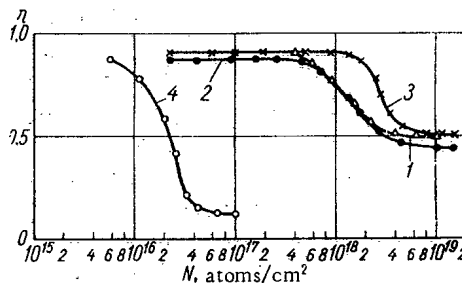


Fig. 2. Variation of η with the density of the hydrogen penetrating into stainless steel.

measured directly during the bombardment of the target. The target was heated to about 600°K at the same time as the measuring chamber. The aluminum-foil collector 5 was protected from the scattered ion beam by screen 4 and heated to about 500°K by thermal radiation from the chamber walls. The weight of the collector was ~ 0.5 g. Evacuation of the measuring chamber during the degassing period was effected by HCP-2. At the conclusion of the heating period the vacuum reached $\sim 1 \cdot 10^{-7}$ mm Hg. After heating, liquid helium was poured into the HeCP and liquid hydrogen into HCP-1; then the measuring chamber was disconnected from HCP-2 by means of the heated metal valve 6. In this way the vacuum in the measuring chamber was brought up to $5 \cdot 10^{-10}$ mm Hg.

The 35-keV H_1^+ ion beam was recorded electrically, using the cutoff potential applied to the collector 5. The ion-beam current was usually 100 to $150 \mu\text{A}$. The sputtered target metal was collected by the collector.

The target and collector were weighed on microanalytical balances. Experiments showed that as a result of the first heating to 600°K in a vacuum of $1 \cdot 10^{-7}$ mm Hg, the weight of a freshly prepared target fell very slightly. The weight of the collector fell rather more, apparently because of its greater surface area. On subsequent heating, the weight of the target and collector remained constant (within weighing accuracy): $\pm 1 \cdot 10^{-6}$ g for the target and $\pm 3 \cdot 10^{-6}$ g for the collector. No effect of atmospheric moisture was noticed (within weighing accuracy); the weight of the target and collector remained constant for much longer than was needed for repeated weighing.

The values of α and η were calculated from the formulas

$$\alpha = \frac{\Delta p_c}{9.3 \cdot 10^{-23} \frac{i}{q} t}; \quad (1)$$

$$\eta = \frac{\Delta p_c + \Delta p_t}{1.67 \cdot 10^{-24} \frac{i}{q} t}; \quad (2)$$

where Δp_c is the change in the weight of the collector in g, Δp_t is the change in the weight of the target in g, i is the ion beam current in A, q is the charge on an electron in C, t is the time of target bombardment in sec, $9.3 \cdot 10^{-23}$ g is the weight of an iron atom, and $1.67 \cdot 10^{-24}$ g is that of a hydrogen atom.

The measured values of α and η are shown in Table 1.

We see from the table that the over-all change in weight is an order greater than the measuring error. The gravimetrically obtained sputtering coefficient of stainless steel due to 35-keV H_1^+ ions equals $9 \cdot 10^{-3}$, while η equals 0.5, much smaller than the penetration coefficient found in [2].

In calculating α and η , the absorption of residual gases by the sputtered metal and the desorption of gases from the target due to ion bombardment were not considered. As regards the absorption of background gases by the sputtered metal, for gas pressures of $\sim 5 \cdot 10^{-10}$ mm Hg this is not very important. In order to determine the quantity of gas desorbed from the target during bombardment, we made some additional experiments. The method was as follows. The gas desorbed from the target by the H_1^+ ions was adsorbed on the surface of the HCP. Since the pumping rate of the HCP for the residual gases was 100 times that of the HeCP operating through a hole in the target chamber, we may consider that nearly all the residual gases were pumped out by the HCP. After the elapse of a certain period of target bombardment, the liquid hydrogen was taken from the HCP 3 and the bombardment was stopped at the same time. Since each gas had its own desorption temperature, on heating the HCP-1 the vacuum in the target chamber varied in accordance with the quantity and type of the desorbed gas. The total quantity of heavy gases desorbed from the target equalled 1 to 1.5 $cm^3 \cdot mm$ Hg, which could not seriously affect the value of η .

Thus the results of the weighing showed that the sputtering coefficient of stainless steel corresponding to 35-keV H_1^+ ions equalled $9 \cdot 10^{-3}$, and the penetration coefficient of the same ions passing into the steel was 0.5. Although this value is quite high, it is much smaller than that given by the varying-pressure method in [2]. The density of the hydrogen penetrating into the stainless steel (found gravimetrically) was much greater than 10^{19} atoms/cm², which agrees closely with the results of the varying-pressure method.

Attempts to match the gravimetric data on η with the data obtained in [2] by allowing for the desorption of gases from the target during bombardment were unsuccessful. In later investigations, which will be published in a separate paper, it was found that the hydrogen in the target chamber was mainly in the molecular state, not in the atomic state, as indicated in [2]. Allowing for this fact alters the computing formula, doubling the quantity of nonpenetrating hydrogen, and giving a value of ~ 0.8 for η . This is clearly insufficient to make the results agree. We therefore considered that an error might have been made in calibrating the Bayard-Alpert ionization manometer (which was based on the LM-2 type). This question is considered later.

MEASURING η BY THE VARYING-PRESSURE METHOD

As indicated earlier, in measuring the value of η by the method of varying pressure, a mistake was made in the calculation, owing to the fact that the hydrogen evolved from the target during bombardment was in the molecular and not the atomic state as indicated in [2]. Accordingly the computing formula for the penetration coefficient will have the form

$$\eta = 1 - \frac{2n(p-p_0)w}{760iq} \quad (3)$$

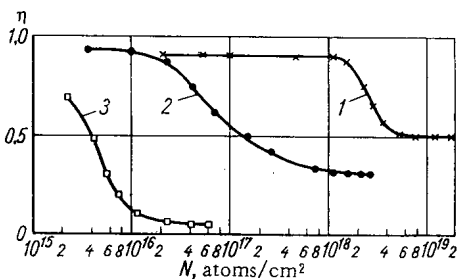


Fig.3. Variation of η with the density of the hydrogen penetrating into nickel.

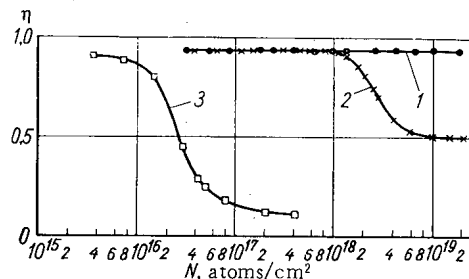


Fig.4. Variation of η with the density of the hydrogen penetrating into titanium.

where n is the number of H_2 molecules in 1 dm^3 under normal conditions, p_0 is the initial pressure in mm Hg, p is the working pressure in mm Hg, w is the rate of pumping hydrogen from the chamber in dm^3/sec , i is the H_1^+ ion-beam current in A, q is the charge of an electron in C, and 760 mm Hg is atmospheric pressure. The factor of 2 accounts for the evolution of H_2 from the target.

In order to investigate the possible error in determining the pressures p_0 and p , we measured the penetration coefficients by using a standard IM-12F ionization manometer specially intended for measuring pressures in heated systems. Since the sensitivity of the ionization manometers was only half as good for hydrogen as for nitrogen [4], the readings of the IM-12F manometer were adjusted accordingly. For large concentrations of hydrogen in the metal ($> 10^{19}$ atoms/ cm^2), the value of η calculated from formula (3) agreed with the penetration coefficient determined gravimetrically, i. e., with 0.5 and not 0.9. The variation of η with the concentration of hydrogen penetrating into the metal is shown in Fig. 2 (curve 2). In addition to this, we made some experiments to verify the characteristics of the ionization manometer used in [2]. This manometer was based on a standard LM-2 ionization manometer intended for measuring pressures in the range 10^{-3} to $5 \cdot 10^{-8}$ mm Hg. The initial sensitivity of this instrument was half that of the LM-2, and the linear range of the characteristic, recalculated in accordance with the sensitivity and the fall in the photocurrent to the collector, was $5 \cdot 10^{-10}$ mm Hg. On comparing the characteristics of this manometer with those of the standard IM-12F and LM-2 ionization manometers, it was found that its sensitivity was three times worse than that determined earlier, and the linear range of the characteristic lay in a narrower range of measured pressures.

The results of [2], recalculated to incorporate corrections for sensitivity and the nonlinearity of the characteristic of the ionization manometer in the high-vacuum region, are shown in Fig. 2 (curve 1). We see that the recalculated results agree quite well with those based on the IM-12F (see curve 2). Since the quantity of hydrogen not penetrating into the metal increases with falling η , the correction for the evacuation of hydrogen by the HCP for concentrations $> 4 \cdot 10^{17} \text{ cm}^{-2}$ diminishes considerably. Taken together with the nonlinearity of the ionization-manometer characteristic under high vacuum, this explains the disproportionate fall in the η/N (cm^{-2}) curve after recalculation in the regions of small and large hydrogen concentrations.

Later it proved possible almost entirely to avoid the necessity of allowing for the rate of hydrogen evacuation by the HCP. The measuring procedure reduced to the following. Immediately after beginning the measurements, the H_1^+ ion beam was defocused, and the HCP was saturated on account of the hydrogen dissipated in the chamber, the area of the pumping surface of the pump being considerably reduced.

VARIATION OF η WITH THE DENSITY OF THE HYDROGEN PENETRATING INTO THE METAL AND WITH THE TARGET TEMPERATURE

A knowledge of the temperature dependence of the capture and retention of fast hydrogen ions may provide useful information on the state of hydrogen in metals, which is of interest in connection with a number of applications.

We studied the variation of η with the density of the hydrogen in the metal and with the target temperature by the variable-pressure method, using formula (3) for the calculations. The pressure was

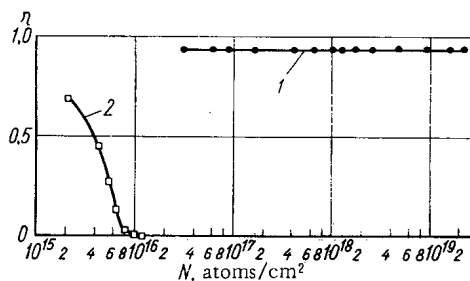


Fig. 5. Variation of η with the density of the hydrogen penetrating into tantalum.

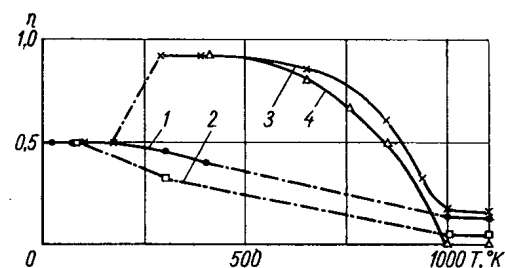


Fig. 6. Variation of η with the temperature of the metal.

measured with an IM-12F manometer designed for measuring vacuum in heated systems. The manometer was placed inside the target chamber. Prior to the measurements, as before, the chamber and target were heated to $\sim 600^\circ\text{K}$ for 3 h. The 35-keV H_1^+ hydrogen-ion beam was recorded electrically, using a cutoff voltage applied to the HCP surrounding the target. The area of target surface bombarded by the ions was determined visually from the erosion traces on the target. Traces of erosion were clearly visible on all the metals studied up to about 300°K . For target temperatures above 300°K there were no noticeable traces of erosion. For temperatures above 300°K the area of the bombarded surface was therefore taken as equal to that measured at lower temperatures for the same settings of the ion source and focusing system.

In order to study the interaction of the hydrogen ions with the metals, we chose two types of metal: those forming weak chemical bonds with hydrogen (nickel and stainless steel) and those forming strong bonds (titanium and tantalum). The penetration of hydrogen ions into stainless steel at normal and low temperatures was studied with targets constituting hollow argon-arc-welded boxes. The thickness of the target walls was 1 mm. The target was insulated from the chamber by glass junctions, so that the ion beam current was recorded continuously. During the experiment, the back of the box was cooled with running water or liquid nitrogen passed through the hollow part of the box. The target was polished mechanically and washed in gasoline and alcohol. Electrolytic polishing of the targets, carried out after mechanical polishing, with subsequent washing in distilled water, had very little effect on the results of the measurements.

Curve 2 of Fig. 2 was obtained for a stainless-steel target cooled by running water to 300°K ; curve 3 was obtained for a target cooled to 78°K with liquid nitrogen. In addition to this, we measured η with a target cooled by liquid hydrogen, for which the target construction was slightly modified. The results of measurements at 24 to 78°K were almost identical. We see from the curves that the results obtained with a normal target temperature differed considerably from those obtained at low temperatures, both in the value of η and in the hydrogen density which η began falling.

Investigations were carried out at high temperatures with thin targets (0.1 to 0.2 mm), carefully degassed by ohmic heating at temperatures close to the melting point. The target temperature was calculated from the thermal-radiation formula. Degassing at these temperatures was stopped when the evolution of gas from the target became insignificant. After this the target temperature was reduced to some 1100 or 1200°K , liquid hydrogen was poured into HCP-1, and the degassing of the target by ionic bombardment began. This was necessary because even the long and continuous degassing at temperatures near the melting point was insufficient to degas any of the metals under examination completely. This was proved by the fact that on bombarding the target after thermal degassing there was a fall in the gas-evolution coefficient with rising number of ions striking the target. The gas-evolution coefficient became constant after the density of the ions striking the target exceeded $(1 \text{ to } 5) \cdot 10^{18} \text{ cm}^{-2}$. Analysis of the gases desorbed by ion bombardment at these temperatures was not carried out. In view of the fact that these gases were clearly recorded by the ionization manometer, despite the HCP surrounding the target, it was reasonable to suppose that these were gases condensing poorly (or not at all) at 20.4°K . This suggests hydrogen. We should not that the total amount of gases evolving from stainless steel and nickel as a result of this procedure was greater than that indicated in [4]. After degassing by ion bombardment, a further brief degassing at a temperature close to the melting point was carried out. After the target had been prepared in this way, the variation of η with the density of the hydrogen penetrating into the metal was measured. The results obtained for stainless steel at a target temperature around 1100°K are shown in Fig. 2. (curve 4). Measurements at higher temperatures involved difficulties which have not yet been overcome.

Figure 3 shows the results of measurements for nickel. Curves 1 and 2 were obtained on targets cooled with liquid nitrogen (to 78°K) and running water (to 300°K) respectively. We see that, for normal temperatures of the nickel target, the curve lines much lower than the corresponding curve for stainless steel (see Fig. 2). At low temperatures the curves for nickel and stainless steel are practically identical. Curve 3 in Fig. 3 was obtained for a thin target (0.025 mm) at about 1100°K .

The measurement of η as a function of hydrogen density in titanium at normal and low temperatures was carried out in the same way as for stainless steel, using targets constructed in a special box-like form, cooled with running water or liquid nitrogen. In addition to this, we made measurements on a target cooled by mechanical contact with the HCP. In this case the target temperature was estimated as approximately 200°K . Curve 2 in Fig. 4 was obtained by cooling the titanium target with liquid nitrogen to 78°K .

The curve for 200°K differed very little from this latter, and accordingly it is not shown in the figure. It should be noted that the fall in the penetration coefficient of H_1^+ ions penetrating into titanium begins at rather lower hydrogen concentrations than in the case of stainless steel or nickel. Curve 1 in Fig. 4 was obtained on cooling the target with running water to 300°K. It is an interesting point that the value of η remains unchanged over the range of hydrogen concentrations considered. Similar results were obtained for a target temperature of 400°K. The value of η fell as the temperature rose further. Curve 3 was obtained for a thin target (0.025 mm) heated to about 1100°K.

Figure 5 shows the results of measurements made with tantalum. Curve 1 was obtained at a temperature of ~400°K. Curve 2 was obtained at 1200°K on a thin target (0.025 mm thick). No measurements were made at low temperatures.

It follows from Figs. 2 to 4 that, at low temperatures, the curves are practically the same for all the metals studied. The difference between metals forming weak and strong chemical bonds with hydrogen is that at low temperatures the value of η for metals forming strong chemical bonds with hydrogen begins to fall at rather lower hydrogen concentrations. This is probably due to the presence of a large quantity of dissolved gases in these metals. At normal temperatures, no fall in η is observed for titanium and tantalum over the concentration range studied, whereas for metals forming weak chemical bonds with hydrogen the value of η falls at hydrogen concentrations of about $1 \cdot 10^{19} \text{ cm}^{-2}$ (by a factor of 2 for stainless steel and 3 for nickel). At high temperatures and low hydrogen concentrations in the metal, the value of η falls sharply (to between 0 and 0.15) for all the metals studied. As shown by the figures, complete target saturation with hydrogen at high temperatures only occurs for tantalum. We see from the curves that the variation of the penetration coefficient with temperature differs for different hydrogen concentrations. Figure 6 shows the η/T relationship for stainless steel, nickel, titanium, and tantalum (curves 1, 2, 3, and 4) in the range corresponding to large concentrations of hydrogen (after the fall in the value of η). The broken (dot-dash) lines show the temperature ranges not studied. It should be noted that the experiments on titanium and tantalum at $400 < T < 1000^\circ\text{K}$ were carried out with carefully-degassed thin targets (~0.025 mm), without ohmic heating of the target during measurement. The target was only heated by the action of the bombarding ions. The procedure for preparing the targets for measurement was described earlier; the temperature was calculated from the thermal-radiation formula.

DISCUSSION OF RESULTS

Our study of the interaction of H_1^+ ions with metals has shown that the penetration coefficient depends substantially on the density of the hydrogen penetrating into the metal, as well as on the temperature and nature of the metal. The greatest value of η occurs for metals forming strong chemical bonds with hydrogen. Although the limiting (saturation) gas capacity with respect to hydrogen was not reached for any of the metals studied (except at high temperatures), the experimental values of η indicated that metals forming strong chemical bonds with hydrogen had the greatest values of this capacity. The unusually high concentration of absorbed hydrogen ($\sim 2 \cdot 10^{19} \text{ atoms/cm}^2$), naturally, cannot be explained on the basis of a simple representation of the penetration mechanism, such as the simple accumulation of absorbed atoms in a layer of metal equal in thickness to the free path of the fast particles. It is well known [3] that the free path of 35-keV protons in metals is $\sim 10^{-5} \text{ cm}$. It is not hard to calculate that for concentrations of absorbed hydrogen equal to $10^{19} \text{ atoms/cm}^2$ the volume concentration would be $10^{24} \text{ atoms/cm}^3$, i. e., 10 times greater than the concentrations of the metal atoms. Clearly this concentration is impossible, even for metals forming strong chemical bonds with hydrogen [4]. At temperatures $> 300^\circ\text{K}$ this phenomenon may be explained by the ordinary diffusion of the absorbed hydrogen into the metal. In fact, if we suppose that, in the course of bombardment, a hydrogen concentration of $\sim 10^{15} \text{ atoms/cm}^2$ is created in the metal, in a layer $dx = 10^{-6} \text{ cm}$, at a depth equal to the free path of the H_1^+ ions (this is quite acceptable), then the flow of hydrogen through a plane at a distance $d = 10^{-3} \text{ cm}$ from the layer dx may be determined from the formula

$$q = DC \frac{1}{d}, \quad (4)$$

where D is the diffusion coefficient of the hydrogen atoms and C is their concentration. For a concentration of $\sim 10^{15} \text{ atoms/cm}^2$ the volume concentration will equal $\sim 10^{21} \text{ atoms/cm}^3$. The diffusion coefficient for stainless steel may be taken as $10^{-9} \text{ cm}^2/\text{sec}$ [5], so that $q = 10^{15} \text{ atoms/sec}$, which approximately equals the flow of ions to the target.

Whereas at above 300°K the results obtained may be explained by ordinary diffusion of the absorbed hydrogen into the metal, this explanation is completely inadequate at low temperatures. Modern views on the diffusion of gases in metals indicate an exponential relationship between the diffusion coefficient and temperature $D \sim e^{-E/RT}$; hence at low temperatures the diffusion of gases in metals should be almost negligibly small. We should thus expect that when hydrogen ions H_1^+ penetrate into metals at low temperatures the concentration of hydrogen in the surface layer will very quickly reach such a value that the penetration coefficient will fall to zero. At high temperatures the penetration coefficient will also equal zero at certain concentrations, but this time on account of the high diffusion velocity of the hydrogen. At high temperatures the expected results were in fact obtained. At low temperatures, however, the experimental data contradicted the ordinary views regarding the diffusion of hydrogen in metals. We are not yet sure why this is so. In order to discover the physicochemical nature of the capture and retention of hydrogen ions in metals, we studied the time dependence of the desorption velocity of absorbed hydrogen. The results of this investigation will be published in a later paper.

The results so far obtained lead to the following conclusions.

1. The greatest penetration coefficient and the greatest gas capacity (relative to hydrogen) are found in metals forming strong chemical bonds with hydrogen. These metals are suitable for capturing fast particles in magnetic traps.

2. The number of reflected ions is no greater than a few percent for any of the metals studied, as indicated by the value of η at low concentrations of absorbed hydrogen.

LITERATURE CITED

1. V. A. Simonov, Nuclear Fusion [in Russian], Pt. 1, Vienna, MAGATÉ, p. 325 (1962).
2. E. S. Borovik, N. P. Katrich, and G. T. Nikolaev, Atomnaya Énergiya, 18, 91 (1965).
3. E. Segre, Experimental Nuclear Physics, Vol. 1, Wiley, N. Y. (1953).
4. S. Dushman and J. M. Lafferty, Scientific Foundations of Vacuum Technique, 2nd ed., Wiley, N. Y. (1962).
5. R. Barrer, Diffusion in Solids [Russian translation], Moscow, IL, (1948).

METHOD OF CALCULATING THE INTENSITY OF BACK-SCATTERED γ -RADIATION

B. P. Bulatov

UDC 539.122:539.121.72:621.039.58

Formulas and graphs enabling the energy flux density of back-scattered γ -radiation from certain widely-used isotopes (Co^{60} , Cs^{137} , Au^{198} , Cr^{51}) to be calculated are presented for several typical cases, for example, narrow and wide beams of γ -quanta falling at different angles on to a scattering surface, and an isotropic source in contact with the surface of a reflector. The accuracy of calculations based on these formulas is $\pm 20\%$. The method here presented constitutes the first attempt to produce engineering formulas and nomograms for determining quantities of scattered γ -radiation.

The formulas and graphs presented in this paper give the energy flux density of back-scattered γ -radiation at various distances from the source for several cases frequently found in industrial and laboratory practice: a narrow beam striking the surface of scattering material at various angles, an isotropic source in contact with a surface, and a plane unidirectional flow of γ -quanta. Presently-known theoretical and experimental data give insufficiently general relationships for solving problems of a quantitative nature in connection with scattered γ -radiation, although a combination of existing data [1-11] may be used for calculating the majority of practically interesting cases.

The geometrical aspects of the scattering process are illustrated in Fig. 1a and b.

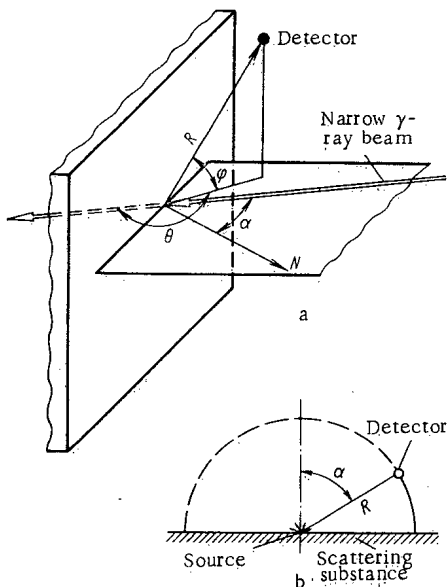


Fig. 1. To illustrate the notation used in the text (θ azimuthal scattering angle; α incident angle; φ latitudinal angle).

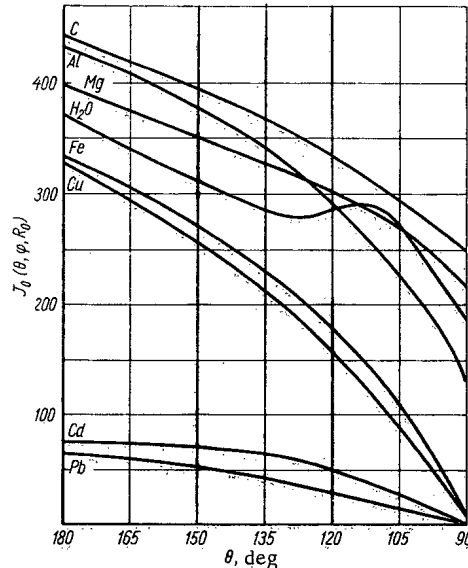


Fig. 2. Distribution function $J_0(\theta, \varphi, R_0)$ for the γ -radiation of Au^{198} (normal incidence of a narrow beam).

Translated from *Atomnaya Energiya*, Vol. 21, No. 5, pp. 345-356, November, 1966. Original article submitted April 1, 1966.

Narrow Beam of γ -Quanta [6, 10]. The energy flux density of radiation scattered in a direction given by the angles θ and φ at a distance R may be determined from the formula

$$J(\theta, \varphi, R) = J_0(\theta, \varphi, R_0) \frac{QE}{R^2} \Omega K, \text{ MeV/cm}^2 \cdot \text{sec}, \quad (1)$$

where $J_0(\theta, \varphi, R_0)$ is the distribution function, Q is the strength of the source in quanta/sec, E is the energy of the primary quanta in MeV, Ω is the solid angle into which the primary radiation is emitted, and R is the distance between the detector and the intersection of the narrow beam with the scattering surface.

According to [6], the empirical constant K equals $8.9 \cdot 10^{-7}$ for the γ -radiation of Co^{60} ($E \sim 1.25$ MeV) at normal incidence on the scattering substance and $9.0 \cdot 10^{-6}$ for oblique incidence; for the γ -radiation of Au^{198} ($E = 0.41$ MeV) these values are $3.5 \cdot 10^{-6}$ and $9.8 \cdot 10^{-6}$ respectively. The corresponding values of the distribution function $J_0(\theta, \varphi, R_0)$ are shown in Figs. 2, 3, 4, and 6.

Formula (1) is applicable for $R > 3L$, where L is the maximum linear dimension of the spot at the intersection of the narrow beam of primary radiation with the scattering surface.

Isotropic Source in Contact with a Surface [7, 8]. The computing formula in this case takes the form

$$J(\alpha, R) = J_0(\alpha, R_0) \frac{0,5QE}{R^2} K \text{ MeV/cm}^2 \cdot \text{sec}. \quad (2)$$

The K factor in formula (2) has the following values: for the γ -quanta of radioactive Cr^{51} ($E = 0.33$ MeV), $K = 1.39 \cdot 10^{-4}$, for Cs^{137} ($E = 0.66$ MeV), $K = 7.14 \cdot 10^{-5}$, and for Co^{60} $K = 7.7 \cdot 10^{-5}$ [7]. The values of the distribution function $J_0(\alpha, R_0)$ are shown in Figs. 5, 7, and 8.

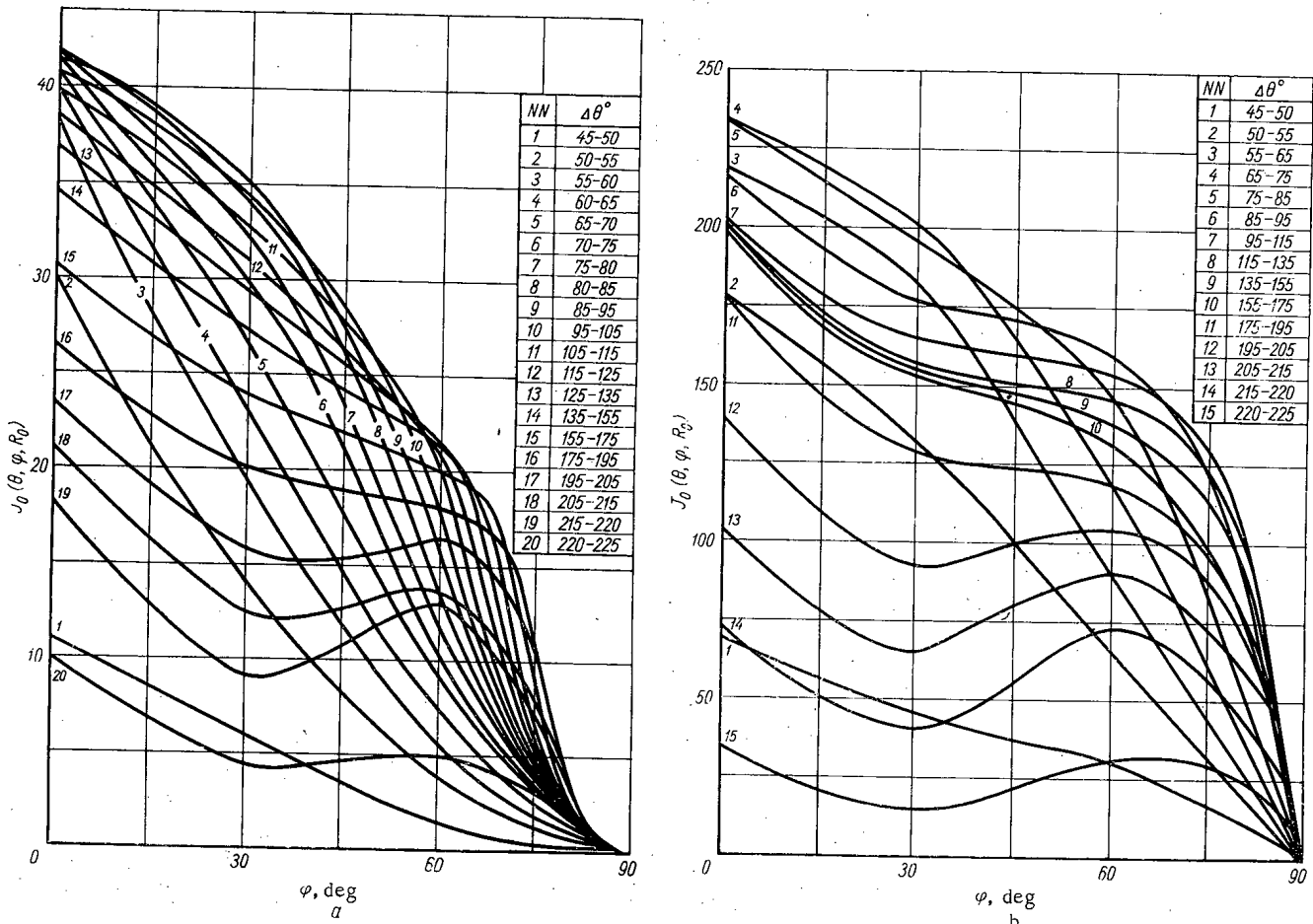


Fig. 3. Distribution function $J_0(\theta, \varphi, R_0)$ of the γ radiation of Au^{198} for the oblique incidence of a narrow beam on various scattering materials : a) lead, $\alpha = 45^\circ$; b) iron $\alpha = 45^\circ$; c) aluminum, $\alpha = 45^\circ$; d) lead, $\alpha = 60^\circ$; e) iron $\alpha = 60^\circ$; f) aluminum, $\alpha = 60^\circ$.

Fig. 3 continued on p. 1026

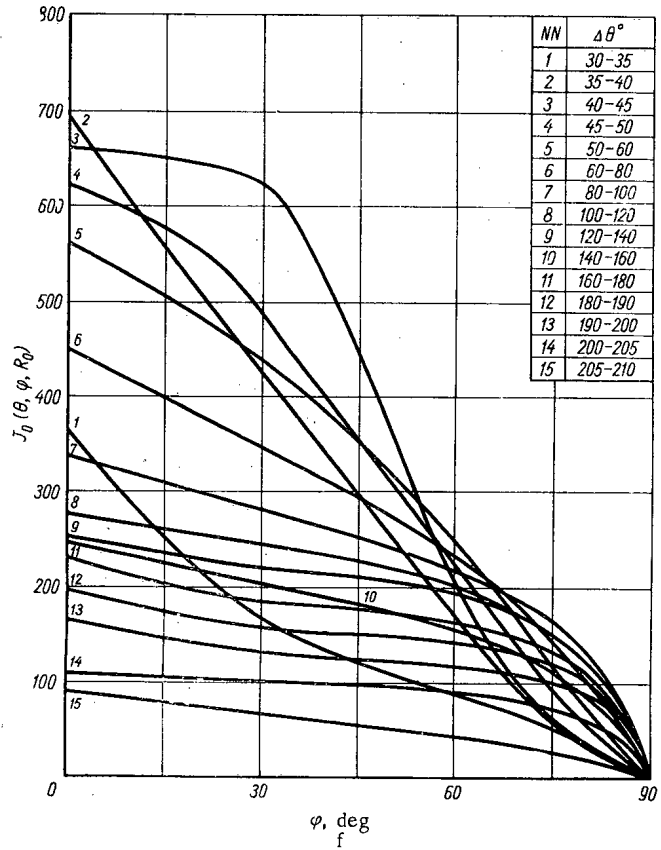
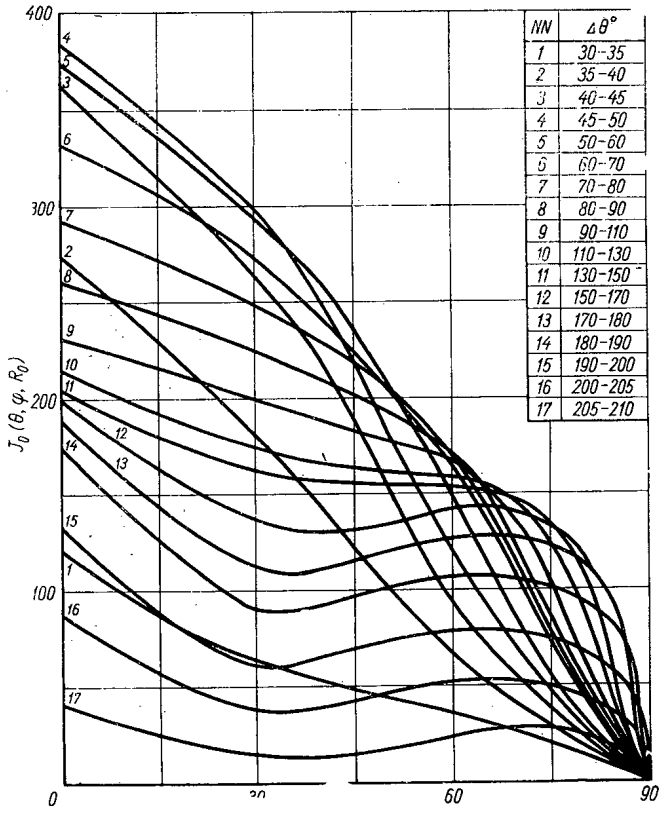
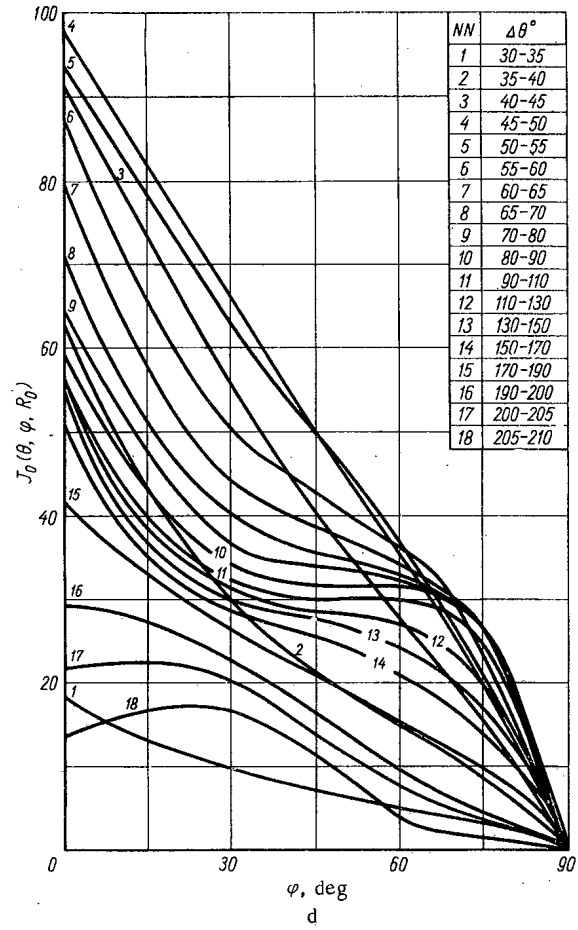
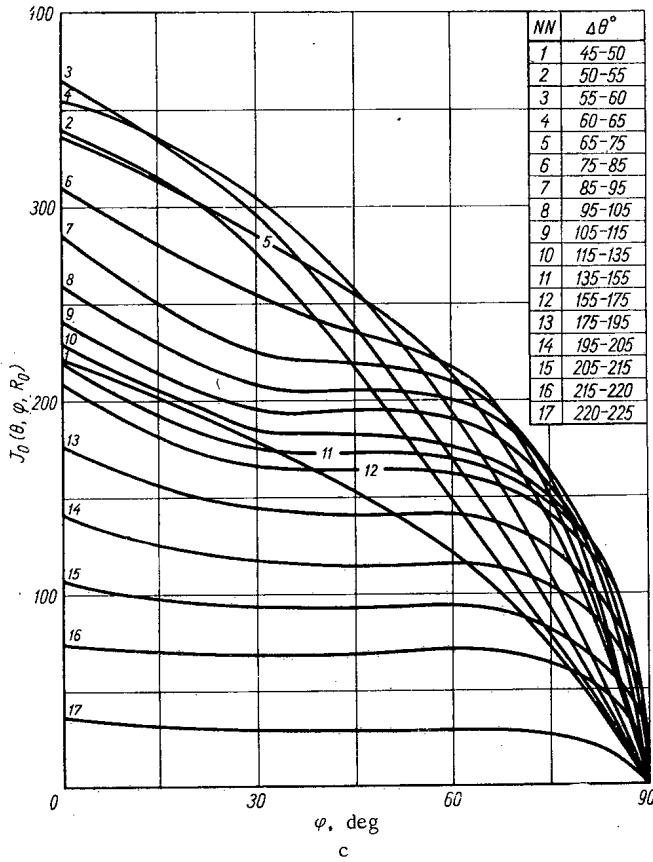


Fig. 3. (continued).

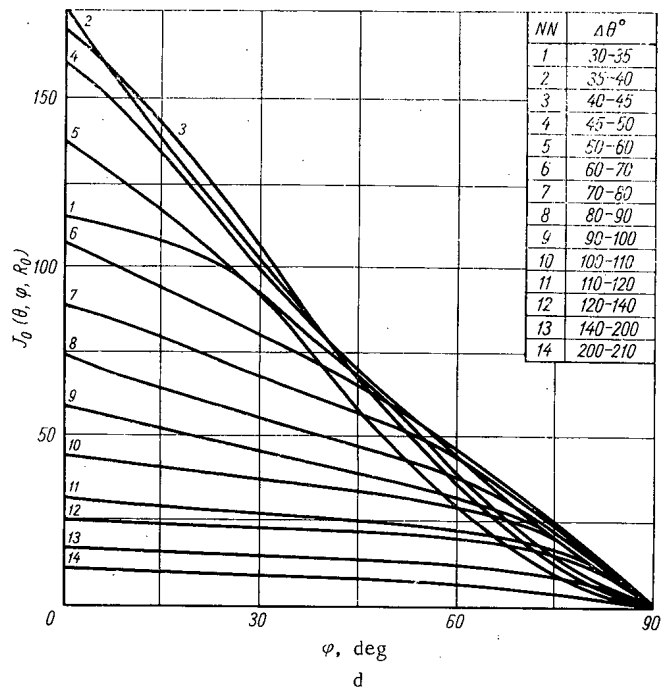
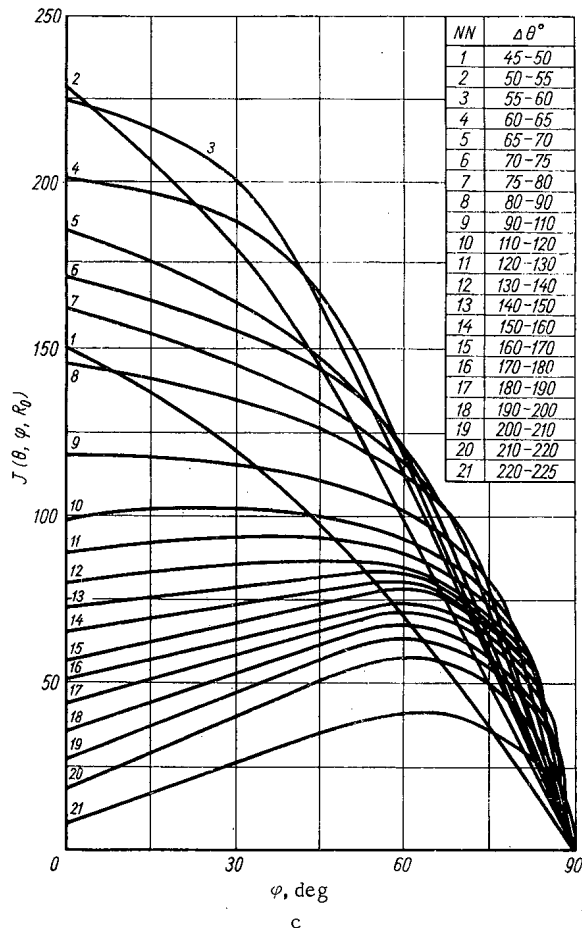
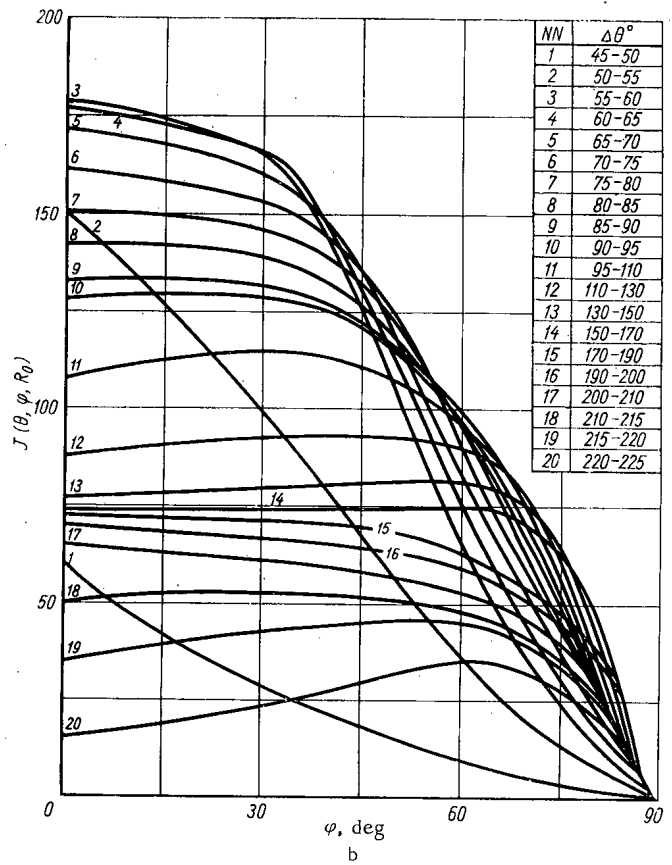
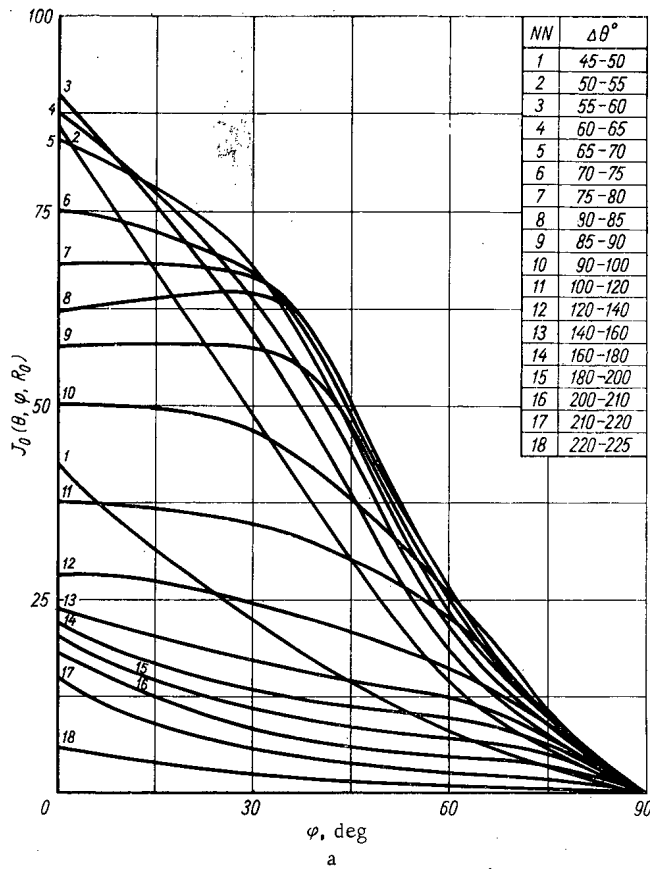


Fig. 4. Distribution function $J_0(\theta, \varphi, R_0)$ of the γ -radiation of Co^{60} for the oblique incidence of a narrow beam on various scattering materials: a) lead; $\alpha=45^\circ$, d) iron; $\alpha=45^\circ$, c) aluminum; $\alpha=45^\circ$, d) lead; $\alpha=60^\circ$, e) iron; $\alpha=60^\circ$, f) aluminum; $\alpha=60^\circ$.

Fig. 4 continued on p. 1028

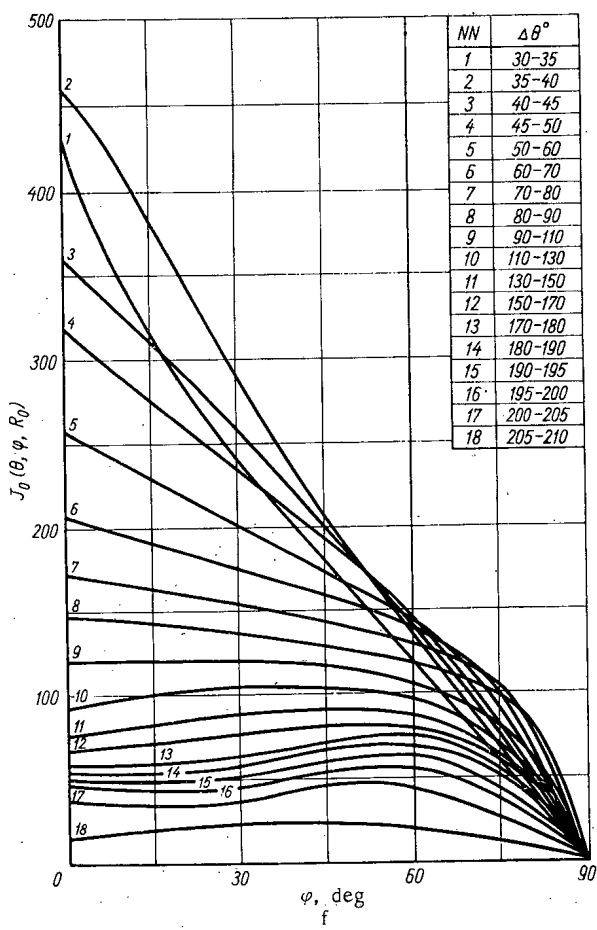
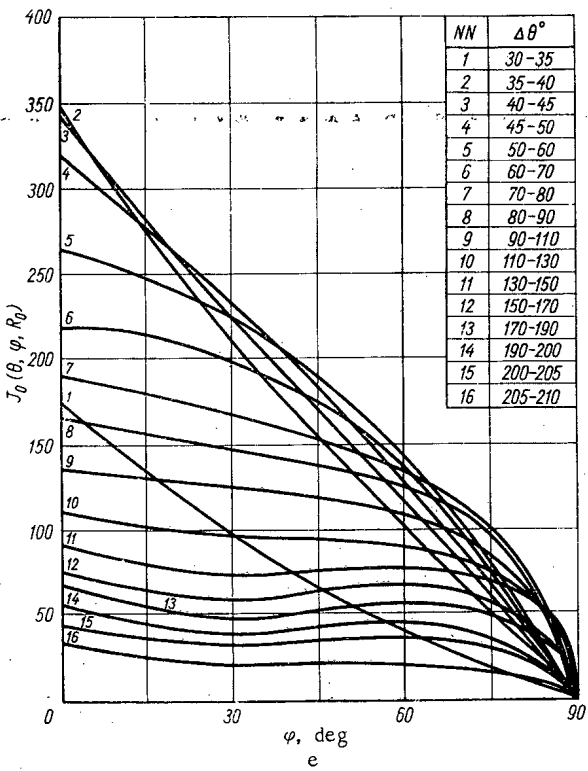


Fig. 4 (continued).

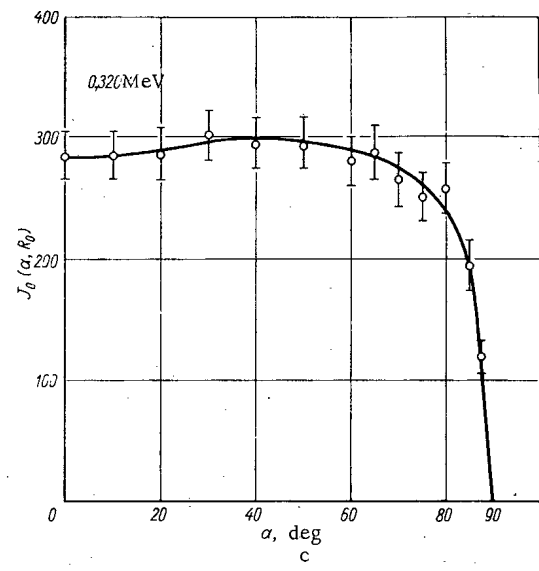
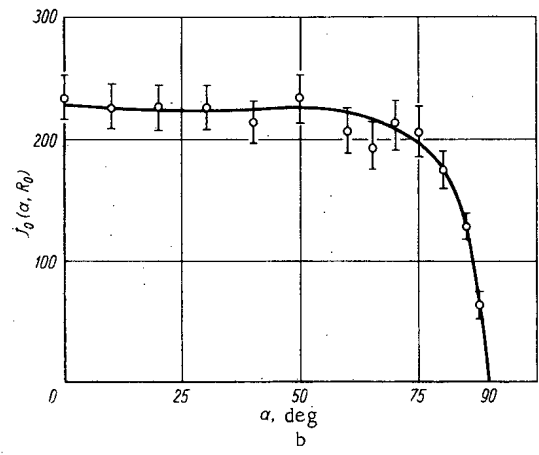
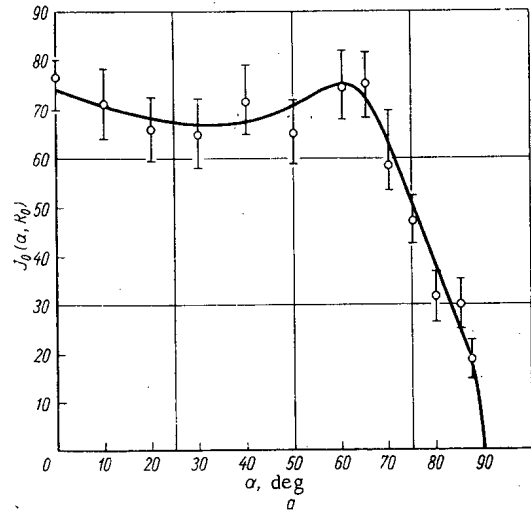


Fig. 5. Distribution function $J_0(\alpha, R_0)$, of the γ -radiation of an isotropic Cr^{51} source for various scattering materials: a) lead; b) iron; c) aluminum.

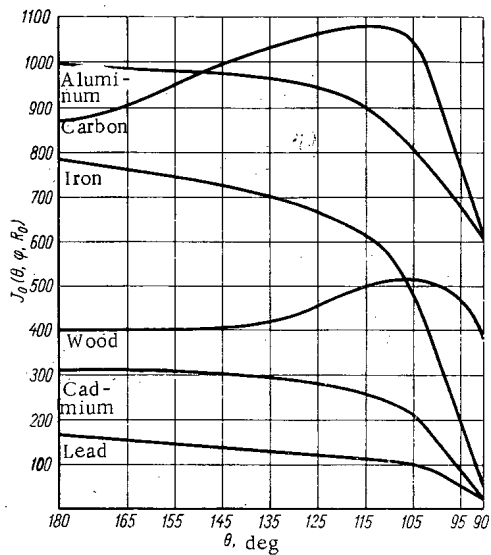
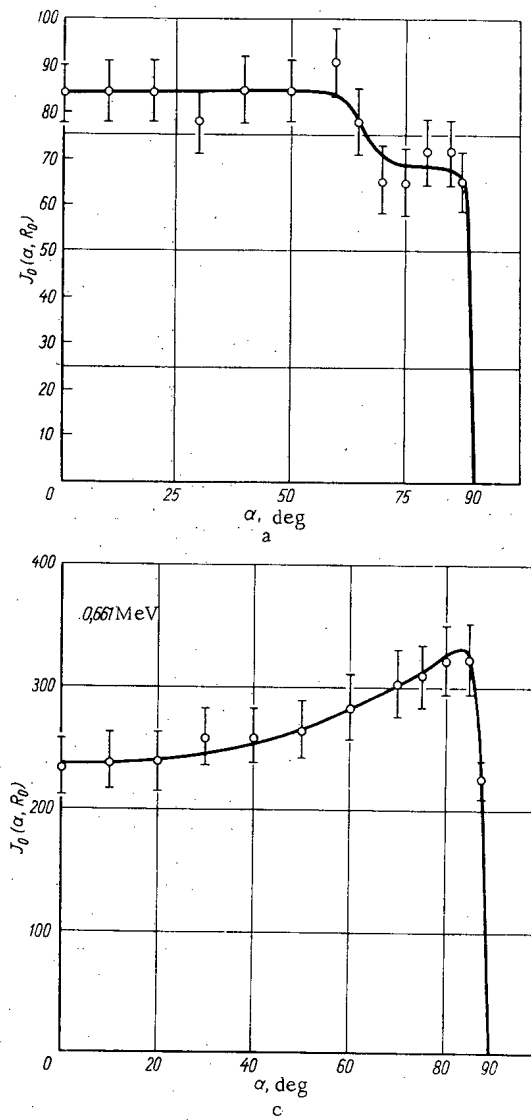


Fig. 6. Distribution function $J_0(\theta, \varphi, R_0)$ of the γ -radiation of Co^{60} for the normal incidence of a narrow beam ($\alpha = 0^\circ$).



Formula (2) is applicable for calculations with $R > 1.5$ to 2.0λ , where λ is the free path of the corresponding quanta of primary radiation in the scattering material, and angles $\alpha < 80$ to 85° .

Plane Unidirectional Flux of γ -Radiation* [1, 2-5, 11].

Here we consider three particular cases.

1. The scattering substance is "infinitely" thick ($d > 1.0$ to 2.0λ), but of limited surface ($\rho < 10h$) [5, 11]. The formula for calculating the intensity of back-scattered γ -radiation as a function of the radius of the circular scattering surface ρ has the form

$$J(\rho, h, \alpha) = \frac{4.4 \cdot 10^{-4} Q}{hr^2 \cos \alpha} \int_0^\rho e^{-\frac{K}{Vh} \rho} \rho d\rho \text{ MeV/cm}^2 \cdot \text{sec} \quad (3)$$

* The concept of a unidirectional flux of quanta may also be used in the case in which the γ -radiation comes from a point source at least $r > 30 h$ away from the detection point [5].

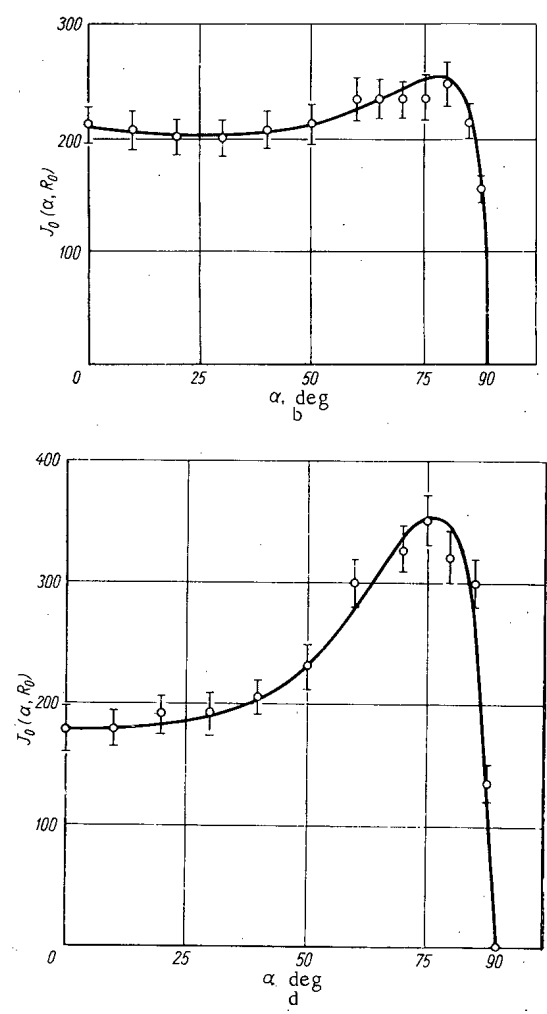


Fig. 7. Distribution function $J_0(\alpha, R_0)$ of the γ -radiation of an isotropic Cs^{137} source for various scattering materials: a) lead; b) iron; c) aluminum; d) carbon.

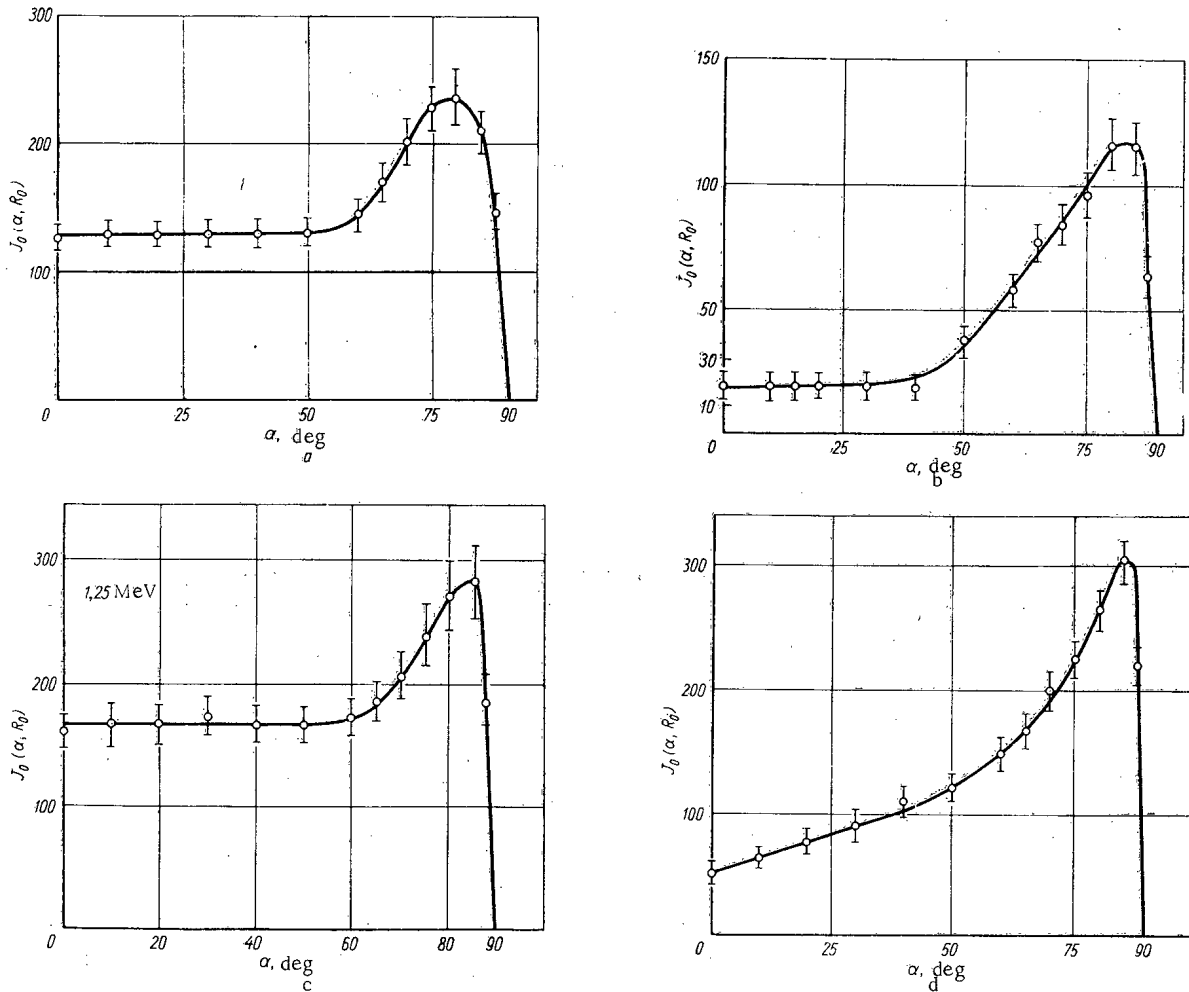


Fig. 8. Distribution function $J_0(\alpha, R_0)$ of the γ -radiation of an isotropic Co^{60} source for various scattering materials: a) iron; b) lead; c) aluminum; d) carbon.

TABLE 1. Values of B_r for Several Energies

Scattering substance	0.41 MeV	0.66 MeV	1.25 MeV
Carbon	1.24-1.26	1.18	1.081-1.088
Concrete	--	1.16	1.063-1.065
Aluminum	1.23-1.25	1.15-1.16	1.085
Iron	1.20	1.12	1.061-1.075
Lead		1.023	1.0095-1.012

where h is the height of the detector above the scattering surface, r is the distance between the latter and the source, and d is the thickness of the scattering substance in g/cm^2 .

The empirical constant K is given [5, 11] by the expression

$$K = 0.2 + 0.02/E \tag{4}$$

for incident primary quanta of energies E between 0.1 and 2.0 MeV.

Formula (3) is applicable to light scattering materials with $Z < 20$, quantum-flux incident angles $\alpha < 80$ to 85° , and $r > 30 h$.

2. The scattering substance is "infinitely" wide but limited in thickness [3-6].

$$J(r, d) = \frac{QE}{4\pi r^2} [B_r - 1] (1 - e^{-d/a}) \text{ MeV}/\text{cm}^2 \cdot \text{sec}, \tag{5}$$

where B_r is the build-up factor for reflection from a scattering substance of infinite thickness and a is a constant equal to half the free path of the primary quanta in a scattering substance with $Z < 26$. For substances with $Z < 26$ this constant is two or three times smaller.

The values of B_r for several energies of the primary quanta are given in the table. Formula (5) is applicable for $r > 30$ h and $\alpha = 0^\circ$.

3. The scattering substance has a nonplanar surface [9]. If the effective radius of curvature of the scattering surface exceeds 1.5 to 2.0 times the free path of the primary quanta in the scattering material, the energy flux density of the back-scattered radiation may be calculated from the formulas for a plane reflector. In the particular case of calculating the intensity of scattered radiation inside closed spherical or cubic cavities containing a central source between 0.2 and 20 m in size (scattered radiation uniformly distributed over the volume of the cavity, at least to an accuracy of 20%), we may use the formula

$$J = \frac{QE}{4\pi r^2} |B_{rc} - 1| \text{ MeV/cm}^2 \cdot \text{sec} \quad (6)$$

The formulas and graphs here considered enable us to calculate the energy flux density of back-scattered γ -radiation to an accuracy of $\pm 20\%$. Practical calculations should allow for the possibility of multiple scattering from surrounding objects and also for scattering in air at distances greater than 20 to 30 m.

LITERATURE CITED

1. M. Leimdörfer, Nucl. Sci. Engng., 17, 345, 352, 357 (1963).
2. F. Corned and R. Liston, Proc. Roy. Soc., 203, 323 (1950).
3. M. Berger and F. Doggett, J. Res. Nat. Bur. Standards., 56, 89 (1956).
4. M. Berger and D. Doggett, Radiation Res., 12, 20 (1960).
5. B. P. Bulatov and O. I. Leipunskii, Atomnaya Energiya, 7, 551 (1959).
6. B. P. Bulatov and E. A. Garusov, Atomnaya Energiya, 5, 631 (1958).
7. B. P. Bulatov, Atomnaya Energiya, 6, 332 (1959).
8. T. Hyodo, Nucl. Sci. Engng, 12, 178 (1962).
9. N. F. Andryushin and B. P. Bulatov, Atomnaya Energiya, 19, 362 (1965).
10. T. Percins, J. Appl. Phys., 26, 1372 (1965).
11. H. Johus and J. Langlin, Radiation Dosimetry, Academic Press, p. 451 (1956).

LIMITING CURRENT DENSITY IN A LINEAR ION ACCELERATOR

A. V. Zotov and V. A. Teplyakov

UDC 621.384.62

The differential equation of the separatrix is found for the initial section of a linear ion accelerator in which the diameter of the group of particles is much greater than its length; the solution of the equation is obtained for three forms of stationary charge-density distribution function in phase space. The solution enables the limiting or saturation current density in the accelerator to be determined.

A knowledge of the limitations imposed on the current passed by an accelerator either in the longitudinal or transverse direction is not only valuable in selecting the acceleration conditions correctly but also in deciding the type of focusing to be used. In this paper we shall estimate the limiting current density associated with the stability of longitudinal motion. The limiting current density determined by the capabilities of the focusing channel was analyzed in [1, 2].

The particles of the accelerated group are acted upon by the phasing force of the hf field, equal to $\frac{evU \sin \varphi_c}{N\beta_c \lambda} \times \frac{2\pi \Delta z}{\beta_c \lambda}$, where $\frac{vU}{N\beta_c \lambda} = E_m$ is the amplitude of the accelerating field, evU is the maximum energy increment of the particle in the gap, $N\beta_c \lambda$ is the length of the accelerating period, φ_c is the synchronous phase, and Δz is the distance between any given particle and the synchronous particle.

The Coulomb force of longitudinal repulsion between the particles in the group is given by the expression $\nabla \cdot \mathbf{E} = \frac{\rho}{\epsilon} \approx \frac{j}{\beta} \sqrt{\frac{\mu}{\epsilon}}$ and equals $\frac{ej k_z}{\beta_c} \sqrt{\frac{\mu}{\epsilon}} \Delta z$, where j is the current density of particles at a given point, $\sqrt{\frac{\mu}{\epsilon}} = 120\Omega$, \mathbf{E} is the Coulomb field of the group, and k_z is the form factor of the group. For the form factor of a uniformly charged ellipsoid of revolution we may write the simple formula

$$k_z \approx 1 - e^{-0.4 \frac{R}{\Delta z_m}},$$

which gives almost exact values over the whole range of ellipsoid-semiaxis ratios $R/\Delta z_m$. (The constant 0.4 is derived from the condition $k_z = 1/3$ at $R/\Delta z_m = 1$). For a stationary charge distribution, the current density in the group does not exceed

$$j_{cr} = \frac{2\pi v U \sin \varphi_c}{N\beta_c \lambda^2 k_z \sqrt{\frac{\mu}{\epsilon}}} = \frac{2\pi E_m \sin \varphi_c}{\lambda k_z \sqrt{\frac{\mu}{\epsilon}}} \quad (1)$$

At $j = j_{cr}$ the phasing and repulsive forces are equal. This estimate, however, is too coarse. A more rigorous estimate of the limiting current is obtained by analyzing the equations of motion on the assumption that the group is in the form of a uniformly-charged ellipsoid of revolution [3, 4]. It is shown in [5] that this approximation is exact: it is possible to have stationary distribution functions (in phase space) such that uniform charge density is maintained over the whole of an ellipsoidal group. Strictly speaking, however, this proof is only valid to a linear approximation. The limitation on the current (with respect to longitudinal motion) is mainly due to nonlinear effects. A more rigorous "self-consistent" solution is given in [6]. The assumption made by the authors of [6] that the group is in the form of a cylinder, nevertheless deprives this of its generality. It may be shown that the solution obtained in [4] on the assumption of a group in the form of a uniformly charged ellipsoid is also as strict in the nonlinear approximation as is the solution of [6]. The difference is that these solutions are obtained for different distribution functions. It should be noted that only methods of solution - not numerical calculations - are considered in [3, 4, 6].

Translated from *Atomnaya Energiya*, Vol. 21, No. 5, pp. 356-360, November, 1966. Original article submitted May 23, 1966.

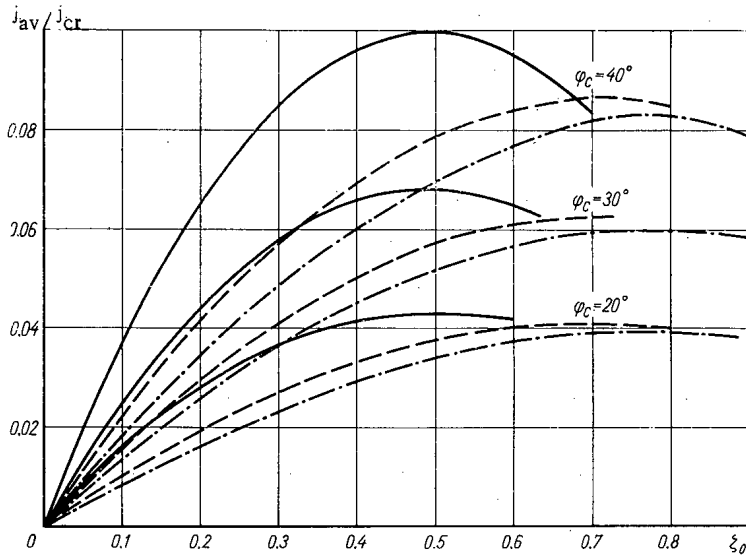


Fig. 1. Limiting current density as a function of the space-charge parameter for three types of distribution functions: — A; - - - B; - · - · - C.

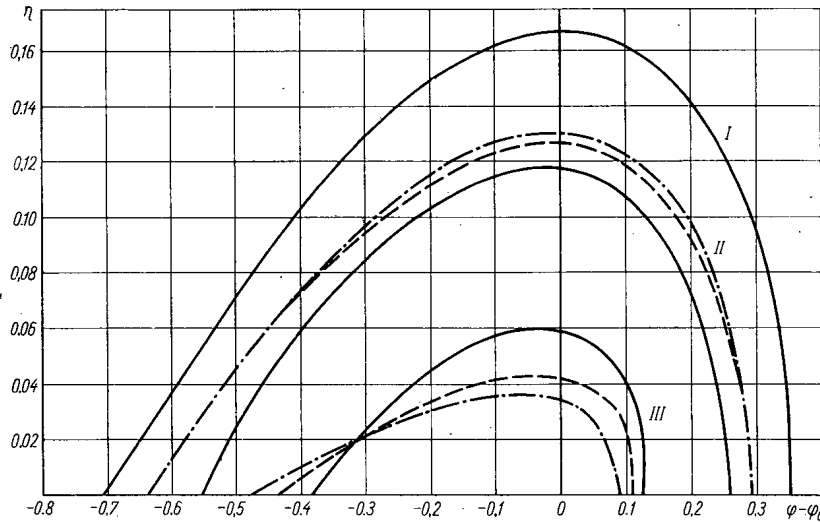


Fig. 2. Separatrices for various values of space-charge parameter ξ_0 and three forms of distributions — A; - - - B; - · - · - C.

We were interested in an accelerator in which the voltage applied to the gaps was kept constant (not the average field). In addition to this, we made the following assumptions: 1) the diameter of the group was much greater than its length; 2) the velocity of the ions was small ($\beta_c \ll 1$), it also varied little over the gap, in which it was independent of radius, and over the period of phase oscillation; 3) all the particles were accommodated in the group; 4) the screening effect of the drift was not taken into account. Except for the first, these are the conventional assumptions. The first assumption enables us to make a one-dimensional approximation (with respect to z): All the particles lie in the plane of the layer, and the accelerator axis (z) is perpendicular to this.

The Hamiltonian

$$\mathcal{H}(\psi, w, n) = \frac{\pi N}{\beta_c^2} + \frac{vL}{\xi} \left[\psi \cos \varphi_0 - \sin(\varphi_c + \psi) \right] - \frac{N\beta_c \lambda}{\xi} \int_0^\psi E(\psi, n) d\psi \quad (2)$$

describes almost conservative motion. Here $n = t/T$ is the number of the gap, $\xi = mc^2/e = 940$ mV for a proton, $\psi = \frac{2\pi}{\beta_c \lambda} \Delta z$ is the phase distance of the particle from the synchronous particle, $\psi = \varphi - \varphi_c$; β_c is the velocity of the synchronous particle, and φ_0 is the phase of the synchronous particle without taking account of space charge.

If the particle distribution is described by the function $f = f(\mathcal{H}_{gr} - \mathcal{H})$, satisfying the kinetic equation $df/dn = 0$, then it is stationary, since the Hamiltonian may be considered as an integral of the motion

$$(\mathcal{H}_{gr} = \text{const}).$$

The charge density and current density in the group respectively equal:

$$\rho(\psi) = \int_{-\infty}^{\infty} f(\mathcal{H}_{gr} - \mathcal{H}) dw; \quad j(\psi) = \int_{-\infty}^{\infty} c\beta f(\mathcal{H}_{gr} - \mathcal{H}) dw \approx c\beta_c \rho(\psi).$$

The boundaries of the group are determined by the projection of the boundary phase curve

$$\mathcal{H}(\psi, w) = \mathcal{H}_{gr} \quad (3)$$

on the ψ axis. The states of all the particles in the group lie inside curve (3).

In order to find the differential equation of the limiting phase trajectory, let us take the second derivative with respect to ψ for both sides of expression (3), taking $\frac{\partial \beta_c}{\partial n} \approx 0$.

As a result of this we obtain

$$y''(\psi) + \frac{\sin(\varphi_c + \psi)}{\sin \varphi_c} - \frac{j(y)}{j_{cr}} = 0. \quad (4)$$

Here $y = \frac{\pi N \zeta}{\sqrt{U} \beta_c^2} \cdot \frac{w^2}{\sin \varphi_c}$; the current density is considered a function of y , since we are only considering points on curve (3), which defines a relationship between y and ψ ; j_{cr} is given by expression (1), where $k_z = 1$.

The particle with $\psi = 0$ will be synchronous and the bounding phase trajectory will be the separatrix if

$$\left. \begin{aligned} y'(0) = 0, & \quad y''(0) < 0; \\ y(\psi_c) = y'(\psi_c) = 0, & \quad y''(\psi_c) > 0. \end{aligned} \right\} \quad (5)$$

The point ψ_c in the phase plane ψ, w is an isolated singularity of the "saddle" type.

Let us find the solution of (4) satisfying condition (5) for three types of distribution function

$$\begin{aligned} \text{A. } f(\psi, w) &= \frac{a}{\sqrt{\mathcal{H}_{gr} - \mathcal{H}}}; \\ \text{B. } f(\psi, w) &= b \text{ St. } (\mathcal{H}_{gr} - \mathcal{H}) = \begin{cases} b & \text{for } \mathcal{H}_{gr} > \mathcal{H}; \\ 0 & \text{for } \mathcal{H}_{gr} < \mathcal{H}; \end{cases} \\ \text{C. } f(\psi, w) &= c \sqrt{\mathcal{H}_{gr} - \mathcal{H}}, \end{aligned}$$

where a, b , and c are normalizing constants.

Case A.

$$e = \frac{2a\beta_c}{\sqrt{\pi N}} \int_0^{w_{gr}} \frac{dw}{\sqrt{w^2 - u^2}} = a\beta_0 \sqrt{\frac{\pi}{N}}$$

i.e., the charge density in the group is constant. Let us write the equation of the bounding trajectory

$$y''(\psi) + \frac{\sin(\varphi_c + \psi)}{\sin \varphi_c} - \zeta_0 = 0, \quad \zeta_0 = \frac{j(0)}{j_{cr}}$$

where $j(0)$ is the current density in the center of the group.

The solution satisfying boundary conditions (5) has the form

$$y(\psi) = \frac{\sin(\varphi_c + \psi)}{\sin \varphi_c} + \zeta_0 \frac{\psi^2}{2} - \psi \operatorname{ctg} \varphi_c + C,$$

where

$$C = \psi_c \operatorname{ctg} \varphi_c - \frac{\sin(\varphi_c + \psi_c)}{\sin \varphi_c} - \zeta_0 \frac{\psi_c^2}{2}.$$

We find the value of ψ_c from the equation

$$-\zeta_0 \sin \varphi_c \psi_c = \cos(\varphi_c + \psi_c) - \cos \varphi_c.$$

Averaging over the accelerating period, the current density is

$$j_{av} = \frac{1}{2\pi} \int_{\psi_c}^{\psi_k} j(\psi) d\psi \simeq \frac{3}{2\pi} j_{cr} \operatorname{tg} \varphi_c \zeta_0 (1 - \zeta_0). \quad (6)$$

For $j(0) = 0.5 j_{cr}$ the mean current density is maximum:

$$j_{av}^{\max} \simeq \frac{3}{8\pi} j_{cr} \operatorname{tg} \varphi_c = \frac{3}{4} \frac{E_m \sin^2 \varphi_c}{\lambda \cos \varphi_c}. \quad (7)$$

For a uniformly charged ellipsoidal group, A. D. Vlasov obtained a formula [4, Eq. (2.53)] for the mean beam current

$$I \leq \frac{3R^2 E_m \sin \varphi_c \varphi_c}{\gamma \lambda k_z} \cdot \frac{\tau S_M (1 - S_M)}{0.18},$$

which in the case of an "infinitely" flattened group ($k_z \approx 1$) gives the limiting current density in the form

$$j_{av}^{\max} = \frac{E_m \varphi_c \sin \varphi_c}{\lambda}.$$

This expression agrees satisfactorily with formula (7).

Case B. The charge is distributed uniformly inside the separatrix, as in [6, 7]. The charge density

$$\rho = 2b \int_0^{w_{gr}} dw = 2b \sqrt{w^2_{gr}}.$$

The equation of the bounding trajectory is

$$y''(\psi) + \frac{\sin(\varphi_c + \psi)}{\sin \varphi_c} - \zeta_0 \sqrt{\frac{y(\psi)}{y(0)}} = 0.$$

The branch of the solution required for our purposes is given by the series

$$y(\psi) = \sum_{n=0}^{\infty} a_n \frac{\psi^n}{n!},$$

where

$$a_0 = y(0); \quad a_1 = 0; \quad a_2 = \zeta_0 - 1; \quad a_3 = -\operatorname{ctg} \varphi_c; \quad a_4 = 1 - \frac{\zeta_0}{2y(0)} (1 - \zeta_0); \quad a_5 = \left(1 - \frac{\zeta_0}{2y(0)}\right) \operatorname{ctg} \varphi_c; \text{ etc.}$$

In order to find the solution, let us expand $\sin(\varphi_c + \psi)$ in series and rid ourselves of the radical. The constant $y(0)$ is given by the condition $\psi = \psi_c$ — a double root. If in the expansion for $y(\psi)$ we confine ourselves to the term of the third degree, we again obtain expressions (6) and (7) for the current density. A more accurate solution of the equation for Case B was obtained by integrating the equation on a computer, the series of the resultant solution converging very slowly for $\zeta_0 > 0.5$.

Case C.

$$\rho = \frac{2c \sqrt{\pi N}}{\beta_c^2} \int_0^{w_{gr}} \sqrt{w^2_{gr} - w^2} dw = \frac{c \sqrt{\pi N}}{\beta_c^2} w^2_{gr}.$$

The equation of the bounding trajectory,

$$y''(\psi) + \frac{\sin(\varphi_c + \psi)}{\sin \varphi_c} - \zeta_0 \frac{y(\psi)}{y(0)} = 0,$$

becomes linear. The solution is obtained from the expression

$$y(\psi) = C_1 \operatorname{Sh} \left(\sqrt{\frac{\zeta_0}{y(0)}} \psi + \chi \right) + \frac{y(0)}{\zeta_0 + y(0)} \cdot \frac{\sin(\varphi_c + \psi)}{\sin \varphi_c},$$

where C_1 and χ are constants determined by condition (5). In order to find $y(0)$ we have to solve a transcendental equation.

Figure 1 shows the mean current density j_{av}/j_{cr} as a function of the current density in the center of the group $j(0)/j_{cr}$ for all three cases considered and three values of synchronous phase φ_c , equal to 20, 30, and 40°.

Figure 2 shows the separatrices for $\varphi_c = 20^\circ$. In order to follow the variation in the synchronous phase resulting from Coulomb forces, the separatrices are plotted as functions of $\varphi - \varphi_0$, where φ_0 is the synchronous phase at zero current. The equation of the separatrix is found from solution (4) and condition (5). For $\rho(y) = 0$

$$\eta = \sqrt{y \sin \varphi_c} = \sqrt{\frac{\pi N \zeta}{v U} \cdot \frac{\beta^2 - \beta_c^2}{2\beta_c}} = \sqrt{\sin \varphi_0 - \varphi_0 \cos \varphi_0 + \sin \varphi - \varphi \cos \varphi}.$$

Figure 2 presents three series of curves: I) the separatrix for zero current; II) the separatrices for $\zeta_0 = j(0)/j_{cr} = 0.2$; III) the separatrices corresponding to maximum average current density j_{av}^{max}/j_{cr} for the three distributions; A) $\zeta_0 = 0.5$, $j_{av}^{max}/j_{cr} = 0.042$; B) $\zeta_0 = 0.7$, $j_{av}^{max}/j_{cr} = 0.041$; C) $\zeta_0 = 0.8$, $j_{av}^{max}/j_{cr} = 0.039$.

Thus the admissible average current density is almost independent of the form of the distribution function used. This indicates that the formula for the average current density in an accelerator with short groups of large diameter is valid for practically all distribution functions.

It should be noted that the maximum average current density is achieved for a certain optimum peak current density, depending on the form of the distribution function.

LITERATURE CITED

1. I. Kapchinsky and V. Vladimirskij, Proc. Internat. Conf. H. Energy Accelerators and Instrumentation, CERN, p. 274 (1959).
2. I. M. Kapchinskii, Atomnaya Énergiya, 13, 235 (1962).
3. A. I. Akhiezer et al., Theory and Calculations of Linear Accelerators [in Russian], Moscow, Atomizdat (1965).
4. A. D. Vlasov, Theory of Linear Accelerators [in Russian], Moscow, Atomizdat (1965).
5. B. I. Bondarev and A. D. Vlasov, Atomnaya Énergiya, 11, 423 (1965).
6. I. M. Kapchinskii and A. S. Kronrod, in the Book: Transactions of the International Conference on Accelerators, Dubna, (1963) [in Russian], Moscow, Atomizdat (1964).
7. C. Nilsen and A. Sessler, Rev. Scient. Instrum., 30, 80 (1960).

USE OF THE CALCULATED-EXPENSE METHOD FOR CHOOSING
THE CHARACTERISTICS OF A FAST REACTOR

V. B. Lytkin, M. F. Troyanov,
and A. I. Novozhilov

UDC 338.4:621.039.516.4

The article describes how a calculated-expense formula can be used for analyzing the economics of the fuel cycle of a fast plutonium reactor. The proposed formula takes account of the down time in the fuel cycle for the fissionable material of the active zone and the blankets. It gives the results of the calculations, which are used for investigating how the fuel component of the calculated expenses depends on the power density and the "flattening" of the active zone of a reactor with an electrical power of 1000 MW.

The calculation of the economic efficiency of an atomic power station involves the problem of correctly matching lump-sum expenses and operating expenses. A property peculiar to the fuel cycle of an atomic power station is the fact that there is a large lump-sum expense for the first charging of the reactor and that in the initial period of operation (until fuel recycling begins), some of the fissionable material is on down time. This quantity of material remains in the fuel cycle at all times and can be salvaged only after the station has ceased operations.

A number of methods are known for taking account of the original fuel expenses. The most widely used one is the method of calculated expenses (or the recoument-period method) [1]. For example, it was used in [2, 3] for selecting the optimum reactor characteristics.

Using this method, we can represent the annual fuel expenses by the formula

$$Z_f = p_n K_f + C_f, \quad (1)$$

where p_n is a normalization coefficient of the efficiency of operating assets; K_f is the amount of initial expense for fuel; C_f is the fuel component of the cost of electrical energy when the reactor is in steady state operation, i.e., when there is recycling of fuel from reprocessing. In a fast reactor C_f includes the expenses for the fuel recharging and the income from the surplus plutonium.

Calculating C_f is a simple matter. The calculation of K_f is more complicated, since from the economic point of view, nuclear fuel has some features both of fixed assets and of circulating assets.

In the case of a fast plutonium reactor, K_f may be represented in the form*

$$K_f = G_a x_i c_9 T_{st}/T_a + G_a \bar{x} c_9 + G_a x_f c_9 T_p/T_a + G_{fb} \bar{z}_{fb} (1 + T_p/T_{fb}^0) + G_{sb} \bar{z}_{sb} c_9 (1 + T_p/T_{sb}^0) + (G_a c_{ma} + G_{fb} c_{mb}) (1 + T_{st}/T_a) + G_{sb} c_{mb} (1 + T_{st}/T_b) + k_m. \quad (2)$$

Here G_a is the inventory of the active zone; G_b and G_{sb} are the depleted-uranium inventories of the front and side blankets; x_i , \bar{x} , and x_f are the initial, average, and final concentrations of plutonium in the fuel; \bar{z}_{fb} and \bar{z}_{sb} are the plutonium concentrations in the front and side blankets, respectively, averaged over the charge-life; T_a and T_{sb} are the effective charge-lives of the reactor and the side blanket (if we consider $\varphi = 0.8$); T_p is the time for the external fuel cycle; T_{fb}^0 and T_{sb}^0 are the average residence times for the plutonium in the front and side blankets, respectively; K_m is the amount of mixed capital investments in the fuel-cycle enterprises, which are taken into account only in calculating the expenses for production costs; T_{st} is the time spent by the fuel and depleted uranium in storage, fabric, and transit; c_9 , c_{ma} , and

* For the sake of simplicity, the value of the depleted uranium was taken to be zero.

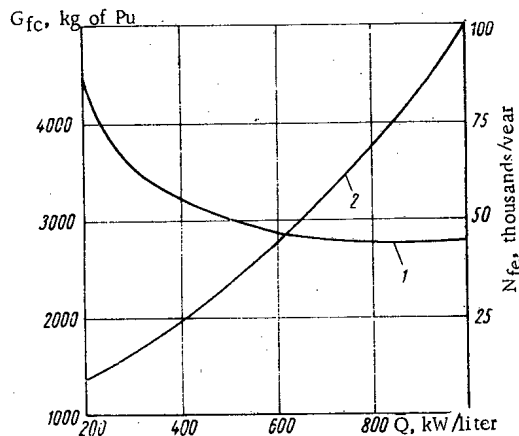


Fig. 1. Amount of plutonium in the fuel cycle of the active zone, G_{fc} , and number of fuel elements required annually, N_{fe} , as functions of the power density of the active zone: 1) amount of plutonium in the cycle; 2) number of fuel elements required annually.

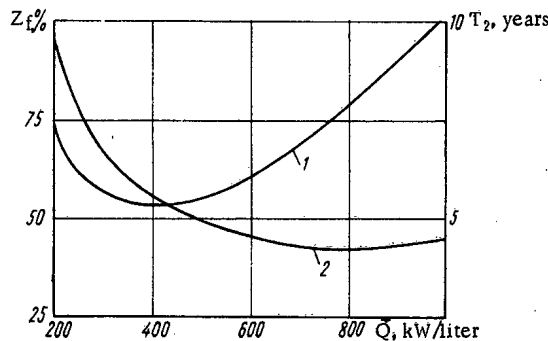


Fig. 2. Fuel component of calculated expenses and doubling time, as functions of Q : 1) fuel component; 2) doubling time.

c_{mb} are, respectively, the cost of plutonium, the cost of manufacturing the fuel elements of the active zone, and the cost of fabricating the fuel elements of the blankets.

Formula (2) takes account of the change in value of the fuel during the time it remains in the reactor and the time delays in the recovery of the fuel during reprocessing and also the time delay when the plutonium is removed from the blankets. Although there are no initial expenses for the plutonium in the blankets, the production of plutonium in the blankets involves the "freezing" of a certain amount of this fissionable material. Just as in the active zone there is a time difference of $(T_a + T_p)$ between spending money to buy fuel and obtaining a return of its value, the blanket cycle includes delays of $(T_{fb}^0 + T_p)$ and $(T_{sb}^0 + T_p)$ in the front and side blankets, respectively, before there is any return of the income on the plutonium. In other words, the blanket-plutonium income counted in the cost at time t will not actually be received until time $(t + T_{fb}^0 + T_p)$ or $(t + T_{sb}^0 + T_p)$. As a result, there is a "down time" of these assets, which is reflected in the fourth and fifth terms of Eq. (2). The necessity of including this "down time" in the formula can be demonstrated if we consider the total fuel expenditure for a fast plutonium reactor during a time equal to the normative recoupment period.

It should be noted that the inclusion of the "frozen" secondary fuel in the engineering and accounting calculations by means of extra charges was first suggested in a general way in [4]. By using formula (2) to calculate K_f in the formula for Z_f , we can analyze the influence exerted on the fuel-cycle expenses by such time factors as T_a , T_{fb}^0 , T_{sb}^0 , and T_p , select the optimum blanket thickness and degree of burn-up, and obtain a graph of the recharging of the side blanket.

The main contribution of the value of K_f is made by the first three terms, which relate to the active zone. For this reason, in approximate calculations, when we do not need any special accuracy for the absolute values of Z_f , and are not investigating any special mode of blanket operation, we can calculate K_f by using only the first three terms of formula (2).

This was done in the present study in order to simplify the variant calculations in the investigation of how Z_t varies with the power density \bar{Q} of the active zone and with the ratio of the diameter of the active zone to its height, for a large fast reactor with the following characteristics:

Reactor thermal power	2500 MW
Electrical power	1000 MW
Fuel	PuC-UC mixture
Time of external cycle	1 year

In the active zone we flattened the radial field of heat generation by means of two zones of equal enrichment. The physical calculations were carried out on electronic computers according to a complex program worked out by the Moscow Institute of Engineering and Physics [5]. The doubling time was calculated by the method proposed by L. N. Usachev [6].

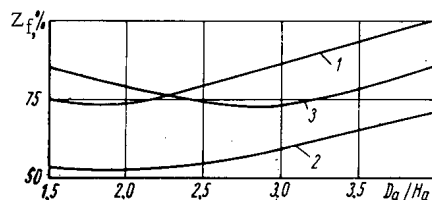


Fig. 3. Fuel component of calculated expenses as a function of D_a/H_a for the following values of power of the active zone (kW/liter): 1) 200; 2) 400; 3) 800.

In the calculations it was assumed that the cost of manufacturing one fuel element is independent of its dimensions within the limits of dimensional variation considered in the study. For this reason, the cost of manufacturing a fuel element (in rubles/kg) as a function of the element diameter may be represented as the sum of two terms:

$$c_{ma} = c_1 + c_{fe}(4/\pi d_{fe}^2 H_a \gamma_f), \quad (3)$$

where c_1 is a constant term independent of the dimensions of the fuel element*; c_{fe} is the cost of manufacturing one fuel element (assumed constant), in rubles/element; d_{fe} is the diameter of the element (a function of \bar{Q}); H_a is the height of the active zone (a function of \bar{Q}); γ_f is the density of fuel.

The cost of manufacturing the fuel elements in the blanket is assumed to be constant.

Figures 1 and 2 show the results obtained by calculating the amount of plutonium in the cycle, the number of fuel elements required annually, the time required for doubling the power, and the fuel component of the calculated expenses for various values of the power density of the active zone. The natural indicators are shown for comparison and to clarify how Z_f varies as a function of \bar{Q} . It can be seen from Fig. 2 that the $Z_f = f(\bar{Q})$ curve has a relatively flat optimum in the region about $\bar{Q} = 400$ kW/liter. The \bar{Q} value which is optimal in the sense of giving a minimum of T_2 is considerably larger (about 800 kW/liter). However, since both curves are relatively flat in the optimum zone, we can select a \bar{Q} value for which the doubling time will be sufficiently short and the fuel component of the calculated expenses will not increase too much. The total calculated expenses, plotted as a function of the power density of the active zone, will vary considerably less than the fuel component, since the latter amounts to only 15-20% of the total calculated expenses. This enables us to select out value of \bar{Q} from an even broader range of values without causing any substantial increase in the total calculated expenses.

Figure 3 shows how the fuel component of the calculated expenses varies as a function of the ratio of the active-zone diameter, D_a , to the active-zone height, H_a , for three values of \bar{Q} . By increasing this ratio, we can improve the physical characteristics of high-power reactors [7]. This makes it possible to increase the reproduction factor and fuel-element diameter for the same active-zone volume.

These examples of the use of the calculated-expense method for investigating the fuel cycle of a power reactor show that the method enables us to evaluate the relative roles played by the initial investments of assets in the fuel cycle and the amounts of continuing expenses for the fuel cycle, so that we can select the optimum reactor characteristics more correctly.

In conclusion, the authors express their gratitude to A. I. Leipunskii and V. V. Orlov for their interest in the work and their valuable comments. We also thank G. S. Filatov for his help in the calculations.

LITERATURE CITED

1. Typical Procedure for Determining the Economic Efficiency of Capital Investments and New Techniques in the National Economy of the USSR [in Russian], Moscow, Gosplanizdat (1960).
2. Yu. D. Arsen'ev, Analysis of the Thermodynamic Cycle of Atomic Power Stations by the Basing-Point Method [in Russian], Moscow, Gosatomizdat (1962).
3. Yu. I. Koryakin, V. V. Batov, and V. G. Smirnov, *Atomnaya Énergiya*, 17, 94 (1964).
4. O. D. Kazachkovskii, Report No.2028, presented by the USSR at the Second International Conference on the Peaceful Use of Atomic Energy (Geneva, 1958).
5. I. S. Slesarev et al., In the collection "Some Questions of Nuclear-Reactor Physics and Technology [in Russian], Moscow, Atomizdat, p. 70 (1966).
6. A. I. Leipunskii et al., Report No.369, presented by the USSR at the Third International Conference on the Peaceful Uses of Atomic Energy (Geneva, 1964).
7. V. V. Khromov et al., *Atomnaya Énergiya*, 17, 199 (1964).

* This includes, for example, the cost of preparing the mixture of PuC and UC powders.

IR-100 RESEARCH AND TRAINING REACTOR

Yu.M. Bulkhin, A.D. Zhirnov, G.N. Zhemchuzhnikov, UDC 621.039.520.21
 L.V. Konstantinov, V.A. Nikolaev, I.A. Stenbok,
 V.S. Lobanov, N. A. Khryastov, and A. G. Filippov

The design, physico-technical characteristics, and experimental capabilities are described for the IR-100 research reactor with a thermal output of 100 kW, which is intended for conducting scientific-research projects and also for training specialists in the field of atomic energy.

The construction of research reactors with a thermal output of 100-200 kW is making it possible to undertake scientific investigations for which thermal neutron fluxes in the core of the order of 10^{12} n/cm²·sec and neutron beams at the channel exit of 10^9 n/cm²·sec are required. Such reactors are indispensable for training highly qualified scientific and engineering personnel, since the relatively small cost of these installations enables them to be installed in universities and in developing countries. This, obviously, also explains the widescale distribution abroad of reactors of the Triga and Argonaut type [1].

A reactor of this type, planned in the USSR, is the IR-100 reactor with a maximum thermal power of 100kW. This is a water-cooled/water-moderated research reactor of the swimming pool type with various experimental facilities. The layout of the reactor, the scientific research laboratories and ancillary equipment in one building facilitates the choice of structural area and reduces the installation costs of the entire complex. The IR-100 reactor is significantly less expensive than reactors of the IR-2000 and VVR type [2]. Planning of the IR-100 reactor was aimed at the simplest construction. The low power of the reactor permits heat removal by natural convection of the coolant. The control and safety system used in the reactor enables accidental power excursions due to operator error to be avoided.

SPECIFICATION AND EXPERIMENTAL FACILITIES OF THE REACTOR

The basic physico-technical parameters for the IR-100 reactor are as follows:

Reactor type	Swimming pool
Nominal power, kW	100
Fuel	UO ₂ 10% enriched
Minimum critical mass with respect to U ²³⁵ isotope, kg	2.6
Moderator	Water
Coolant	Water
Reflector	Graphite
Maximum thermal neutron flux at the center of the core, n/cm ² ·sec	2×10^{12}
Maximum fast neutron flux at the center of the core, n/cm ² ·sec	2.2×10^{12}
K _∞	1.57
τ, core, cm ²	52
Maximum excess reactivity available for experiments, %	2.3
Number of control rods:	
automatic (coarse) control	1
scram rods	3
manual control	2

Translated from Atomnaya Énergiya, Vol. 21, No. 5, pp.363-368, November, 1966. Original article submitted July 28, 1966.

Total compensating efficiency of control rods, %	2.4
Cooling system	Natural circulation
Core configuration	Regular hexagonal prism, length of each face 240mm
Height of core, mm	500

The neutron-technical characteristics of the experimental facilities of the IR-100 reactor are given in the Table 1.

Horizontal channels, pneumatic rabbits, vertical experimental channels, a graphite thermal column with a tank for mounting exponential experiments, a glory hole with an open box, the front part of which fits onto the reflector of the reactor, are provided for carrying out experimental projects.

The design of the experimental facilities of the IR-100 and the thermal and fast neutron fluxes, and the γ -radiation fluxes permit neutron- and γ -spectrometric studies to be undertaken; it is also possible to study the deformation of neutron and γ -radiation spectra as a result of their passage through various materials, to investigate the shielding properties of materials and their composition, and also to carry out in situ tests on reactor shield mock-ups. The horizontal channels and the hole with the "roll-away" box can be used for these investigations.

The moderating and diffusion properties of substances can be studied in the graphite thermal column. An aluminum tank above the thermal column permits exponential experiments to be carried out for cores with both solid and liquid moderators. The installation of a uranium converter makes it possible to study the moderating properties of liquids in this same tank.

Despite the relatively low neutron fluxes (10^{11} n/cm²·sec) in the vertical experimental columns located in the reflector, it is possible to study the effects of radiation on insulating organic semiconductor materials and instruments; the mechanism and methods of controlling chemical processes can be established (radiation polymerization, radiation oxidation, etc) [4].

In case of requirements for producing a large integral flux, the central vertical experimental channel can be used, in which the unperturbed thermal neutron fluxes reach 2×10^{12} n/cm²·sec. In addition, the vertical experimental channels could be used for the production of radioactive isotopes. The experimental channel with the pneumatic rabbit allows experiments to be carried out for studying isotope isomers and also for studying and using short-lived radioactive isotopes.

Isotope activation analysis investigations can be undertaken in the IR-100 reactor. Activation analysis is particularly effective for determining trace impurities with sufficiently large activation

TABLE 1. Experiment Facilities of the IR-100 and Their Neutron-Technical Characteristics

Designation	Number	Diameter, mm	Cross section through face, mm	Neutron flux at nominal reactor power, n/cm ² ·sec		Notes
				thermal	fast	
Horizontal channels	3	100	---	$1.5 \cdot 10^8$	10^8	Neutron fluxes at exit from experimental channels in reactor hall
Vertical channels	1	38	—	$2 \cdot 10^{12}$	$2.2 \cdot 10^{12}$	
	2	85	—	$2 \cdot 10^{11}$	$5 \cdot 10^{10}$	
	2	52	—	$2 \cdot 10^{11}$	$5 \cdot 10^{11}$	
	4	52	—	$7 \cdot 10^{11}$	$3 \cdot 10^{11}$	
Pneumatic rabbit	1	30	—	$2 \cdot 10^{12}$	$2.2 \cdot 10^{12}$	At the core center
Experimental hole	1	—	800×800	$7 \cdot 10^{11}$	$5 \cdot 10^{11}$	At the inner face adjacent to the core
Thermal graphite column	1	—	800×1000	10^5 — 10^8	—	Neutron flux depends on the void fraction in the thermal column
Experimental tank	1	1000	$7.8 \cdot 10^6$	10^7 — 10^9	—	For conducting neutron physics studies

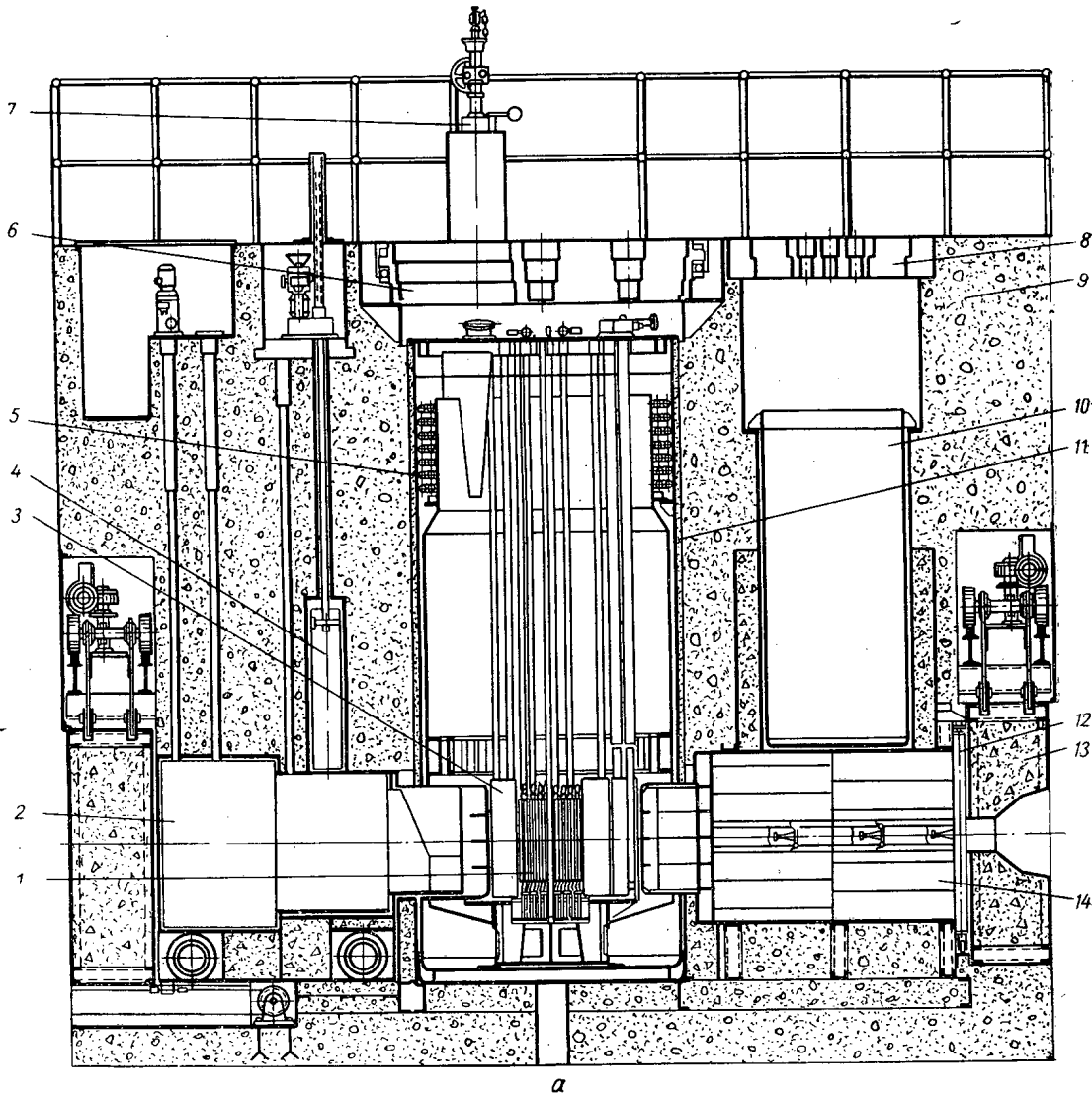


Fig. 1. Longitudinal (a) and transverse (b) sections through the IR-100 reactor: 1) core; 2) roll-away box; 3) reflector; 4) lifting slide-valve; 5) heat exchanger; 6) rotatable plate; 7) charging mechanism; 8) removable plate; 9) biological shield; 10) experimental tank; 11) reactor housing; 12) paraffin block; 13) roll-away door; 14) thermal column; 15) pneumatic rabbit; 16) hot box; 17) slide-valve.

Fig. 1 continued on p. 1043

cross sections in reactor or semiconductor materials. The most modern equipment permits the range of application of activation analysis to be extended [6].

The radioactive isotopes produced by means of the reactor (including also short-lived isotopes) make it possible to undertake investigations in the fields of medicine, biology, agriculture, and technology. In addition, by studying the effect of radiation of different intensity and duration on biological specimens, research into controlled hereditary change in plants and animals can be undertaken.

The installation of an oscillator makes it possible to measure the absorption cross sections for thermal and resonance neutrons in various materials. The IR-100 reactor can be used for testing reactor control equipment under actual conditions, and for checking new methods and instruments developed for other reactors. For example, equipment for analyzing reactor noise can be checked beforehand and adjusted in the IR-100 reactor. In this case, the measurement results can be compared with data obtained by means of an oscillator. The checking of equipment for measuring transfer functions in the IR-100 reactor is particularly advantageous, since the transfer function for this type of reactor is studied most completely at low power.

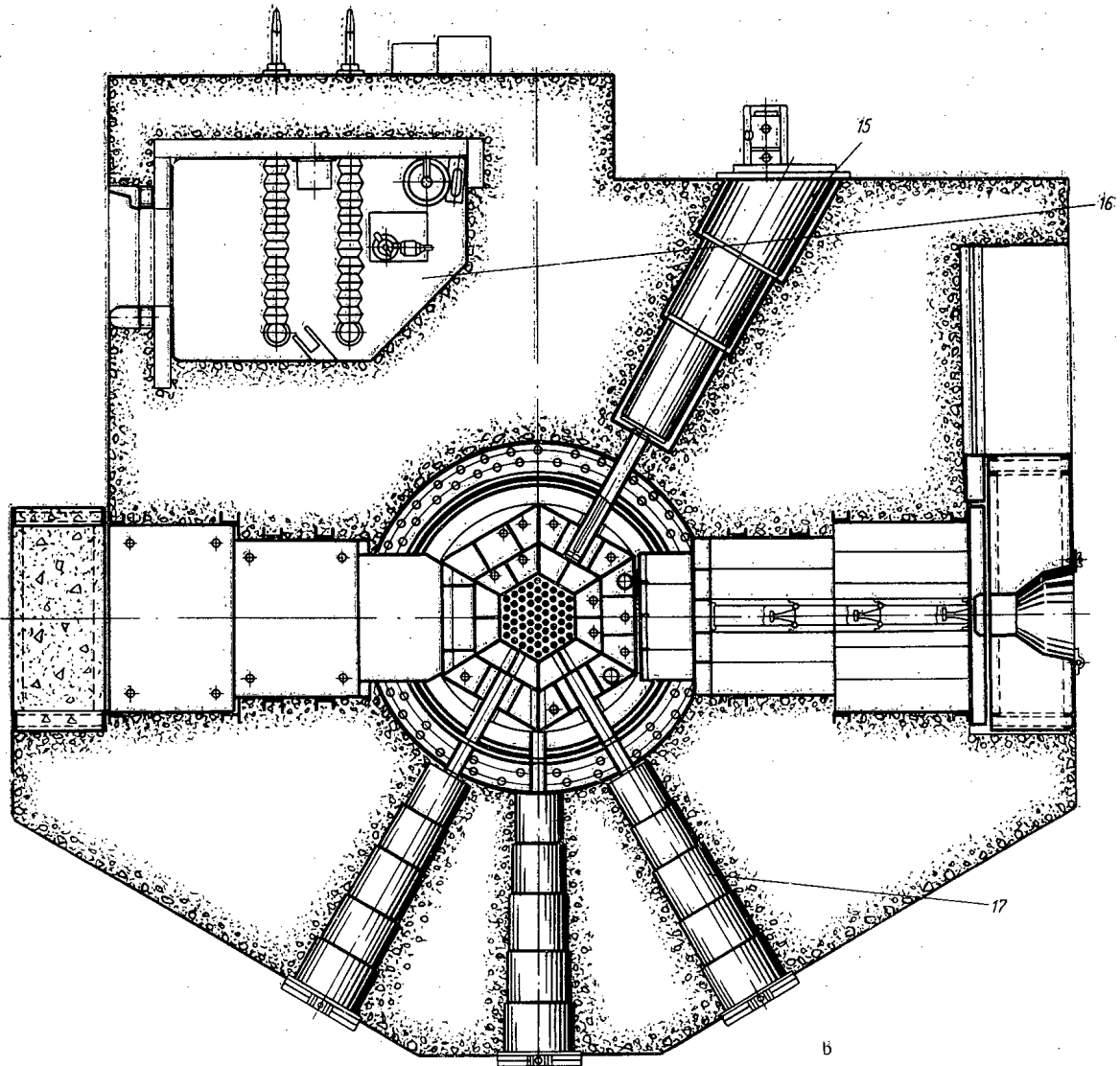


Fig. 1 (continued)

The list of possible scientific-research capabilities of the IR-100 reactor can be lengthened. However, what has already been said is sufficient to indicate convincingly the versatility of the reactor. The participation of students and practical workers in the scientific investigations permits specialists, who are highly-qualified in different fields of science and technology, to be trained.

EXPERIMENTAL FACILITIES

Figures 1a and 1b show the longitudinal and transverse sections through the reactor. The blocks of the graphite reflector (Fig. 2.), which are mounted on a special support in the aluminum reactor tank, have the following experimental facilities which are provided for in the design:

1) three horizontal channels with a diameter of 100 mm, arranged in the plane of the central section of the reactor core. The slide-valves of the experimental channels are led out into the reactor hall for carrying out experiments. Each channel is provided with safety equipment which allows training to be given to research workers when operating the reactor.

2) a pneumatic rabbit channel with a diameter of 30 mm, intended for the rapid transportation samples from the core. This channel emerges into a box equipped with special devices for working with active samples and for carrying out activation analysis on isotopes of elements with short half lives.

3) vertical experimental channels, one of which with a diameter of 38 mm is located at the center of the reactor core, and eight channels (two with a diameter of 85 mm and six with a diameter of 52 mm) are located in the graphite reflector at various distances from the center of the core.

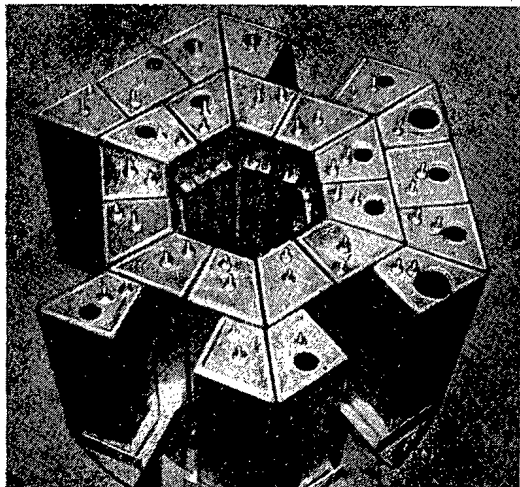


Fig. 2. Graphite reflector of the IR-100 reactor.

4) a thermal column, whose inner face adjoins the graphite neutron reflector, and whose outer face opens into a special room which is isolated from the reactor hall. The outer face is covered by a block of paraffin wax and boron carbide and a roll-away door filled with high-density concrete ($\gamma = 5.2 \text{ t/m}^3$).

5) above the central part of the thermal column is located an aluminum tank with a diameter of 1000 mm for setting up exponential experiments.

6) an experimental hole located on the face opposite the thermal column and adjoining the first set of blocks of the graphite reflector. The experimental hole is intended for studying the shielding properties of materials and their composition. It is equipped with a movable structure for setting up specimens to be studied. The specimens are mounted in special containers which are isolated from the physical reactor hall. The recess is equipped with shielding equipment: a vertical slide-

valve and a roll-away shielding door filled with high-density concrete ($\gamma = 5.2 \text{ t/m}^3$). The slide-valve and the roll-away door shield the assembly chamber of the experimental recess from the reactor radiation.

7) in the concrete block of the reactor biological shield are located a) a hot box, which is connected with the upper reactor space (between the rotatable shielding plate and the water level) by means of a special conveyor mechanism, so that irradiated samples after withdrawal from the vertical channels can be transferred to the hot box; and b) a storage well and dry boxes for storing processed cassettes and radioactive units of the reactor or experimental assemblies (control rods, channel probes, etc).

LITERATURE CITED

1. Directory of Nuclear Reactors. Vol. 2. Vienna, IAEA, p. 3, 5 (1964).
2. V.V. Goncharov et al., In: "Proceedings of the International Conference on the Peaceful Uses of Atomic Energy" (Geneva, 1958), Report of the Soviet Scientists, Vol. 2, Moscow, Atomizdat, p. 273 (1959).
3. T.A. Lopovok, In: "Proceedings of the International Conference on the Peaceful Uses of Atomic Energy" (Geneva, 1958), Report of the Soviet Scientists, Vol. 2, Moscow, Atomizdat, p. 259 (1959).
4. Chemistry Research and Chemical Techniques Based on Research Reactors. Report of a Panel on Chemistry Research Using Research Reactors. Vienna, 4-8, March (1963).
5. Production and Use of Short-Lived Radioisotopes from Reactors. Proceedings of a Seminar. Vol. I, Vienna, 5-9, November (1962).

EVAPORATION RATES OF CATHODES MADE OF URANIUM CARBIDE,
ZIRCONIUM CARBIDE, AND THEIR SOLID SOLUTIONS

B. S. Kul'varskaya

UDC 621.362;621.039.542.344

The Langmuir method was used in combination with the Becker method to investigate the evaporation rates of carbide thermionic cathodes. Data were obtained concerning the values of the evaporation rates of cathodes of ZrC, UC, and their solid solutions. It was found that UC has the fastest evaporation rate and ZrC has the slowest; the solid solutions occupy an intermediate position. It was shown that the evaporation rate of a carbide cathode depends on its backing.

For the past few years there has been a great deal of interest in the study of the thermoemissive properties of carbides, borides, and other high-melting compounds that can be used as the material for the cathodes of thermoelectronic devices for converting heat energy into electrical energy [1-3].

In particular, a report has already been published concerning the practical use of ZrC-UC solid solutions for converting nuclear (thermal) energy into electrical energy [4].

It is known that an important factor in selecting the material for a thermoelectronic cathode is its service life, which is strongly dependent on the evaporation rate of the emitting substance. The evaporation rate also determines the range of operating temperatures, or more precisely, the optimum temperature of cathode operation.

Today we know many direct and indirect methods of the most varied kinds for determining the vapor pressure of materials [5]. Among the most widespread are the Langmuir method [6] and the Knudsen effusion method [7].

Because of the low evaporation rate of carbides, which makes it necessary to heat a specimen to a very high temperature in order to obtain data on its vaporizability (for example, in the case of ZrC, a temperature of 2000°K or higher), the use of the effusion method involves considerable difficulty. For this reason, in the present study, the author used the Langmuir method, based on determining the pressure by measuring the rate of evaporation from an open surface.

An important drawback of this method is the lack of data on the values of the Langmuir coefficient (and this may be markedly different from unity), as well as the indeterminacy of the surface area.

Usually, the evaporation rate is calculated on the basis of the weight of material evaporating over a fixed period of time. However, this method has serious disadvantages: first of all, the exposure time required is very long, and, secondly, after the experiment the evaporated material is weighed in air, which in some cases may lead to serious errors, especially with hygroscopic materials.

These drawbacks are eliminated to a considerable extent in the Becker emission method, which enables us to determine the evaporation rate directly in the vacuum apparatus when it is pumped out. This method has been widely used recently for determining the rate of evaporation of barium from ("L" cathodes, impregnated cathodes, etc.) [8, 9].

The Becker method is based on the well-known phenomenon that the work function of the metal backing changes when a number of electropositive metals (barium, cesium, thorium, etc.) are adsorbed onto its surface.

Becker himself showed that in the process of depositing barium onto tungsten, the thermionic emission increases from the values characteristic of pure tungsten to some maximum value corresponding to the deposition of a monolayer onto the tungsten [10].

Translated from *Atomnaya Energiya*, Vol. 21, No. 5, pp. 368-375, November, 1966. Original article submitted August 26, 1965; revised February 1, 1966.

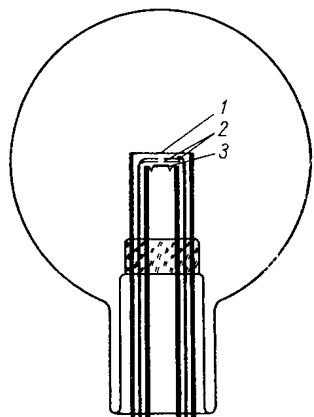


Fig. 1. Schematic diagram of experimental apparatus: 1) tungsten ribbon; 2) screens; 3) evaporator.

In determining the evaporation rate by this method, we must measure the time required for the current from the tungsten ribbon to reach its maximum value, and this time is taken to be the formation time of one monolayer.

Design of the Experimental Apparatus and Investigation Procedure

The Becker method can be used for determining the amount of carbide evaporated only if a thermoemission maximum is observed when the carbides are deposited onto the tungsten. Anticipating our results somewhat, we may say at this point that such a maximum actually exists (see Figs. 2 and 3) and is determined by the carbide layer on the tungsten surface, as was shown by the data of our mass-spectrometric analysis.

The design and geometry of the electrode system of the evaporator of the experimental apparatus, are somewhat analogous to those described in [11]. The system consists of two diaphragms, at the center of which are openings 2 mm in diameter, placed at a fixed distance from each other and from the object; the advantage of such a system consists in the fact that it considerably reduces the "penumbra" on the target (this was verified by means of a model with a source of light).

Tantalum and rhenium ribbons were used as the evaporator for this material. The reason tantalum and rhenium were chosen as the backing material for cathodes made of uranium carbide, zirconium carbide, and the like is that, according to the available literature data, tantalum is almost completely non-reactive with ZrC and UC in the temperature range under investigation (2000-2300°K for ZrC and 1700-1900°K for UC), at least for a period of several hours. As for rhenium, it is well known that this material is much more passive than tantalum.

The ribbon carrying the carbide layer was heated by passing a current directly through it. The evaporating substance was condensed on a tungsten ribbon 50 μ thick.

A schematic diagram of the apparatus is shown in Fig. 1.

The procedure used in handling the experimental apparatus was the following: The apparatus was annealed at a temperature of $t \approx 450^\circ\text{C}$, the tantalum evaporator carrying the carbide layer was annealed for a few minutes at pale red heat, and the tungsten ribbon (the cathode) was annealed at $t \approx 2000^\circ\text{C}$.

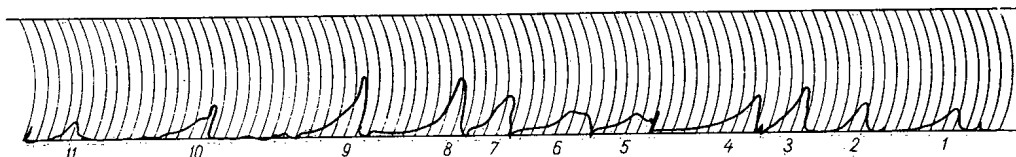


Fig. 2. Recorder strip showing thermoemission current as a function of time for ZrC: 1) $t = 1600^\circ\text{C}$, $\tau = 2.75$ min; 2) $t = 1633^\circ\text{C}$, $\tau = 2.1$ min; 3) $t = 1653^\circ\text{C}$, $\tau = 1.9$ min; 4) $t = 1680^\circ\text{C}$, $\tau = 1$ min; 5) $t = 1700^\circ\text{C}$; 6) $t = 1700^\circ\text{C}$; 7) $t = 1685^\circ\text{C}$; 8) $t = 1670^\circ\text{C}$, $\tau = 1.65$ min; 9) $t = 1660^\circ\text{C}$, $\tau = 1.6$ min; 10) $t = 1650^\circ\text{C}$, $\tau = 0.85$ min; 11) $t = 1600^\circ\text{C}$, $\tau = 5.3$ min.

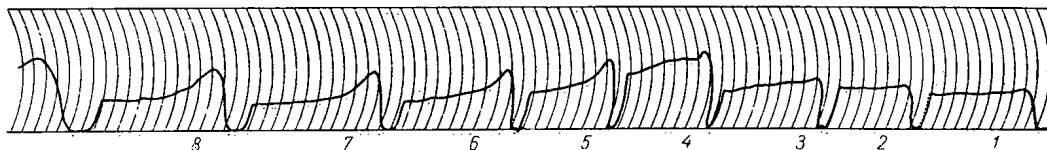


Fig. 3. Recorder strip showing thermoemission current as a function of time for UC: 1) $t = 1465^\circ\text{C}$, $\tau = 2.5$ min; 2) $t = 1485^\circ\text{C}$, $\tau = 2.3$ min; 3) $t = 1500^\circ\text{C}$, $\tau = 1.75$ min; 4) $t = 1490^\circ\text{C}$, $\tau = 1.75$ min; 5) $t = 1470^\circ\text{C}$, $\tau = 1.6$ min; 6) $t = 1440^\circ\text{C}$, $\tau = 2.1$ min; 7) $t = 1420^\circ\text{C}$, $\tau = 2.75$ min; 8) $t = 1440^\circ\text{C}$, $\tau = 3.5$ min.

Temperature, °K	2050	2100	2150	2175	2200	2275
Evaporation rate, $\text{g cm}^{-2}\text{sec}^{-1}$:						
ZrC on tantalum backing	$\sim 2 \cdot 10^{-9}$	$3 \cdot 10^{-9}$	$8 \cdot 10^{-9}$	$\sim 1 \cdot 10^{-8}$	-	-
ZrC on rhenium backing	-	-	-	$1.1 \cdot 10^{-9}$ ($1.4 \cdot 10^{-9}$ at the conclusion of measurements)	$2 \cdot 10^{-9}$	$3 \cdot 10^{-9}$

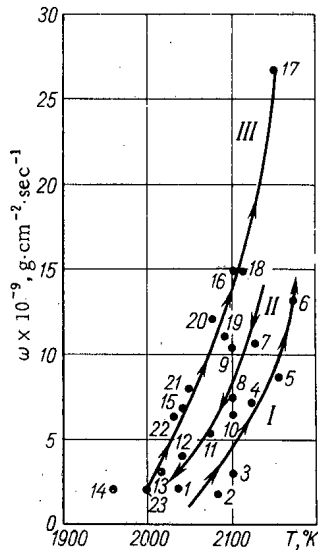


Fig. 4.

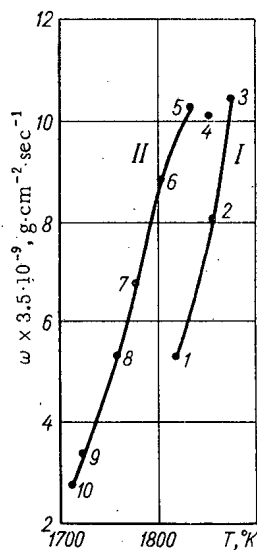


Fig. 5.

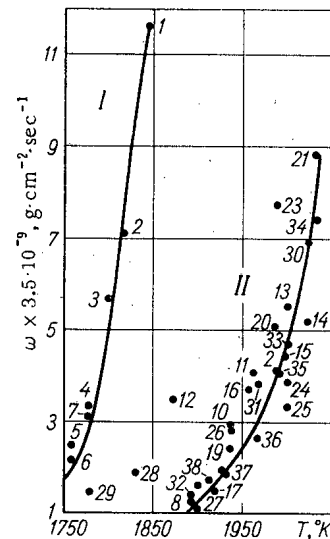


Fig. 6.

Fig. 4. Evaporation rate of ZrC cathodes as a function of temperature. The numbers of the points on Figs. 4-8 indicate the order in which the measurements were made.

Fig. 5. Evaporation rate of UC cathodes as a function of temperature: I) start of experiment; II) end of experiment.

Fig. 6. Evaporation rate of $(\text{ZrC})_{0.7}-(\text{UC})_{0.3}$ cathodes as a function of temperature.

The evaporator temperature was measured by means of an optical pyrometer with a reading accuracy of 1%, and to determine the true temperature, we introduced a correction for the radioemissivity of the tantalum. The temperature of the tungsten ribbon was kept at 700-900°C in order to prevent the evaporation of the carbide from the tungsten ribbon and to prevent any substantial migration of the carbides.

The thermoemission current from the tungsten ribbon was measured by the usual method for anode-current measurements in a diode; the electron collector was used as the upper diaphragm. An N-370 recorder was used to give a continuous recording of how the emission current varied with time for different evaporator temperatures. The measurements were made both when the evaporator temperature was raised and when it was lowered. Such measurement cycles were repeated several times for the same specimen. In addition, a given specimen composition was tested in at least three apparatuses.

Figures 2 and 3 are photographs of the recorder strips showing how the thermoemission current varies as a function of time for different evaporator temperatures.

The resulting curves show the following regularities: 1) the higher the temperature, i.e., the higher the evaporation rate, the more rapidly we will reach the maximum value of the emission current corresponding to the formation of approximately one monolayer of the evaporating substance on the tungsten ribbon; 2) as the evaporation temperature increases, there is usually an increase in the value of the emission current at the maximum.

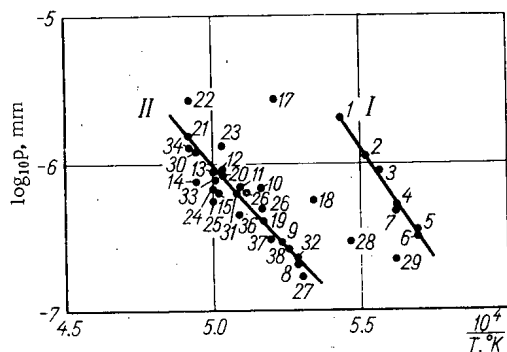


Fig. 7. Saturated vapor pressure of $(\text{ZrC})_{0.7}-(\text{UC})_{0.3}$ as a function of reciprocal temperature when the evaporation process is continued for a long time.

It was suggested that as the evaporator temperature rises, there is an additional heating of the tungsten ribbon owing to the radioemissivity of the hotter evaporator. However, a blank experiment with a tantalum ribbon not carrying a carbide layer did not produce such an effect. Another hypothesis was based on the possibility of a change in the composition in the vapor phase when the temperature increases: it was assumed that the percentage of metallic zirconium in the vapor phase of the ZrC and the percentage of uranium in the UC increased, with the result that the work function of the tungsten would be further decreased by the formation of a zirconium or uranium film on the tungsten or the carbide. Mass-spectrometric data actually showed a change in the composition in the vapor phase; as the temperature increases, there is an increase in the percentage of the zirconium in the ZrC vapor. This appears to confirm the second hypothesis.

In calculating the evaporation rate, I started from the assumption that the vapor phase of each monocarbide consists of molecules of the carbide in question but the vapor phase of the ZrC-UC double carbide consists of molecules of UC, which evaporate more easily than ZrC. As it turned out, this assumption was not entirely correct. Mass-spectrometric investigation showed that the vapor phase of ZrC always contains some metallic zirconium, even if only a very small amount, and this amount increases with temperature; this is apparently the result of a reaction between the tantalum backing and the carbide layer, and the reaction is very slow at low temperatures but becomes more rapid as the temperature rises. For this reason, the composition of the vapor phase will depend to a considerable extent on the material of the backing which carries the carbide.

The second assumption was that the maximum of the emission current corresponds to depositing one monolayer of the evaporating substance onto the tungsten. At the same time, it is known that this maximum occurs when the surface is covered not with one monolayer but with a fraction of one [12, etc.]. Moreover, it has been shown in a number of studies that this maximum may not exist at all or may be rather flat and cover a range equal to fractions of a monolayer (see, for example, [13]). However, reliable studies made in recent years have shown that the extremal value of the work function $\phi(\theta)$ (where θ is the degree of covering) corresponds to a monatomic layer [14]. I found that the carbide emission does have a rather well-defined maximum (see Figs. 2 and 3) caused by the layer of carbide on tungsten.

The evaporation rate of the substance under investigation was found from the formula

$$\omega = \frac{g}{\tau S f} \text{ g.cm}^{-2}.\text{sec}^{-1},$$

where g is the weight of the monolayer deposited onto the tungsten ribbon; τ is the time required to form the monolayer; S is the surface area of the evaporator; f is a geometric factor determining the fraction of the evaporating substance which hits the tungsten ribbon.

The value of τ is found directly by experiment; f depends on the geometry of the apparatus.

The amount of evaporated substance was calculated by means of known formulas, with the actual density distribution replaced by an ideal distribution.

The density of the monolayer was calculated as follows: I determined the number of ZrC or UC molecules in the ZrC or UC monolayer and calculated the weight of the monolayer from this. For ZrC the weight was $9.4 \cdot 10^{-8} \text{ g/cm}^2$, while for UC and for ZrC-UC it was $g = 2.7 \cdot 10^{-7} \text{ g/cm}^2$. The geometric factor f , expressing the ratio of the amount of the substance hitting the target (the tungsten ribbon) to the total amount of evaporated substance was calculated by using a known formula of [14], into which the appropriate values of aperture diameter and object-to-diaphragm distance were substituted for each experimental apparatus.

From the experiments I found the time required for the thermionic emission to reach a maximum, which, according to the hypothesis, corresponds to the time required to form a monolayer of the evaporated substance on the tungsten ribbon.

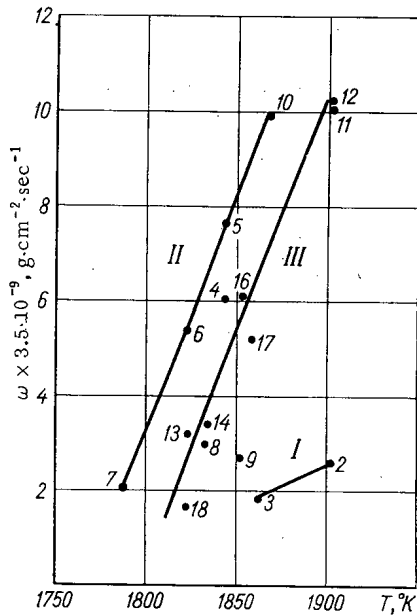


Fig. 8. Evaporation rate of $(\text{ZrC})_{0.7}-(\text{UC})_{0.3}$ cathodes as a function of temperature when the evaporation process is continued for a long time.

For example, if at the start of the measurements (curve I) we had $\omega \approx 5 \cdot 10^{-9} \text{ g}\cdot\text{cm}^{-2}\cdot\text{sec}^{-1}$ at $t = 2100^\circ\text{K}$, then at the end of our measurements, after about 2-3 h, the value will be more than $1 \cdot 10^{-8} \text{ g}\cdot\text{cm}^{-2}\cdot\text{sec}^{-1}$, i.e., more than twice as large (curve III). (Curve II was obtained for intermediate experimental conditions.)

This is apparently due to the reaction between the ZrC and the tantalum backing, which takes place slowly at such temperatures. The zirconium liberated by this reaction evaporates rapidly, and consequently the ω value for ZrC will increase with time. As mentioned above, this hypothesis was confirmed by the mass-spectrometric data.

It is of interest to note that the evaporation rate of ZrC on a rhenium backing is considerably lower than that of ZrC on a tantalum backing. Thus, for example, the value of ω is $1.1 \cdot 10^{-9} \text{ g}\cdot\text{cm}^{-2}\cdot\text{sec}^{-1}$ for ZrC on a rhenium backing at $T = 2175^\circ\text{K}$ but $1 \cdot 10^{-8} \text{ g}\cdot\text{cm}^{-2}\cdot\text{sec}^{-1}$ for ZrC on a tantalum backing at the same temperature.

Evaporation Rate of UC Cathodes. The temperature range of the measurements was $1718-1893^\circ\text{K}$. In this temperature range the evaporation rate ω varies from about $9 \cdot 10^{-9}$ to about $4 \cdot 10^{-8} \text{ g}\cdot\text{cm}^{-2}\cdot\text{sec}^{-1}$, and the saturated vapor pressure P varies from about $3 \cdot 10^{-7}$ to about $2 \cdot 10^{-6} \text{ mm Hg}$, respectively.

Figure 5 shows typical curves for $\omega = f(T)$.

It can be seen from the graph that for UC, just as for ZrC, the evaporation rate increases with time. However, this effect is less pronounced for UC than for ZrC.

Evaporation Rate of Cathodes Made of ZrC-UC Solid Solutions. In addition to the cases of ZrC and UC monocarbides, the evaporation rate was also measured for solid solutions containing ZrC and UC in a ratio of 0.7:0.3.

If the measurement process is continued only for a short time, the evaporation rate increases with time, just as in the case of ZrC.

If the experiment is continued further, the nature of the situation changes. Toward the end of the measurements, the separation rate decreases. This is illustrated in Fig. 6, in which curve I of the function $\omega = f(T)$ refers to the beginning of the measurements and curve II refers to the end. The results of the vapor pressure determination at the beginning and end of the experiment are shown in Fig. 7.

When we consider, however, that the maximum of the current from the tungsten ribbon may correspond not to a monolayer but to a fraction of one, we see that the value found for the evaporation rate may be too large by about one-third of an order of magnitude.

The zirconium carbide and uranium carbide were manufactured by the powder-metallurgy method. The specimens were subjected to x-ray analysis. The lattice constant was found to be 4.988 kX for the UC and 4.689 kX for the ZrC. The uranium was 98.95% pure; the graphite contained 0.004% impurities, including $1.5 \cdot 10^{-5}\%$ boron.

Results of the Experiments

Evaporation Rate of ZrC Cathodes. Figure 2 is a typical photograph of a recorder strip showing the graphs of emission current as a function of time, $I = f(t)$, obtained for different evaporator temperatures. The temperature range I selected for measuring the evaporation rate of ZrC was $1963-2275^\circ\text{K}$; the minimum time for depositing a monolayer onto the tungsten ribbon was 0.5 min. The table shows the values of ω for ZrC, obtained by averaging the data from three experimental apparatuses (the deviation of individual data from the average did not exceed 30%).

Figure 4 shows a typical graph of the evaporation rate ω as a function of temperature for ZrC on a tantalum backing. It is readily seen that if the evaporation process goes on for a fairly long time, the evaporation rate increases sharply; thus, for example, if at the start of the measurements (curve I) we had $\omega \approx 5 \cdot 10^{-9} \text{ g}\cdot\text{cm}^{-2}\cdot\text{sec}^{-1}$ at $t = 2100^\circ\text{K}$, then at the end of our measurements, after about 2-3 h, the value will be more than $1 \cdot 10^{-8} \text{ g}\cdot\text{cm}^{-2}\cdot\text{sec}^{-1}$, i.e., more than twice as large (curve III). (Curve II was obtained for intermediate experimental conditions.)

This is apparently due to the reaction between the ZrC and the tantalum backing, which takes place slowly at such temperatures. The zirconium liberated by this reaction evaporates rapidly, and consequently the ω value for ZrC will increase with time. As mentioned above, this hypothesis was confirmed by the mass-spectrometric data.

It is of interest to note that the evaporation rate of ZrC on a rhenium backing is considerably lower than that of ZrC on a tantalum backing. Thus, for example, the value of ω is $1.1 \cdot 10^{-9} \text{ g}\cdot\text{cm}^{-2}\cdot\text{sec}^{-1}$ for ZrC on a rhenium backing at $T = 2175^\circ\text{K}$ but $1 \cdot 10^{-8} \text{ g}\cdot\text{cm}^{-2}\cdot\text{sec}^{-1}$ for ZrC on a tantalum backing at the same temperature.

Evaporation Rate of UC Cathodes. The temperature range of the measurements was $1718-1893^\circ\text{K}$. In this temperature range the evaporation rate ω varies from about $9 \cdot 10^{-9}$ to about $4 \cdot 10^{-8} \text{ g}\cdot\text{cm}^{-2}\cdot\text{sec}^{-1}$, and the saturated vapor pressure P varies from about $3 \cdot 10^{-7}$ to about $2 \cdot 10^{-6} \text{ mm Hg}$, respectively.

Figure 5 shows typical curves for $\omega = f(T)$.

It can be seen from the graph that for UC, just as for ZrC, the evaporation rate increases with time. However, this effect is less pronounced for UC than for ZrC.

Evaporation Rate of Cathodes Made of ZrC-UC Solid Solutions. In addition to the cases of ZrC and UC monocarbides, the evaporation rate was also measured for solid solutions containing ZrC and UC in a ratio of 0.7:0.3.

If the measurement process is continued only for a short time, the evaporation rate increases with time, just as in the case of ZrC.

If the experiment is continued further, the nature of the situation changes. Toward the end of the measurements, the separation rate decreases. This is illustrated in Fig. 6, in which curve I of the function $\omega = f(T)$ refers to the beginning of the measurements and curve II refers to the end. The results of the vapor pressure determination at the beginning and end of the experiment are shown in Fig. 7.

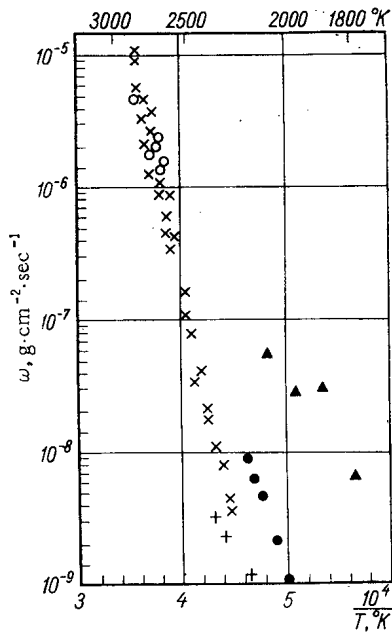


Fig. 9. Data obtained by various authors for the evaporation rate of ZrC as a function of temperature. Data of the present study: ●) for ZrC(Ta), +) for ZrC(Re); Δ) [15]; ×) [16]; ○) [17].

data given above, even though the comparison is made more difficult in some cases by the fact that the measurements were made in different temperature ranges and extrapolation to the required temperatures is not always possible.

Figure 9 shows the values obtained by various authors [15-17] for the evaporation rate of ZrC at different temperatures; the same figure also shows the data on the evaporation rate of ZrC on tantalum and rhenium backings, obtained in the present study. It is readily seen that the data are in reasonably good agreement (within less than one order of magnitude).

As for UC, in [18-20] the temperature range of the measurements was 2000-2820°K, while in the present study the evaporation rate was investigated up to 2000°K. At this temperature the saturated vapor pressure of UC is approximately $3.8 \cdot 10^{-10}$ atmospheres, while according to the data of [19] it is approximately $4 \cdot 10^{-10}$ atmospheres.

The data available in the literature with regard to the evaporation rates of ZrC-UC refer to temperature ranges of 2000-2400°K (for ZrC-UC combinations with a high percentage of UC) and above 2100°K (for ZrC-UC combinations containing 15-20% UC). The temperature range I selected for my measurements was 1800-2085°K. According to the data of [21], $\omega = 10^{-9}$ g·cm⁻²·sec⁻¹ when T=2000°K, while according to the results of the present study $\omega \approx 3 \cdot 10^{-8}$ g·cm⁻²·sec⁻¹; as in [21], the evaporation rate decreased when the cathodes were heated for a long time.

A comparison of the results obtained in the present study for the evaporation rates of monocarbides and binary solid solutions shows that uranium carbide has the highest evaporation rate and, correspondingly, the highest saturated vapor pressure, and zirconium carbide has the lowest; the values for the solid solutions are intermediate between these.

Thus, an evaporation rate of approximately 10^{-8} g·cm⁻²·sec⁻¹ is obtained with UC at a temperature of 1800-1850°K; with ZrC on a tantalum backing, at 2175°K; with ZrC on a rhenium backing, at 2300°K; and with (ZrC)_{0.7}-(UC)_{0.3}, at 1800-2000°K, depending on the duration of the experiment.

If we assume that the lifetime of a carbide cathode for a thermoelectronic converter depends only on the evaporation rate of the active material, the lifetime of cathodes made up of the carbides investigated

The straight line representing the equation $\log_{10} p = f(1/T)$ at the end of the experiment (see Fig. 7, II) has a slope different from that of line I, which shows that the heat of vaporization of the carbide changes with time.

Figure 8 shows three $\omega = f(T)$ curves obtained in one apparatus; curve I represents the beginning of the experiment, II represents the middle, when the evaporation rate increases because of the reaction between the ZrC-UC and the tantalum backing, and, lastly, III represents the end of the measurements, when some fraction of the more easily vaporized UC has already evaporated from the layer, so that the evaporation rate of the material is decreased.

The temperature range of the measurements for the (ZrC)_{0.7}-(UC)_{0.3} binary carbide is 1800-2085°K. Each measurement cycle, including heating and cooling the evaporator, took about 2 h.

Evaluation of the Results

The literature available today includes many studies describing the results of investigations on the evaporation rate of carbides, including zirconium carbide and uranium carbide [15-21].

However, the investigation procedure used in these studies differs considerably from the procedure selected in the present study. The advantage of the latter procedure is that the evaporation rates of the materials can be determined in a much shorter time and at relatively low temperatures. This makes it possible to observe the change in evaporation rate as a function of time. It is of some interest to compare the evaporation rate data obtained by different authors with

here will amount to thousands of hours at these temperatures (for actual thicknesses of the layer on the core), and therefore these temperatures (or even higher ones) are entirely acceptable as operating temperatures.

However, we must also bear in mind other factors influencing cathode lifetime: first the evaporation rate of the carbides may increase under certain circumstances; secondly, in some cases, e.g., for UC, the cathode lifetime may be shortened by a large drop in the thermionic emission with increasing time [22]; thirdly, we do not yet understand the behavior of the carbide cathode in the cesium vapors with which the thermoelectronic converter is filled.

All of these questions will have to be studied in detail, and at the present state of investigations it is impossible to predict exactly the lifetime of a carbide cathode under real operating conditions in a thermoelectronic converter used for converting nuclear (thermal) energy into electrical energy.

LITERATURE CITED

1. T. L. Matskevich et al., ZhTF, 32, 1266 (1962); T. L. Matskevich and T. V. Krachino, ZhTF, 32, 233 (1962).
2. R. Pidd et al., J. Appl. Phys., 30, 1575 (1959).
3. J. Ingold, J. Appl. Phys. 34, 2033 (1963).
4. R. W. Pidd et al., Direct Conversion of Thermal to Electrical Energy [Russian translation]. Collection of Translations. Moscow, Gosatomizdat, p. 133 (1961).
5. A. N. Nesmeyanov, Vapor Pressure of Chemical Elements [in Russian]. Moscow, Izd-vo AN SSSR (1961).
6. I. Langmuir, Phys. Zeitschrift, 14, 1233 (1913).
7. M. Knudsen, Ann. Physik, 28, 75 (1905); Ann. Physik, 29, 179 (1909).
8. I. Brodie and R. Jenkins, J. Electronics, 2, 457 (1957).
9. I. Brodie and R. Jenkins, J. Electronics, 2, 33 (1956).
10. J. Becker, Trans. Amer. Electrochem. Soc., 55, 53 (1929).
11. K. S. Beinar and B. P. Nikonov, Radiotekhnika i Élektronika, 10, 476 (1965).
12. I. Langmuir, J. Amer. Chem. Soc., 54, 2798 (1932).
13. E. P. Gyftopoulos and J. D. Levine, Effective Thermionic Cathodes [Russian translation]. Collection of Translations, No. IV, Moscow, Énergiya, p. 237 (1964).
14. V. N. Shrednik, Dissertation, Leningrad, (1965); [in Russian] High-Temperature Technology. Collection edited by I. E. Campbell [Russian translation], Moscow, Izd-vo inostr. lit., p. 485 (1959).
15. A. S. Bolgar, T. S. Verkhoglyadova, and G. V. Samsonov, Izv. AN SSSR, Ser. Metallurgiya i toplivo, 1, 142 (1961).
16. I. Koffman et al., WADD-TR-646, p. II (1963).
17. B. Pollock, J. Phys. Chem., 65, 731 (1961).
18. J. Leitnaker and W. Witteman, J. Chem. Phys., 36, 1445 (1962).
19. H. Erick et al., Thermodynamics of Nuclear Materials. TAEA-549 (1962).
20. L. Eberle, Atomwirtschaft, 9, 223 (1964).
21. A. Weinberg et al., General Atomic Report GE-3007, (1962).
22. B. S. Kul'varskaya et al., Radiotekhnika i Élektronika, 8, 675 (1963).

All abbreviations of periodicals in the above bibliography are letter-by-letter transliterations of the abbreviations as given in the original Russian journal. Some or all of this periodical literature may well be available in English translation. A complete list of the cover-to-cover English translations appears at the back of the first issue of this year.

FORMATION OF POLYMER PRODUCTS IN THE RADIOLYSIS OF
MIXTURES OF HEXAFLUOROBENZENE WITH PERFLUORO-
CYCLOHEXANE AND PERFLUORONONANE

V. A. Khramchenkov

UDC 541.15:678.7

The dependence of the formation of polymer products in the (n, γ) -irradiation of mixtures of hexafluorobenzene with perfluorocyclohexane and *n*-perfluorononane upon the concentration of hexafluorobenzene was determined. A hypothesis was formulated on the inhibiting effect of hexafluorobenzenes in the radiolysis of perfluorocyclohexane. It was established that in the radiolysis of *n*-perfluorononane, hexafluorobenzene plays the role of a polymerization-initiating agent.

The unique properties of organochlorine compounds, for example, their high thermal stability (up to 600°C in perfluorinated polyphenyls [1]) and their chemical inertness, have been responsible for their wide use in the atomic energy industry [2]. Progress in this field sets new requirements for such compounds – requirements of radiation-thermal stability. The combination of sufficiently high radiation-thermal stability of fluorocarbons, which is possessed by perfluorinated polyphenyls [3], with the low neutron absorption cross section fluorine atoms opens up broad prospects for the use of these compounds in nucleonics. The absence of molecular fluorine as a radiolysis product, as well as the absence of any corrosive action of the other radiolysis products on aluminum [3, 4], once again confirms the possibility of using fluorocarbons.

As is well known, aromatic hydrocarbons exert an inhibiting effect upon the radiolysis of aliphatic hydrocarbons. However, there are no data in the literature on an analogous influence of perfluorinated aromatic compounds on the radiolysis of aliphatic fluorocarbons, in view of which in this work we determined the dependence of the formation of high-boiling products ("polymer") on the concentration of hexafluorobenzene in (n, γ) -irradiation of its mixtures with perfluorocyclohexane and *n*-perfluorononane. The radiolysis of such mixtures is interesting from the standpoint of the protective action of aromatic compounds in various compositions. Irradiation was conducted in molybdenum glass ampoules.

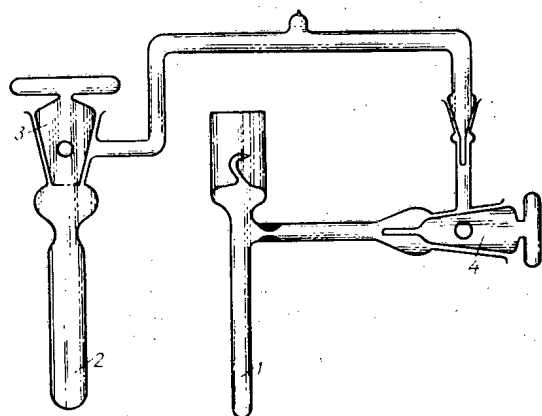


Fig. 1. Cell for filling of ampoules.

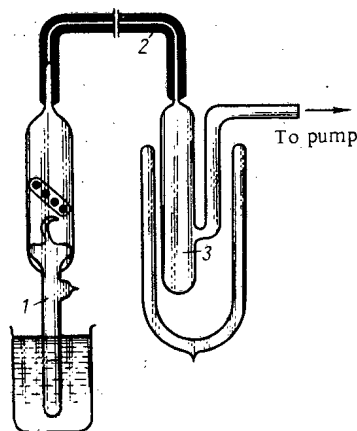


Fig. 2. Scheme of isolation of high-boiling radiolysis products.

Translated from *Atomnaya Energiya*, Vol. 21, No. 5, pp. 375-378, November, 1966. Original article submitted March 18, 1966.

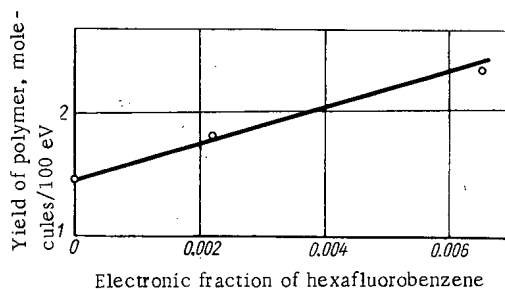


Fig. 3. Dependence of the yield of high-boiling radiolysis products on the electronic fraction at hexafluorobenzene concentrations of 0-0.5 M.

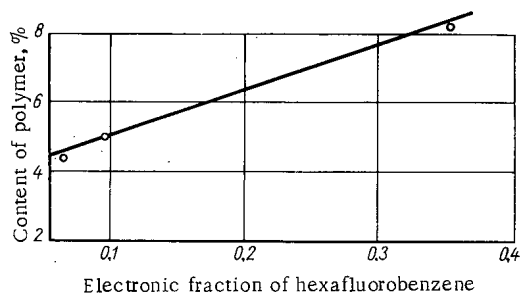


Fig. 4. Dependence of yield of high-boiling radiolysis products on the electronic fraction at hexafluorobenzene concentrations of 0.5-4 M.

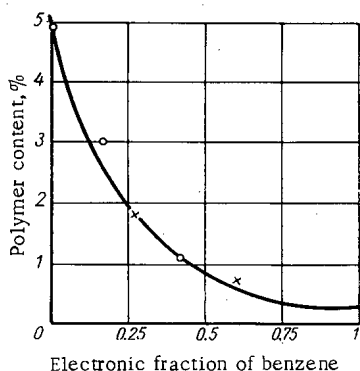


Fig. 5. Dependence of the yield of high-boiling radiolysis products of mixtures of benzene with cyclohexane upon the electronic fraction of benzene: O) fluorocarbons; X) hydrocarbons.

Since a large error in the concentration of hexafluorobenzene might appear in the preparation of the ampoules for irradiation, in the cases of n-perfluorononane, the following specially developed method was used. After degasification by repeated alternation of the processes of freezing and melting under vacuum, the weight of a sample of n-perfluorononane in ampoule 1 (Fig. 1) was determined, considering the weight of the lubricant on the ground joints. Before each operation of filling, degasification of hexafluorobenzene in ampoule 2 was also carried out. After degasification of the cell for the filling, it was sealed off at a residual pressure of $\sim 10^{-3}$ mm Hg. Hexafluorobenzene was frozen out in ampoule 1 with liquid nitrogen directly from ampoule 2 or (if the mixtures were prepared with a low hexafluorobenzene concentration), from the tube between stopcocks 3 and 4, filled with vapor, by turning stopcock 3. The amount of hexafluorobenzene vapors in the tube varied depending upon the temperature of ampoule 2.

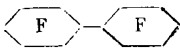

Irradiation was conducted at $\sim 50^\circ\text{C}$ in the water-filled experimental channel of the VVR-2 reactor of I. V. Kurchatov Atomic Energy Institute. The dose of absorbed energy was determined according to calorimetric data in the irradiation of polyterafluoroethylene with a correction of electron density. In the case of mixtures of n-perfluorononane, the dose corresponded to 66 Mrad of energy absorbed by hexafluorobenzene; in the case of perfluorocyclohexane the dose was 60 Mrad.

The polymer radiolysis products were isolated by simple distillation with continuous evacuation ($\sim 10^{-3}$ mm Hg) through a trap 3, cooled with liquid nitrogen, and connected to ampoule 1 by a flexible vacuum hose 2 (Fig. 2). The inner branch of ampoule 1 was broken with a glass breaker with steel balls inside. The redistillation was conducted at a temperature of 100°C to a constant weight of ampoule 1.

Figures 3 and 4 present the values of the yields of the polymer products as a function of the electronic fraction of hexafluorobenzene in the mixture with n-perfluorononane. At low concentrations, the yield of polymer products (see Fig. 3) is expressed by the number of molecules of n-perfluorononane converted to polymer products with the absorption of 100 eV of energy.

The yields of the polymer products increase as a linear function of the hexafluorobenzene concentration; the calculated content of the polymer in the mixtures (according to the yield in individual components) is lower than the experimental value. This interesting fact is probably associated with the specific properties of organofluorine compounds. In contrast to hydrocarbons, in normal, alicyclic, and aromatic fluorinated compounds, these properties are manifested in approximately identical radiation chemical yields of the polymer products (see Table 1). It should be emphasized that frequently fluorinated aromatic compounds are more inclined to polymerize under the action of ionizing radiations than are perfluorinated saturated fluorocarbons of normal and cyclic structure.

TABLE 1. Radiation Chemical Yields of Polymer Products of Various Organofluorine Compounds

Compound	Yield of polymer, molecules/100 eV	Method of irradiation	Literature
C ₆ F ₆	2.15	Electron irradiation (~ 30° C)	[5]
C ₆ F ₆	2.25	Irradiation in a nuclear reactor (~ 50° C)	Data of this work
C ₆ F ₁₂	2.1	Electron irradiation (90° C)	[5]
C ₆ F ₁₂	2.7	Irradiation in a nuclear reactor (~ 50° C)	Data of this work
C ₆ F ₅ -C ₆ F ₅	1.4	γ-radiation (100° C)	[3]
	0.9	Electron irradiation (122° C)	[5]
	1.4	Electron irradiation (~ 30° C)	[5]
n-C ₉ F ₂₀	1.5	Irradiation in a nuclear reactor (~ 50° C)	Data of this work
n-C ₇ F ₁₆	1.8	Irradiation in a nuclear reactor (110° C)	[4]

Since the linearly increasing yield of the polymer in mixtures of hexafluorobenzene with n-perfluorononane exceeds the yield of the polymer both of pure n-perfluorononane (4.45%) and of pure hexafluorobenzene (2.87%), and since the content of the polymer in the mixtures calculated according to the yields in individual components is below that detected experimentally, it may be assumed that, on the one hand, hexafluorobenzene in the mixtures is an agent that initiates polymerization, and on the other hand, at low concentrations of p-perfluorononane, the latter increases the tendency of hexafluorobenzene of polymerize. The correctness of these hypotheses is confirmed by the linear increase in the coefficient of refraction of the polymer products in mixtures with increasing electronic fraction of hexafluorobenzene, the refractive increment of the double bond of which is large.

One of the facts relating to the specificity of organofluorine compounds is the greater (in comparison with hydrocarbons) ability of hexafluorobenzene to form radicals. Thus according to the data of I. I. Chkheidze (Institute of Chemical Physics, Academy of Sciences of the USSR), the radiation yield of radicals in electron irradiation of hexafluorobenzene in the solid phase (-170°C) is equal to 0.18-0.20/100 eV, i. e., twice as great as the yield of radicals of the hydrocarbon benzene under the same conditions (0.1/100 eV).

In contrast to mixtures of hexafluorobenzene and n-perfluorononane, in the irradiation of mixtures of the former with perfluorocyclohexane, a decrease in the yield of polymer products with increasing electronic fraction is observed; moreover, the yields of the polymer are substantially below the calculated values. Considering this, and also comparing the yields of the polymer products in mixtures of fluorocarbons with the yields in mixtures of the corresponding hydrocarbons in irradiation in one series (Fig. 5), a definite conclusion can be drawn on the inhibiting effect of hexafluorobenzene in the radiolysis of perfluorocyclohexane. On the other hand, perfluorocyclohexane reduces the ability of hexafluorobenzene to polymerize.

As for the mechanism of the initiation of radiation polymerization of n-perfluorononane by hexafluorobenzene and the increase in the tendency of hexafluorobenzene to polymerize in the presence of p-perfluorononane, no definite conclusions can be drawn on the basis of the data of this work. One of the causes of the detected dependences may be (on the basis of the molecular properties of organofluorine compounds) a tendency to form conjugated systems of molecules and radicals.

Further investigations are being carried out.

In conclusion, the author would like to thank I. P. Prokudin for providing the compounds.

LITERATURE CITED

1. L. Wall, R. Donadio, and W. Pummer, *J. Amer. Chem. Soc.*, 82, 4846 (1960).
2. I. L. Knunyants and A. V. Fokin, *Conquest of the Impregnable Element* [in Russian], Moscow, Izd. AN SSSR, p. 4 (1963).
3. F. Bloch and D. Mackenzie, *Radiation Stability of Some Liquid Fluorocarbon Systems at Elevated Temperatures*, Meeting of American Nuclear Society, San Francisco (1964).
4. J. Simons and E. Taylor, *J. Phys. Chem.*, 63, 636 (1959).
5. D. Mackenzie, F. Bloch, and R. Wiswall, *J. Phys. Chem.*, 69, 2526 (1965).

CHANGES IN THE PROPERTIES OF ION EXCHANGERS AFTER PROLONGED USE IN THE PURIFICATION OF RADIOACTIVE WASTE WATER

F. V. Rauzen and Z. Ya. Solov'eva

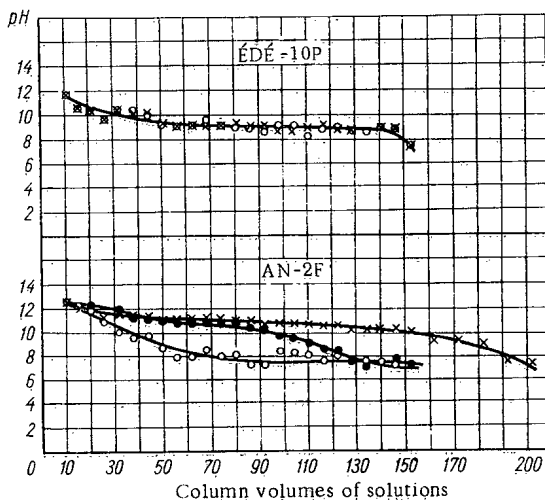
UDC 621.039.7:66.074.7

Experimental data on changes taking place in the properties of ion exchangers after prolonged use in the purification of low-activity waste water in an experimental industrial plant designed for the purification of laboratory waste are presented. Under those conditions the ion exchangers become darkened and break up. The dynamic exchange capacity falls by 30 to 45%. The coefficients representing the purification of the solutions from Cs^{137} , Sr^{90} , and S^{35} are nevertheless no lower than those achieved with new ion exchangers. The capacity of anion exchanger AN-2F may be increased by 20% after treating with a 0.5 N solution of nitric acid. After three years operation, the ion exchangers are still suitable for further use in the purification plant.

An experimental industrial plant for the purification of laboratory waste water uses cation exchanger KU-2 and anion exchangers AN-2F and ÉDÉ-10P for removing radioactive isotopes from clarified waste water. The ion exchangers are regenerated periodically as their exchange capacity becomes exhausted: the cation exchangers with a 1.5 N solution of nitric acid, and the anion exchangers with a 0.5 N solution of sodium hydroxide. The solutions subjected to ion-exchange purification are characterized by a high content of organic materials and complexing reagents used for the deactivation of overalls, rooms, vessels, hands and so on. The oxidation (Kubel') of these solutions requires 30 to 100 mg O_2 /liter. The oxidizability of the water purified in the plant is no greater than 3 to 7 mg O_2 /liter, i.e., the organic materials are sorbed by the ion exchangers [1].

It is well known that, after prolonged use in the purification of water, ion exchangers are subject to aging, the properties of the anion exchangers changing more than those of the cation exchangers. This is because, first, the anion exchangers absorb the organic substances from the water, and secondly, in the course of desalinization the cation-exchanger decomposition products fall on the anion exchangers [2]; the aging of the anion exchangers is accelerated considerably if they are placed after the sulfonated coal [3]. An indirect sign of the aging of the anion exchangers is the specific flow of water used in washing away the excess of regeneration alkali. The amount of water used for this purpose rises rapidly for anion exchangers which have been in service for a long time [4, 5].

The aging of the anion exchangers depends on the composition of the water and leads to a reduction in their term of service. Usually for weakly-basic anion exchangers the period of service is about 6 years. In practice it may be either longer or shorter [3, 6, 7]. It is probable that aging of the ion exchangers also takes place when using ion exchangers for the purification of radioactive waste water, but nothing on this appears



Variation in the pH of the washing water:
○) original anion exchanger; ×) anion exchanger of the first batch; ●) anion exchanger of the second batch.

Translated from *Atomnaya Énergiya*, Vol.21, No.5, pp.378-381, November, 1966. Original article submitted May 17, 1966.

to have been published. The radiation produced by radioactive isotopes absorbed from low-activity waste water plainly presents no danger to the use of ion-exchange resins. It follows from [8, 9] that, on irradiating ion-exchange resins with electrons up to a dose of 10^{21} eV/g, no change takes place in their properties. In purifying waste water with a radioactivity level of the order of 10^{-6} Ci/liter, the radiation dose is no greater than 10^{17} to 10^{18} eV/liter after one year.

EXPERIMENTAL PART

Two batches of ion-exchange resins were selected from the plant column for testing. The samples of the first batch were taken through the charging door of the columns (from the top), and the second with a probe from different heights in the column. Neither type of sample could be considered as average, but to a fair approximation they characterized the state of ion exchangers after long use in the purification of low-activity waste water. The ion-exchanger samples of the first batch were taken out after 50 and those of the second after 68 regenerations. On average, the duration of the filtering cycle in the plant was 120 column volumes; hence 6000 to 8000 column volumes of solution passed through the ion exchangers under examination (6 to 8 m³ through 1 liter of ion exchanger).

The change in the properties of the ion exchangers after prolonged use was determined by comparing with ion exchangers which had been left ever since charging. In color, the used ion exchangers differed considerably from the original; cation exchanger KU-2 became reddish-brown instead of light-yellow, and anion exchanger AN-2F black instead of brown, while anion exchanger ÉDÉ-10P was brown instead of light-yellow.

Determination of the granulometric composition, bulk specific gravity, and dynamic exchange capacity (DEC) was carried out by the method indicated in the All-Union State Standards [10]. The capacity of the anion exchangers was also determined after washing them with a 0.5 N solution of nitric acid. The sorbing capacity for radioactive isotopes was verified under static conditions. In our experiments we used the method of agitating the ion exchangers with the solution. In purifying from Sr⁹⁰ and Cs¹³⁷, we used neutral solutions; for P³² and S³⁵ we used acid solutions (pH=2.5). The radioactive isotopes Sr⁹⁰ and Cs¹³⁷ were introduced into the original solution in the form of nitrates, and P³² and S³⁵ in the form of acids.

TABLE 1. Variation in the Granulometric Composition and Bulk Specific Gravity of Ion Exchangers After Long Use *

Ion exchanger	Average grain diameter, mm	Inhomogeneity factor	Bulk specific gravity, g/ml		Change in bulk weight on moistening
			Air-dry ion exchanger	Moist ion exchanger	
KU-2†	0.64	1.8	-	-	-
KU-2 (original)	0.66	3.1	0.83	0.4	2.1
KU-2 (first batch)	0.53	3.4	0.83	0.4	2.1
KU-2 (second batch)	0.71	2.5	0.83	0.4	2.1
AN-2F†	0.71	3.0	-	-	-
AN-2F (original)	0.82	3.2	0.53	0.35	1.51
AN-2F (first batch)	0.42	3.1	0.59	0.42	1.41
AN-2F (second batch)	0.79	2.4	0.56	0.42	1.33
ÉDÉ-10P†	-	-	-	-	-
ÉDÉ-10P (original)	1.0	2.9	0.59	0.28	2.1
ÉDÉ-10P (first batch)	0.71	2.5	0.50	0.23	2.2

* Cation exchanger KU-2 used in the H form, anion exchangers AN-2F and ÉDÉ-10P in OH form.

†Data of [11].

TABLE 2. Dynamic Exchange Capacity (DEC) of Ion Exchangers

Ion exchanger	Concentration of solutions, mg-equiv./liter	DEC, mg-equiv./liter ion exchanger	Reduction in capacity, %	DEC after treatment with nitric acid, mg-equiv./liter ion exchanger
KU-2 (original)	3.5 (CaCl ₂)	1900	-	-
KU-2 (first batch)	3.5 (CaCl ₂)	1380	28	-
KU-2 (second batch)	3.5 (CaCl ₂)	1370	27	-
AN-2F (original)	3.5 HCl	1750	-	1770
AN-2F (first batch)	3.5 HCl	960	45	1240
AN-2F (second batch)	3.5 HCl	960	45	1240
ÉDÉ-10P (original)	3.5 HCl	1400	-	1220
ÉDÉ-10P (first batch)	3.5 HCl	800	37	890

TABLE 3. Purification Factor* for Various Radioactive Isotopes in Ion Exchangers

Radioactive isotope	KU-2			AN-2F			ÉDÉ-10P	
	original	first batch	second batch	original	first batch	second batch	original	first batch
Sr ⁹⁰	432	487	420	-	-	-	-	-
Cs ¹³⁷	17	15	15	-	-	-	-	-
P ³²	-	-	-	470	98	128	1100	180
S ³⁵	-	-	-	1120	1385	2830	2750	4170

* Purification coefficient or factor = ratio of specific radioactivities of original and purified solutions.

Tables 1 to 3 show the results. The figure shows the variation in the pH of the solution on washing the anion exchangers regenerated with a 0.5 N solution of caustic soda in distilled water.

The samples of ion exchangers used for a long time in the purification plant had γ and β activity. The radioactivity changed little after washing the cation exchanger with acid and the anion exchanger with alkali.

The radioactive isotopes causing this radioactivity were determined by means of curves giving the absorption of β radiation in aluminum and γ spectrograms, using a USD-1 detector and a pulse analyzer of the AI-100 type. Table 4 shows the results of determining the radioactive isotopes left in the ion exchangers.

DISCUSSION OF RESULTS

The experimental data considered reveal certain changes in the properties of the ion exchangers after prolonged use in purifying low-activity waste water: 1) Anion exchangers AN-2F and ÉDÉ-10P break up; 2) the dynamic exchange capacity of the exchangers diminishes – the cation exchanger by 30% and the anion exchangers by 40 to 45%; 3) the purification factors of the solutions relative to P³² in the anion exchanger diminish; 4) the amphoteric properties of the AN-2F anion exchanger increase, as indicated by the slower fall in the pH of the washing water.

Our investigations indicate that the ion exchangers may be used still further for the desalinization and deactivation of waste water in the purification plant. By comparing the DEC of the first and second batches of samples (differing in period of use), we see that, on increasing the period from 50 to 68 regenerations, there is no diminution in the exchange capacity. The tests on the ion-exchange properties showed that the same purification factors relative to radioactive isotopes were obtained for both new and used ion exchangers. An exception was P³² the sorption of which in the anion exchanger did in fact fall. The P³² component in the water coming into the purification plant was nevertheless extremely small. The capacity of the anion exchangers was lower than that of the original exchangers, but it must be borne

TABLE 4. Composition of Radioactive Isotopes in the Ion Exchangers

Ion exchanger	Total γ -activity, g-equiv. Ra/g	Co ⁶⁰	β -activity of isotopes, Ci/g ion exchanger			
			Sb ¹²⁵	Ru ¹⁰⁶ -Rh ¹⁰⁶	Cs ¹³⁷	Sr ⁹⁰ -Y ⁹⁰
KU-2 (first batch)	1.3·10 ⁻⁹	6·10 ⁻¹⁰	-	5·10 ⁻¹⁰	Exists*	5.9·10 ⁻¹⁰
KU-2 (second batch)	1.9·10 ⁻⁹	1.1·10 ⁻⁹	-	1.5·10 ⁻¹⁰	3·10 ⁻¹⁰	9.8·10 ⁻¹⁰
AN-2F (first batch)	0.7·10 ⁻⁹	3·10 ⁻¹⁰	6·10 ⁻¹⁰	3.3·10 ⁻¹⁰	-	-
AN-2F (second batch)	0.6·10 ⁻⁹	3·10 ⁻¹⁰	6·10 ⁻¹⁰	3.3·10 ⁻¹⁰	-	-
ÉDÉ-10P (first batch)	0.4·10 ⁻⁹	Exists*	Exists*	Exists*	-	-

* Radioactive isotope found qualitatively owing to the low γ -activity.

in mind that, in accordance with the existing technological arrangements at the plant, the cation and anion exchangers went for regeneration at the same time. Since more than half the salts in the waste water are carbonates and bicarbonates, the anion exchangers may even be used when their capacity is not less than 50% of the capacity of the cation exchanger. As indicated, the capacity for the AN-2F anion exchanger may be raised by washing with 0.5 N nitric-acid solution.

It should be especially noted that γ -emitting Co⁶⁰ and Sb¹²⁵ build up in the ion exchangers, particularly the cation exchanger, although their concentration in the solution purified by the ion exchangers is so low as to be indeterminable [12]. Measurements showed that after three years use of the ion exchangers their residual radioactivity was approximately 1 mg-equiv. Ra/ton. This should be remembered when deciding the biological shielding required for the column.

LITERATURE CITED

1. K. A. Bol'shakov et al., In the book "Transactions of the Second International Conference of the Peaceful Use of Atomic Energy. Geneva, 1958" [in Russian]. Contributions of Soviet Scientists. Vol. 4. Moscow, Atomizdat, p. 195 (1959).
2. L. Wirth, Industr. and Engng Chem., 53, 638 (1961).
3. B. A. Bakeev, In the Collection "Theory and Practice of Ion Exchange". Alma-Ata, Izd. AN Kaz. SSR, [in Russian] (1961).
4. F. G. Prokhorov, In the Collection "Theory and Practice of the Use of Ion-Exchange Materials" [in Russian]. Moscow, Izd. AN SSSR, p. 57 (1955).
5. H. Brost, Chem. Labor, and Betrieb, No. 11,455 (1963).
6. H. Busch, Mitt. Verein. Grosskesselbesitzer, 75, 383 (1963).
7. V. P. Shvetsova, Teploenergetika, No.11, 46 (1963).
8. E. D. Kiseleva et al., Zh. fiz. khim. 35, 1822 (1961).
9. V. A. Nikashina et al., In the book "Transactions of the Second All-Union Conference on Radiation Chemistry" [in Russian]. Moscow, Izd. AN SSSR, p. 596 (1962).
10. Ion Exchangers. Testing Methods [in Russian]. GOST 10895-64; GOST 1098-64; 10900-64.
11. K. M. Saldadze et al., Ion-Exchange High-Molecular Compounds [in Russian]. Moscow, Goskhimizdat (1960).
12. D. I. Trofimov and Z. A. Sver'kova, Practices in the Treatment of Low and Intermediate Level Radioactive Wastes. Vienna, IAEA, p.449 (1966).

ABSTRACTS

PROPAGATION OF CAPTURE γ RADIATION IN A
UNIFORM SPHERICAL SHIELD

B. K. Fedyushin

UDC 621.039.538.7

If thermal neutrons emitted isotropically from a spherical source of radius R_0 enter a uniform concentric spherical shell shield of thickness $h = R - R_0$, where they give rise to ν γ 's each of energy ε (MeV) per thermal neutron capture, and if it is assumed that the γ rays are emitted isotropically and cannot penetrate the spherical neutron source, the capture γ dose rate at the outside of the shield is given by [1]

$$P' = \frac{k\mu_a\nu\varepsilon\bar{\Sigma}_a}{2R} \int_{R_0}^R \Phi r dr \int_{R-r}^{\sqrt{r^2-R_0^2}+\sqrt{R^2-R_0^2}} \frac{e^{-\mu r'}}{r'} B_D(\mu r') dr', \quad (1)$$

and the intensity of the capture γ radiation at the outside of the shield is

$$I' = \frac{\nu\varepsilon\bar{\Sigma}_a}{4R^2} \int_{R_0}^R \Phi r dr \int_{R-r}^{\sqrt{r^2-R_0^2}+\sqrt{R^2-R_0^2}} \frac{e^{-\mu r'}}{r'^2} (r'^2 + R^2 - r^2) B_I(\mu r') dr'. \quad (2)$$

In Eqs. (1) and (2), k is a coefficient of proportionality equal to $[1/(6.87 \times 10^4)]$ r·cm³/MeV; μ_a is the absorption coefficient for the capture γ radiation in air; $\bar{\Sigma}_a$ is the average macroscopic cross section for radiative capture of thermal neutrons in the shield; Φ is the thermal neutron flux in the shield; $B_D(\mu r')$ and $B_I(\mu r')$ are respectively the dose and energy buildup factors for a point isotropic source of monoenergetic capture γ radiation in the shield; μ is the attenuation coefficient for capture γ radiation in the shield. The quantities r and r' are shown on the figure. The dose rate at the outside of the shield due to capture γ radiation was calculated from Eq. (1) by elementary diffusion theory, by the Hirschfelder theory, and by the Spencer-Fano theory using Taylor's method.

For elementary diffusion theory $B_D(\mu r') = 1$ and

$$P' = P'_0 = \frac{k\mu_a\nu\varepsilon\bar{\Sigma}_a\Phi_0}{2R} e^{-\kappa R} \times [(I_2 - N_2) - (I_1 - N_1) e^{-2\kappa d}], \quad (3)$$

where

$$I_2 = \int_0^h e^{\kappa z} E_1(\mu z) dz; \quad I_1 = I_2(-\kappa) \quad (4)$$

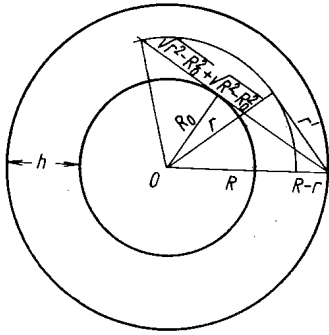
are well known integrals, $E_1(\mu z)$ is the exponential integral of μz , and the integrals

$$N_2 = \int_0^h e^{\kappa z} E_1\{\mu[\sqrt{(R-z)^2 - R_0^2} + \sqrt{R^2 - R_0^2}]\} dz; \quad N_1 = N_2(-\kappa) \quad (5)$$

can only be evaluated numerically for given values of κ , μ , R_0 , and $R = R_0 + h$. In Eqs. (3)-(5) $\kappa = 1/L$ is the reciprocal of the thermal neutron diffusion length in the shield; d is the linear extrapolation length for the thermal neutron flux at the shield-vacuum boundary, and

$$\Phi_0 = \frac{S(1-\beta_0)}{4\pi D [e^{-\kappa R_0}(1 + \kappa R_0) - e^{-2\kappa R'}(1 - \kappa R_0) e^{\kappa R_0}]}, \quad (6)$$

Translated from *Atomnaya Énergiya*, Vol. 21, No. 5, pp. 382-383, November, 1966. Original article submitted November 17, 1965; abstract submitted March 3, 1966.



Cross section of uniform spherical shield.

where D is the diffusion coefficient for thermal neutrons in the shield; β_0 is the albedo of the shield; $R' = R + d$, and S is the number of the thermal neutrons emitted by the source per sec. For the Hirschfelder theory

$$B_D(\mu r') = 1 + \alpha \mu r' + \beta \mu^2 r'^2,$$

where α and β are the coefficients depending only on the γ energy. The final result takes the form

$$P' = P'_0 + \rho', \quad (7)$$

where the positive quantity

$$\rho' = \frac{k\mu_a v \bar{\Sigma}_a \Phi_0}{2R} e^{-\kappa R} [(i_1 + i_3) - (i_2 + i_4) e^{-2\kappa d}], \quad (8)$$

with

$$\left. \begin{aligned} i_1 &= (\alpha + \beta) \left[\frac{e^{(\kappa - \mu)h} - 1}{\kappa - \mu} - e^{-\mu\lambda} \varphi_1 \right]; \\ i_2 &= i_1(-\kappa); \\ i_3 &= \beta \mu \left\{ \frac{1 + [(\kappa - \mu)h - 1] e^{(\kappa - \mu)h}}{(\kappa - \mu)^2} - e^{-\mu\lambda} (\lambda \varphi_1 + \varphi_3) \right\}; \\ i_4 &= i_3(-\kappa), \end{aligned} \right\} \quad (9)$$

where $\lambda = [(2R_0 + h)]^{1/2}$, and the quantities φ_1 and φ_3 are given by the definite integrals

$$\left. \begin{aligned} \varphi_1 &= \int_0^h e^{\kappa z - \mu \sqrt{(R-z)^2 - R_0^2}} dz; \\ \varphi_3 &= \int_0^h e^{\kappa z - \mu \sqrt{(R-z)^2 - R_0^2}} \sqrt{(R-z)^2 - R_0^2} dz, \end{aligned} \right\} \quad (10)$$

which can only be evaluated numerically for given values of κ , μ , R_0 , and $R = R_0 + h$.

Finally in the case of the Spencer-Fano theory using Taylor's method [2]

$$B_D(\mu r') = A_1 e^{-a_1 \mu r'} + A_2 e^{-a_2 \mu r'},$$

where $A_1, A_2 = 1 - A_1$, and a_1 and a_2 are coefficients depending both on the γ energy and on the shield material. The final result is expressed in the form

$$P' = \frac{k\mu_a v \bar{\Sigma}_a \Phi_0}{2R} e^{-\kappa R} \{ A_1 [I_2(\mu_1) - N_2(\mu_1)] + A_2 [I_2(\mu_2) - N_2(\mu_2)] - e^{2\kappa d} [A_1 [I_1(\mu_1) - N_1(\mu_1)] + A_2 [I_1(\mu_2) - N_1(\mu_2)]] \}, \quad (11)$$

where $\mu_1 = \mu(1 + a_1)$ and $\mu_2 = \mu(1 + a_2)$, and the integrals I_1, I_2, N_1 , and N_2 are defined by Eqs. (4) and (5). The expression for the dose rate at the outside of the shield due to capture γ radiation is quite useful for making engineering calculations. The author thanks engineer-physicist A. F. Tverdov for a helpful discussion.

LITERATURE CITED

1. "The Shielding of Nuclear Reactors" [Russian translation]. Collection. Izd. inostr. lit. (1958).
2. Price, Horton, and Spinney, "Radiation Shielding" [Russian translation], Moscow, Izd. inostr. lit. (1959).

APPROXIMATE SOLUTION OF THE DYNAMIC EQUATIONS OF A NUCLEAR REACTOR *

N. G. Chelintsev

UDC 621.039.512

A method is described for solving the equations

$$\frac{dn}{dt} = \frac{\rho - \beta}{l^*} n + \sum_{i=1}^m \lambda_i c_i + s; \quad \frac{dc_i}{dt} = \frac{\beta_i}{l^*} n - \lambda_i c_i$$

for a given time dependence of the reactivity ρ .

For small time intervals formulas are derived by using a special form of perturbation which allows an approximate solution to be found rather simply. For larger time intervals a method of successive approximations, the equivalent decay constant (EDC) method, is discussed. Formulas for determining the error are derived. It is shown that the method is applicable when the solution for $l^* = 0$ is close to the exact solution.

When the reactivity increases monotonically but the power n increases several fold, an approximate method is developed using the inverse period as a variable.

Finally a method of numerical integration is described which appreciably reduces the amount of calculational effort in comparison, for example, with the Cohen-Flatt method for investigating long-term processes.

SOLUTION OF THE DIFFUSION EQUATION IN PERIODIC LATTICES IN TERMS OF TRIGONOMETRIC SERIES †

G. Ya. Rumyantsev

UDC 621.039.51.12

A description is given of an approximate method of solving the diffusion equation in cells of a one-dimensional slab lattice with boundary conditions of the general form given in [1]. It is shown in [1] that the solutions in each cell may be found in the form

$$\Phi = \mathcal{A}\Phi_s + \mathcal{B}\Phi_{as}, \quad (1)$$

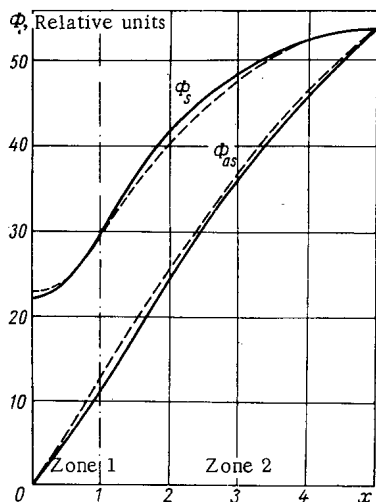
where \mathcal{A} and \mathcal{B} are constants within the boundaries of one cell.

In the present report the functions Φ_s and Φ_{as} are written as the series

$$\left. \begin{aligned} \Phi_s &= \sum_{n=-\infty}^{\infty} A_n \cos \left(\kappa + \frac{n\pi}{a} \right) x; \\ \Phi_{as} &= \frac{1}{\kappa a} \sum_{n=-\infty}^{\infty} A_n \sin \left(\kappa + \frac{n\pi}{a} \right) x, \end{aligned} \right\} \quad (2)$$

* Translated from *Atomnaya Énergiya*, Vol. 21, No. 5, p. 383, November, 1966. Original article submitted March 22, 1966; abstract submitted August 20, 1966.

† Translated from *Atomnaya Énergiya*, Vol. 21, No. 5, p. 384, November, 1966. Original article submitted July 3, 1965; abstract submitted August 30, 1966.



Solutions of the diffusion equation in a cell: ——— series solution; - - - - - exact solution.

The figure shows the results of a calculation for a two zone cell with the following initial data expressed in relative units; lattice pitch $2a = 10$; slug thickness $2b = 2$; in a slug $\Sigma_{tr}^s = 1.2$, $\Sigma_a^s = 0.2$; in the moderator $\Sigma_{tr}^m = 1$, $\Sigma_a^m = 0$. In the solution for Φ_s the source is taken as $Q_s = 1$; in the solution for Φ_{as} the source is $Q = x/a$. Calculations were performed for $\kappa^2 = 0$ (infinite lattice) and $-5 \leq n \leq 5$.

As may be seen from the figure the agreement with the exact diffusion solution is quite satisfactory even for such a relatively small number of terms in the expansion.

The labor involved in the proposed method is practically independent of the number of zones in the cell. The method may be applied to the calculation of two-dimensional cells with slugs of complicated shapes.

LITERATURE CITED

1. G. Ya. Rumyantsev, *Atomnaya Énergiya*, 13, 556 (1962).

A VERY SIMPLE MATHEMATICAL MODEL FOR STUDYING THE DYNAMICS OF SELF-REGULATING WATER-COOLED WATER-MODERATED REACTORS*

F. M. Mitenkov, B. I. Motorov, and É. A. Motorova

UDC 621.039.514

A mathematical model for investigating the stability of an isolated self-regulating reactor is formulated in the following way:

$$\frac{l}{\beta} \cdot \frac{d\Delta n}{dt} - \frac{n_0}{\beta} \Delta \rho + \Delta n - \frac{\lambda l}{\beta} \Delta c = 0;$$

* Translated from *Atomnaya Énergiya*, Vol.21, No.5, p.385, November, 1966. Original article submitted September 24, 1965; abstract submitted September 8, 1966.

$$\begin{aligned}
l \frac{d\Delta c}{dt} - \beta \Delta n + \lambda \Delta c &= 0; \\
\Delta \rho &= \alpha_\beta \Delta \theta + \alpha_{ICS} \Delta \theta_{ICS} + \alpha_r \Delta \theta_r; \\
m_r c_r \frac{d\Delta \theta_r}{dt} &= A_1 \Delta n - k_1 (\Delta \theta_r - \Delta \theta); \\
m_\beta c_\beta \frac{d\Delta \theta}{dt} &= k_1 (\Delta \theta_r - \Delta \theta) - 2G c_\beta \Delta \theta; \\
m_{ICS} c_{ICS} \frac{d\Delta \theta_{ICS}}{dt} &= A_2 \Delta n - 2G_{ICS} c_{ICS} \Delta \theta_{ICS}.
\end{aligned}$$

Here n is the relative neutron density in the reactor; ρ is the reactivity; β is the total fraction of delayed neutrons; c is the concentration of delayed neutron emitters for one effective group; l is the prompt neutron lifetime; λ is the decay constant for one effective group of delayed neutrons; α_r , α_β , and α_{ICS} are the average temperature coefficients of reactivity of the fuel and of the coolant in the reactor channels and in the interchannel space (ICS); k_1 is the heat transfer coefficient from fuel to coolant averaged over the length of a channel; $A_1 n$ and $A_2 n$ represent the power released in the channels and in the ICS respectively; G and G_{ICS} are the flow rates of the coolant in the channels and in the ICS; m_r , m_β , and m_{ICS} are the masses of the fuel and of the coolant in the channels and in the ICS; c_r , c_β , and c_{ICS} are the specific heats of the fuel and of the coolant in the channels and in the ICS; θ_r , θ , and θ_{ICS} are the mean temperatures of the fuel and of the coolant in the channels and in the ICS.

This model may be used to investigate reactor dynamics in the fairly high frequency region since the time constants characterizing heat transfer processes in the core are generally appreciably smaller than the circulation period of the coolant. The effects of the following factors were analyzed in establishing the mathematical model: the presence of the ICS, various numbers of delayed neutron groups, the prompt neutron lifetime, the distribution of parameters along a channel, the temperature coefficient of reactivity of the fuel, the non-linearity of the kinetic equations, the thermal inertia of the fuel element cladding.

A system described by a model which does not take account of the above factors is stable for any negative temperature coefficient of reactivity so long as either the fuel or coolant time constant is less than $1/\lambda$ which is almost always the case. Such a model is therefore crude even qualitatively because of its inadmissible underestimating of phase shifts in the feedback loop.

Taking account of the ICS in a stabilized system does not increase the phase shift in the loop. The same may be said of the number of delayed neutron groups on the basis of a comparison of the phase-frequency and amplitude - frequency characteristics of the kinetic equations.

Neglecting the prompt neutron lifetime is more serious; taking account of the time constant $1/\beta$ makes a significant change in the position of the boundary of the region of stability with respect to the temperature coefficient of reactivity.

If spatial variations of system parameters are taken into account, the description of heat transfer in the fuel and coolant requires partial differential equations and further analysis of transcendental transfer constants. In the frequency range investigated the phase shift transfer error of the discrete model both for a uniform and for a sinusoidal distribution of energy release along the length of a channel is insignificant.

A positive temperature coefficient of reactivity of the fuel appreciably increases the phase shift of the resultant negative feedback when negative feedback is controlling because of a larger phase lag than in the fuel.

Taking account of the thermal inertia of the fuel element cladding and the non-linearity of the kinetic equations for an amplitude of a sinusoidal perturbation of the reactivity of not more than 0.1β leads to an insignificant change of the phase shift in the system.

IMPROVED SYSTEM OF STATIONARY DOSIMETRIC
MONITORING AT THE VVR-M REACTORE. A. Konovalov, L.M. Ploshchanskii,
and V.A. Solov'ev

UDC 621.039.58

One of the principal drawbacks of the initial stationary dosimetric monitoring system serving the VVR-M reactor facility was the low sensitivity and low operational stability of the instruments monitoring radioactive gases and gamma radiation. The low-rated performance in radioactive gas measurements, malfunctioning of the steel sampling lines through buildup of corrosion products at weld sites and bends, the unreliability of 910000SP valves on stream due to design defects, and defects in the arrangement for monitoring off-gases were equally troublesome. Water-ring pumps were a source of constant dumping of large amounts of water contaminated to the level of 10^{-6} Ci/liter into the drainage system, when air was collected from the reactor process components.

The improved dosimetric monitoring system now being used in the VVR-M reactor of the A. F. Ioffe Physics and Engineering Institute (USSR Academy of Sciences) reactor goes a long way toward eliminating these drawbacks. The air monitoring system has a more developed branching network of sampling lines. All sampling lines are connected up to headers with shared reserve volume.

Manual, semiautomatic, and automatic monitoring options are available. In automatic monitoring, all points can be checked periodically in runs anywhere from 0.5 to 2 h. The devices sensing concentrations of radioactive gases are 50-liter chambers with three STS-6 counters placed inside the chamber. The sensitivity of the radioactive off-gas counters is 10 pulses per sec at $2 \cdot 10^{-9}$ Ci/liter for A^{41} . In addition to these counters, an ionization chamber positioned in the main header line can be used when required. Sampling air monitoring lines are made of coiled polyethylene tubing 20 by 4 mm. The sampling lines can be switched by electromagnetically actuated valves designed specially for this application. RGN-95 type gas blowers create a vacuum suction in the sampling lines.

Radioactive off-gases can be monitored by continuously pumping air from the ventilation center tubing through a DZ-20 ionization chamber. The chamber ionization current is measured directly on a EPPV-60 automatic recorder. The recorder scale is calibrated in Ci/h because of the constant gas flowrate in the ventilation center off-gas tube. The instrument has a sensitivity of 0.1 Ci/h.

Gamma radiation is monitored by means of two USIT-1 type devices. Kaktus type devices with DIG-1 ionization chambers are also used in hot caves, in the primary-loop pump house, and on the reactor cover.

Radiation hazard sound alarms and light-flashing alarms are actuated automatically for all types of radiation. Other situations actuating alarms are opening of reactor gate valves, opening of hot cave doors, opening of the primary-loop pump house entrance, etc.

The VVR-M improved dosimetric monitoring system meets the requirements set in existing public health rules and also meets technological standards. Operating experience acquired in two and a half years of work with the system will lead to further improvements.

Translated from Atomnaya Energiya, Vol.21, No.5, p.386, November, 1966. Original article submitted January 14, 1966; abstract submitted June 4, 1966.

CALCULATION OF THE ABSORPTION OF EPITHERMAL NEUTRONS
IN AN INFINITE LATTICE OF ABSORBING SLABS

V. N. Gurin

UDC 621.039.512.45

A method is proposed for calculating the absorption of epithermal neutrons in a cell with a central absorbing slab. The slab occupies the region $-t \leq x \leq 0$ and the moderator the region $0 \leq x \leq b$. The spatial and energy dependence of the neutron distribution in the cell is described by the solution of the age - diffusion equation

$$D\Delta\Phi(x, u) - \Sigma_a\Phi(x, u) = \frac{\partial q}{\partial u}, \quad (1)$$

where Φ is the neutron flux, q the slowing-down density, and u the lethargy.

It is supposed that there is a constant neutron source at lethargy u_0 :

$$\Phi(x, u_0) = C. \quad (2)$$

On the slab boundary $\Phi(x, u)$ satisfies the effective boundary condition

$$\left. \frac{\partial\Phi(x, u)}{\partial x} \right|_{x=0} = h(u)\Phi(0, u), \quad (3)$$

where $h(u)$ is the logarithmic derivative at the surface of the slab [1]. The condition at the cell boundary is written as

$$\left. \frac{\partial\Phi(x, u)}{\partial x} \right|_{x=b} = 0. \quad (3a)$$

An analytic solution of Eq. (1) is possible only if the logarithmic derivative h varies suitably with the lethargy u or the neutron age τ .

The solution of Eq. (1) is found by using the approximation to the logarithmic derivative h given in [2]:

$$\left. \begin{array}{l} \text{first region} \quad (0 \leq \tau \leq \tau') \\ h = \frac{h_0\tau_0}{\tau_0 + \tau' - \tau} \\ \text{second region} \quad (\tau' \leq \tau \leq \tau_T) \\ h = h_0 \end{array} \right\} \quad (4)$$

where τ_T is the lower limit of the epithermal group and τ_0 and h_0 are constants.

In this report the solution of Eqs. (1) - (4) is obtained by the use of Laplace transforms. An analytic solution $\Phi(x, \tau)$ exists only for the following discrete values of b , the half-width of the moderator

$$b = \frac{2\tau_0 h_0}{n-1}, \quad (5)$$

where $n = 1, 2, 3, \dots$

For $n = 1$, an infinite moderator, the solution agrees with the result obtained in [2]. The results for $n = 1, 2, 3, 4$ for slabs of boron carbide clad with aluminum and a graphite moderator are given in the form of curves showing the slowing-down density at the surface of a slab as a function of the neutron age τ .

The solution may be used to check the accuracy of various approximate methods including the application of the multi-group method to nonhydrogenous moderators.

LITERATURE CITED

1. E. I. Grishanin, *Atomnaya Énergiya*, **16**, 234 (1964).
2. H. Überall, *Nucl. Sci. and Engng.*, **7**, 228 (1960).

Translated from *Atomnaya Énergiya*, Vol. 21, No. 5, pp. 386-387, November, 1966. Original article submitted July 14, 1966.

LETTERS TO THE EDITOR

POSSIBILITIES OF THE PHOTONEUTRON METHOD FOR
DETERMINING HYDROGEN IN HEAVY METALS

N. P. Mazyukevich and V. A. Shkoda-Ul'yanov

UDC 543.843

New industrial techniques are calling for material with very small admixtures of certain impurities. In some cases the amount of hydrogen present must be controlled to $5 \cdot 10^{-6}\%$ [1].

Present methods of analyzing gaseous impurities are not sensitive enough [2, 3] and have inconvenient properties: They require small samples (weighing a few grams), involve preliminary treatment, take several hours, destroy the specimen, and so on.

To determine the mean concentration of gases in large metal ingots without destroying them, and to automate the process, rapid analysis methods are required.

Compact, relatively cheap high-current electron accelerators are now available, with beams ranging from tens of microamperes to tens of milliamperes [4, 5], and therefore it is of interest to make theoretical and experimental tests of the feasibility of the photoneutron method of determining the mean hydrogen content. This method is based on recording photoneutrons from the reaction $D(\gamma, n)H^1$ (threshold 2.23 MeV), which is caused by avalanche photons in the bulk of the specimen when it is irradiated by a gamma or electron beam of high intensity. The accuracy of hydrogen determinations will be affected by the presence of beryllium [threshold of (γ, n) reaction 1.67 MeV].

Using the avalanche theory of Belen'kii and Tamm, the present authors have calculated the photoneutron yields from hydrogen and beryllium, present to the extent of $10^{-4}\%$ in lead, in the energy range from the thresholds of the (γ, n) reaction to $E=6.71$ MeV (see annexed table). From the table it will be seen that at $E \approx 4.5$ MeV, where the contribution from the (γ, n) reaction involving the O^{17} isotope (threshold 4.14 MeV) is fairly small, the ratio Q_{Be}/Q_H is equal to 500, i.e., it is practically impossible to determine hydrogen against a background of beryllium when these isotopes are present in comparable concentrations. However, if the beryllium content is 2-3 orders of magnitude lower than the hydrogen content, the problem becomes easier to solve. According to Palei and Bezrogova [6] metallic uranium may contain $10^{-6}\%$ of beryllium, which makes it possible to detect 10^{-3} - $10^{-4}\%$ hydrogen in it by the photoneutron method. With this amount of beryllium, this conclusion is also valid for other heavy metals. Unfortunately, it is not always possible to estimate the sensitivity of the method for hydrogen in different metals, because there are practically no literature data on the beryllium contents of the metals.

Neutron Yields from Beryllium and Hydrogen

E, MeV	$Q_{Be} \cdot 10^{-9}$ neutrons/electron	$Q_H \cdot 10^{-12}$ neutrons/electron
1.67	—	—
2.24	0.01	—
2.80	0.04	0.003
3.35	0.07	0.08
3.91	0.12	0.20
4.48	0.17	0.35
5.03	0.24	0.54
5.59	0.31	0.76
6.15	0.38	0.97
6.71	0.46	1.2

If a specimen of lead contains $10^{-4}\%$ hydrogen and $10^{-6}\%$ beryllium, to achieve statistical accuracy in recording the photoneutrons (5%) we need 400 sec; if the beryllium is absent, only ~ 40 sec are required. This estimate was made by irradiating a specimen with a $50 \mu\text{A}$ electron beam with energy 4.5 MeV and beam efficiency 10%.

Other things being equal, any increase in the accelerator beam current will be accompanied by a proportional decrease in the analysis time, and may in principle render it possible to analyze production-line ingots on the conveyor.

Translated from *Atomnaya Energiya*, Vol. 21, No. 5, p.388, November, 1966. Original article submitted June 15, 1966.

LITERATURE CITED

1. C. Harrington and A. Ruehle, Uranium Production Technology, Van Nostrand, Princeton, N. J. (1959).
2. I.A. Berezin and V.I. Malyshev, Zh. Analit. Khimii, 17, 1101 (1962).
3. H. Waldron, Nucl. Sci. and Engng, 13, 366 (1962).
4. O.A. Val'dner, A.A. Glazhov, and A.I. Finogenov, Pribory i Tekhnika Éksperimenta, No. 3, 29 (1963).
5. G.I. Budker, Atomnaya Énergiya, 19, 497 (1965).
6. P.N. Palei and E.V. Bezrogova, Zh. Analit. Khimii, 16, 57 (1961).

CALCULATING PHOTOELECTRIC ATTENUATION
COEFFICIENTS FOR GAMMA RADIATION

O. S. Marenkov

UDC 539.121.7

The probability of an atomic photoelectric effect is known to vary markedly with ϵ , the gamma-quantum energy. The graph of this variation has been the object of several investigations, mostly theoretical; it rapidly falls off with rising energy in the range $\epsilon > \epsilon_K$, but at relativistic energies decreases approximately as ϵ^{-1} . The quantum theory of the photoeffect, though fairly clear in principle, leads to laborious calculations, in which the error in calculating the cross section of the photoeffect depends on the accuracy of the atomic wave functions being used. Although much theoretical work had been done on this question, we do not at present have any exact formulas for the cross section of the photoeffect in any energy range.

White-Grodstein [1] and McGinnies [2] survey the state of theoretical and experimental work on the subject up to 1959*, and give systematic coordinated data on the total and partial cross sections for the interaction of gamma radiation with matter at energies from 0.01 to 100 MeV: the error in the numerical values is below 3-5%.

However, the tabulated data in [1, 2] are in certain respects inconvenient for calculating the distribution of gamma fields in matter by the Monte Carlo method. In the present paper I give the results of an analytical approximation of the mass photoelectric attenuation coefficients for gamma rays in finite intervals of ϵ :

$$\frac{\tau}{\rho}(\epsilon) = c_0 + c_1\epsilon^{-1} + c_2\epsilon^{-2} + c_3\epsilon^{-3}.$$

* Later theoretical investigations of the photoeffect refer to the relativistic region; there are very few experimental papers on measurement of the cross section of the photoeffect.

Coefficients c_k for Calculating Mass Photoelectric Attenuation Coefficients for Gamma Rays

Element or substance	Energy range (MeV)	c_0	c_1	c_2	c_3
Beryllium	0.01-0.06	-0.00157	0.000205	-0.0000117	0.000000445
Carbon	0.01-0.15	-0.00115	0.000351	-0.0000366	0.00000217
Nitrogen	0.01-0.15	-0.00221	0.000657	-0.0000650	0.00000387
Oxygen	0.01-0.2	-0.00141	0.000602	-0.0000786	0.00000594
Sodium	0.01-0.3	-0.00126	0.000705	-0.000126	0.0000156
Magnesium	0.01-0.4	-0.000825	0.000679	-0.000155	0.0000219
Aluminum	0.02-0.4	-0.000125	0.000222	-0.0000952	0.0000246
Silicon	0.01-0.4	-0.000824	0.000767	-0.000195	0.0000354
Phosphorus	0.01-0.5	-0.000535	0.000513	-0.000156	0.0000405
Argon	0.02-0.6	-0.000225	0.000415	-0.000173	0.0000675
Calcium	0.03-0.8	-0.000658	0.000805	-0.000261	0.000105
Iron	0.02-1.0	-0.0000464	0.000285	-0.000122	0.0000211
Copper	0.02-1.0	0.000416	-0.000344	0.000137	0.0000274
Molybdenum	0.05-5.0	0.0000319	0.000711	0.000272	0.0000825
Tin	0.08-5.0	-0.0000865	0.00191	-0.0000386	0.00146
Lead	0.088-10.0	0.0000891	0.00644	0.00787	0.00429
Air	0.01-0.2	-0.00190	0.000634	-0.0000701	0.00000520
Water	0.01-0.2	-0.00109	0.000482	-0.0000652	0.00000518
Sand	0.01-0.4	-0.000277	0.000288	-0.0000852	0.0000183
Sodium iodide	0.06-6.0	0.0000219	0.00136	0.000790	0.00131

Translated from Atomnaya Energiya, Vol. 21 No 5, p. 389, November, 1966. Original article submitted July 14, 1966.

The coefficients c_k were calculated from the data in [1, 2] by the method of least squares, using weight functions which enabled the error of approximation to be shifted along the curve of $\tau/\rho(\epsilon)$. The annexed table gives numerical results for some elements and substances. The maximum error of approximation is below 5%, except for aluminum and sodium iodide, where it is 6.7 and 6%, respectively.

LITERATURE CITED

1. G. White-Grodstein, X-ray Attenuation Coefficients from 10 keV to 100 MeV. NBS, Circ., No. 583 (1957).
2. R. McGinnies, X-ray Attenuation Coefficients from 10 keV to 100 MeV. NBS, Suppl. to Circ., No. 583 (1959).

NEUTRON YIELD CURVE FOR A TRITIUM TARGET

L. N. Katsaurov and A. N. Kuznetsov

UDC 539.172.13

When zirconium-tritium or titanium-tritium targets are used to obtain neutrons, the yield of the D-T reaction systematically decreases; simultaneously, neutrons appear from the D-D reaction, and their yield gradually increases [1]. It has been shown experimentally that these changes depend markedly on the ion current incident on the target (Fig. 1)*. If we are working with deuteron beams with densities of $\sim 10\text{-}20 \mu\text{A}/\text{cm}^2$, we cannot explain the fall in neutron yield from the D-T reaction as being due to heating of the target [2, 3] or to knocking of tritium out of the surface by the incident ion beam.

The present authors also measured the thickness of the carbon film formed: they found that the observed fall in the yield of neutrons from the D-T reaction can be explained only as due to energy losses in this film. The same conclusion was arrived at by Butler and Jossett [4].

The behavior of solid tritium targets can be completely accounted for by a diffusion mechanism. The essence of this mechanism is as follows. The deuterium ions, falling on to the solid tritium target, are retarded, and, coming to rest in a layer about 0.1μ thick (for incident-particle energy $E_D = 200 \text{ keV}$, the scatter of the ranges is $\sim 15\text{-}20\%$ of the range in titanium [5]), they set up a concentration gradient, which causes diffusion of the hydrogen dissolved in the zirconium or titanium. When so much deuterium has accumulated that the particle concentration near the target surface exceeds the limiting concentration, equilibrium is attained, and hydrogen isotopes begin to separate out from the target: the amounts of tritium and deuterium formed are respectively proportional to the concentrations C_T and C_D . Consequently, the deuteron beam falling on the target also leads to continuous reduction of the target's tritium content.

For the equilibrium state we can obviously write

$$\frac{dN}{dS} = \beta \frac{dC}{dx}, \quad (1)$$

where dN/dS is the flux of particles (in this case, of deuterons), C is the concentration of the tritium-deuterium mixture, and β is the diffusion coefficient.

From (1) we easily find that

$$C = C_0 + \frac{a}{\beta S} (x_0 - x), \quad (2)$$

where C_0 is the initial concentration at which hydrogen atoms begin to separate out from the target surface, a is the number of deuterons incident per second on the target, x_0 is the depth of the layer in which the deuterons come to rest, x is a coordinate directed along the normal to the target surface, and S is the cross section of the beam of hydrogen atoms (in practice, this is equal to the cross-sectional area of the incident beam)†.

The second term on the right in (2) is very small in comparison with C_0 , and for a zirconium target ($C_0 \approx 10^{23} \text{ atoms}/\text{cm}^3$, $\beta \approx 10^{-5} \text{ cm}^2/\text{sec}$ [6], $a \approx 10^{12} \text{ ions}/\text{sec}$, $x_0 \approx 10^{-4} \text{ cm}$) it constitutes $\sim 10^{-10} C_0$. We can therefore neglect this term, and can assume that, after attainment of equilibrium in the target, C_0 , the concentration of hydrogen isotopes, also remains constant through the thickness of the target layer.

* The unit is taken as 10^{10} neutrons, and a milli-unit as 10^7 neutrons.

† There will be very little diffusion across the target surface, owing to the low concentration gradient in this direction and the small area over which diffusion can occur.

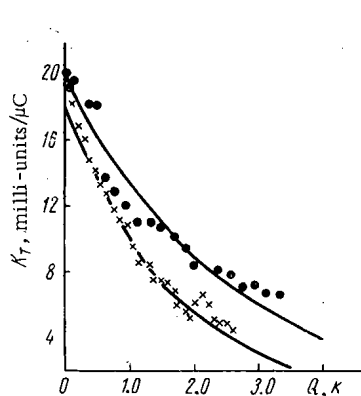


Fig. 1.

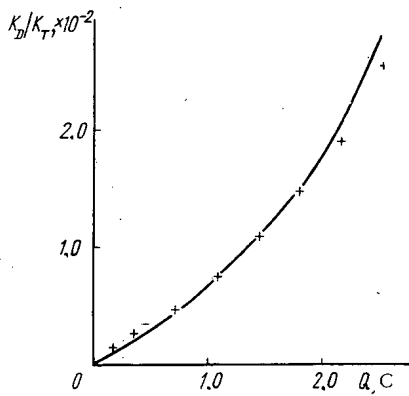


Fig. 2.

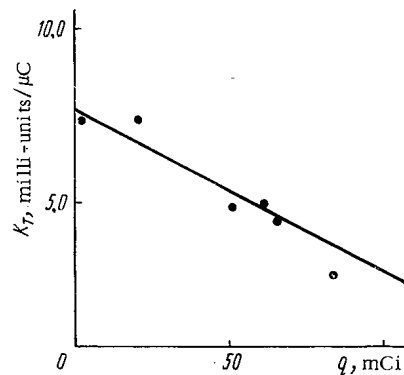


Fig. 3.

Fig. 1. Yield of neutrons from the D-T reaction with a zirconium-tritium target, plotted versus the total charge on the incident ions: ×) data from [1], $E_D = 250$ keV; ●) data of present authors, $E_D = 200$ keV.

Fig. 2. K_D/K_T versus the total charge on the ions falling on the target.

Fig. 3. Neutron yield from D-T reaction with zirconium-tritium target, versus amount of tritium separating from the target: ●) results of present authors.

The time for achievement of equilibrium is found from the expression

$$t_{eq} = 0.5 \frac{W^2}{\beta \bar{B}_M^2 d^2},$$

where W is the energy of the incident particles in keV, \bar{B}_M is the average retarding capacity of the target over the range in keV/mg/cm², and d is the relative density of the target. For a zirconium target, $t_{eq} = 9.5 \cdot 10^{-4}$ sec for energy $E_D = 200$ keV.

Thus we can assume that the tritium concentration C_T and the deuterium concentration C_D are the same at all times throughout the thickness of the target layer, and their sum is always equal to C_0 , while the area through which diffusion occurs is equal to the cross-sectional area of the incident beam.

From these considerations we can deduce that K_T , the yield of the D-T reaction, is equal to

$$K_T = K_{0,T} e^{-1.04 \cdot 10^{-2} \frac{A_H \bar{B}_M \nu}{\alpha_0 W S} Q}, \quad (3)$$

where A_H is the atomic weight of the target carrier, ν is the number of particles in one ion of the bombarding beam, α_0 is the number of target nuclei per atom of carrier, Q is the charge in coulombs carried to the target by the incident beam, S is the cross-sectional area of the beam in cm², and $K_{0,T}$ is the initial yield of the D-T reaction in the target. We also assumed that the rate of diffusion along the direction of the beam is much smaller than in the opposite direction [3]. As will be seen from Fig. 1, the experimental results agree fully with the results of calculations by means of (3).

From a large number of experimental measurements of K_T , on the assumption that the yield falls off exponentially, we obtained an exponent equal to $0.34Q$. On substituting the known values of A_H , \bar{B}_M , ν , α_0 , W , and S in (3), we found this index to be $0.38Q$ — in good agreement with the experimental results. The same value was found by Fleischer et al. [7].

By the condition $C_T + C_D = C_0$, we find an expression for the yield of the D-D reaction:

$$K_D = C_0 \left(1 - e^{-1.04 \cdot 10^{-2} \frac{A_H \bar{B}_M \nu}{\alpha_0 W S} Q} \right) \int_0^W \frac{\sigma_D}{B} dW, \quad (4)$$

where σ_D is the effective cross section of the D-D reaction, and B is the energy lost by the incident particles in the target layer ($B = dW/dx$). From (3) and (4) we find the ratio K_D/K_T :

$$\frac{K_D}{K_T} = \left(e^{-1.04 \cdot 10^{-2} \frac{A_H \bar{B}_M v}{\alpha_0 W S} Q} - 1 \right) \frac{\int_0^W \frac{\sigma_D}{B} dW}{\int_0^W \frac{\sigma_T}{B} dW}, \quad (5)$$

where σ_T is the effective cross section of the D-T reaction.

Figure 2 plots the experimental results cited from [1]. The solid curve was calculated from (5). The theoretical and experimental results will be seen to display good agreement.

At the same time, we measured the yield K_T of the D-T reaction and the amount of tritium separating out from the target, q (Fig. 3).

From the above considerations we find that

$$K_T = K_{0,T} \left(1 - \frac{3.7 \cdot 10^7}{\gamma x_0 C_0 S} q \right), \quad (6)$$

where γ is the decay constant of tritium, and q is expressed in millicuries.

Substituting for γ , x_0 , and C_0 , we get

$$K_T = K_{0,T} \left(1 - 6.72 \cdot 10^{-5} \frac{\bar{B}_M A_H}{W \alpha_0 S} q \right). \quad (7)$$

The solid line in Fig. 3 was calculated from (7) on the assumption that for a zirconium target $K_{0,T} = 20$ milli-units/ μC (1 milli-unit = 10^7 neutrons). Allowing for the difficulty of measuring the amount of tritium formed, we can consider that the experimental points agree with the theoretical curve.

Thus the diffusion mechanism for the yield curve of a tritium target is supported by the experimental results.

In conclusion, the authors would like to thank I. Ya. Barit and I. M. Frank for many discussions of the results, and also A.V. Elpidinskii and V.P. Pereygin for assistance with the experiments.

LITERATURE CITED

1. V. Heivens, In book, "Proceedings of International Conference on the Peaceful Use of Atomic Energy (Geneva, 1955)." Reports of foreign scientists. Vol. 4. Moscow, Izd. AN SSSR, p. 94 (1957).
2. F. Cambon and H. Reme, J. de physique, 25, 61 (1964).
3. K. Fiebiger, Z. angew. Phys., 8, 213 (1957).
4. J. Butler and C. Jossett, Phys. Rev., 108, 1473 (1957).
5. E. Segre, Experimental Nuclear Physics, Vol. 1, p. 209 (1955).
6. Smithells, Metals reference book. V. 2. London, p. 544 (1955).
7. A. Fleischer et al., IEEE Nucl. Sci., 12, 3, 262 (1965).

ANGULAR DISTRIBUTION OF FAST NEUTRONS EMERGING FROM A MEDIUM WHICH CONTAINS HYDROGEN

S. F. Degtyarev, V. I. Kukhtevich,
A. P. Suvorov, V. V. Tarasov,
V. K. Tikhonov, and S. G. Tsypin

UDC 539.125.5:539.121.72

Dulin et al. [1] studied the angular distribution of fast neutrons emerging from a 15 cm layer of water, for a point isotropic source, with initial energy $E = 3.5$ MeV, at the surface of a shielding barrier. The angular distribution of the dose rate was studied by Henry et al. [2] for fast neutrons emerging from a layer of polyethylene of thickness 7.5–38 cm, and by French [3] for fast neutrons emerging from a layer of lithium hydride of thickness 20 cm. The neutron sources used by these authors were 15 cm diameter collimated beams emerging from the BSR nuclear reactor.

The present article gives the results of experiments on the angular distribution of the flux (dose rate) of fast neutrons, with energies $E \geq 0.7$ MeV, emerging from a plate of lithium hydride with a density of 0.5 g/cm^3 and a thickness of 15, 30, 45, or 60 cm, or from a layer of water of thickness 15 or 45 cm.

The radiation source was a collimated beam of neutrons (plane unidirectional source). The experimental setup is shown in Fig. 1. Figure 2 shows the neutron spectrum of the source*, and also the spectrum of the BSR reactor [4].

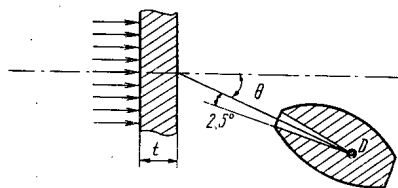


Fig. 1. Experimental setup.

As will be seen from Fig. 1, the neutron detector was placed within the collimating structure. In measuring the background count we used an additional stepped shield consisting of a mixture of paraffin and boron carbide, of total thickness 150 cm. This shield was placed directly inside the collimator channel. Measurements were made for angle $\theta \approx 0-55^\circ$. The neutrons were recorded by a scintillation fast-neutron detector consisting of a Plexiglas tablet with an admixture of ZnS (Ag), fastened to the end of an FEU-52 photomultiplier. The diameter of the tablet was 80 mm and its thickness 7 mm. Figure 3 gives the sensitivity curve†. Figure 4 gives the angular distributions of the flux (dose rate) of fast neutrons emerging from lithium hydride plates of various thickness. It will be seen that for $\theta \geq 10^\circ$ changes in plate thickness have little effect on the shape of the angular distribution. Between $\theta = 0$ and 10° the neutron flux curve has a marked peak due mainly to unscattered neutrons. The height and width of this peak decrease with increasing thickness of the lithium hydride plate: this is naturally due to increase in the fraction of scattered neutrons. It follows from Fig. 4 that the angular distribution of the flux of scattered neutrons is given approximately by the expression

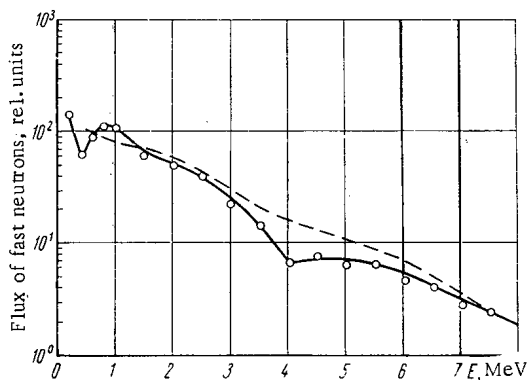


Fig. 2. Neutron spectra of BSR reactor (---) and of source (—).

* Data of L. A. Trykov.

† Data of S. F. Degtyarev, V. I. Kukhtevich, and V. V. Tarasov.

Translated from *Atomnaya Energiya*, Vol.21, No.5, pp.392-394, November, 1966. Original article submitted July 5, 1966.

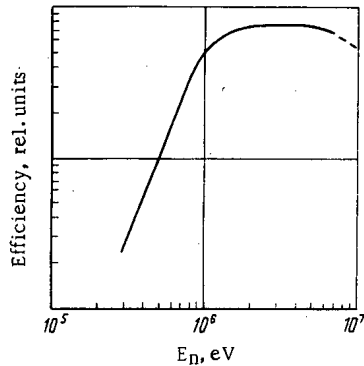


Fig. 3. Efficiency of ZnS (Ag) detector versus initial neutron energies.

$$\frac{d\Phi}{d\Omega}(\theta, t, E) = C(t, E) e^{-\theta/\theta_0(E)}, \quad (1)$$

where θ is the angle between the normal to the surface of specimen under test and the direction of the axis of the detector collimator t is the thickness of the shielding barrier, and θ_0 is a constant which, in the general case, depends on the neutron energy: for our incident neutron spectrum and for lithium hydride plates of all thicknesses, $\theta_0 = (28 \pm 2)^\circ$. The coefficient $C(E, t)$ can be found from the expression

$$\Phi_{sc} = (B-1) \Phi_{unsc} = \int_0^{2\pi} d\varphi \int_0^{\pi/2} C(E, t) e^{\theta/\theta_0} \sin \theta d\theta, \quad (2)$$

since the total flux of scattered radiation Φ_{sc} is equal to the build-up factor minus unity, multiplied by the flux of unscattered radiation Φ_{unsc} . Putting $\Phi_{unsc} = 1$, we get

$$\frac{d\Phi}{d\Omega}(E, t, \theta) = \frac{(B-1) \left(1 + \frac{1}{\theta_0^2}\right) e^{\theta/\theta_0}}{2\pi \left(1 - \frac{1}{\theta_0} e^{\pi/2\theta_0}\right)}. \quad (3)$$

For comparison, Fig. 4. gives the present authors' results and data from [3]. The comparison was made for a lithium hydride plate 30 cm thick with density 0.5 g/cm^3 . The results display satisfactory agreement: for $\theta = 15^\circ$ the maximum difference is $\sim 20\%$. Curve 1 in Fig. 4 was calculated by the Monte Carlo method for the angular distributions of fast neutrons from the BSR reactor, emerging from a lithium hydride plate 20 cm thick. Curve 2 illustrates the angular distribution calculated in the successive-scattering approximation. In this approximation it is assumed that on the detector, which is placed at

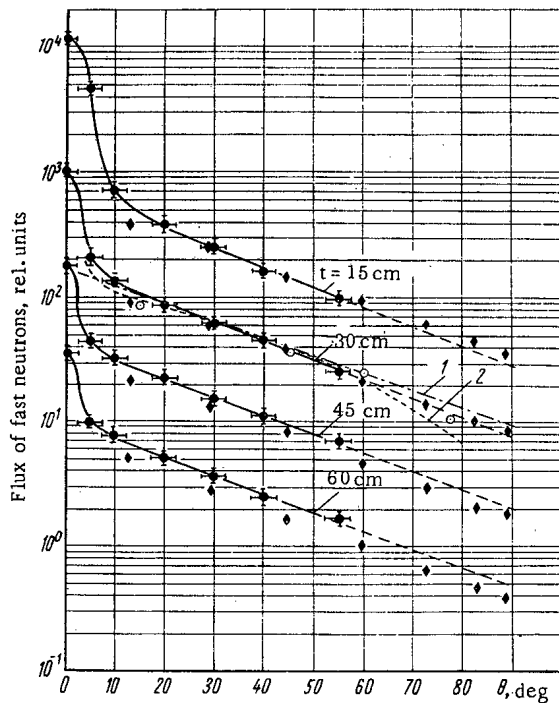


Fig. 4. Angular distributions of flux of fast neutrons emerging from lithium hydride ($\rho = 0.5 \text{ g/cm}^3$): \bullet) experimental results of present authors; \blacklozenge) calculated by the method of transmission matrices; \circ) experimental data of [3]; 1) calculated by the Monte Carlo method [3]; 2) calculated by the method of successive scattering [3].

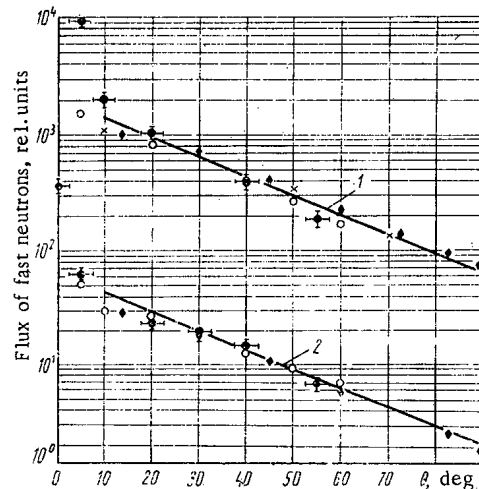


Fig. 5. Angular distributions of flux of fast neutrons emerging from water and other media containing hydrogen: 1, 2) data for shield thicknesses 15 and 45 cm of water, respectively; \bullet) experimental data (water); \blacklozenge) calculated by the transmission-matrix method (water); \circ) dose rate from polyethylene [2]; \times) dose rate for polyethylene (data of I. V. Goryachev et al.); —) experimental results of present authors for lithium hydride.

an angle θ to the normal, there are incident only those neutrons which are scattered through precisely this angle, i.e., no account is taken of neutrons which have undergone several collisions. Clearly, for large θ , when the contribution of multiply scattered neutrons is relatively large, the successive-scattering approximation will give a low value for the neutron flux; this is also apparent from Fig. 4. However, up to $\theta=60^\circ$ this approximation correctly represents the shape of the angular distribution of scattered neutrons (to within 10-15%). Unfortunately, no experimental or calculation errors are quoted in [3].

Figure 4 also gives results calculated by the multigroup transmission-matrix method ("R. O. Z." programme), as described in [5]. Calculations were made of the angular and energy distributions of a flux of neutrons from lithium hydride plates of various thicknesses for the cases of a plane unidirectional source with the spectrum shown in Fig. 2. For comparison with experiment, the results of the calculations multiplied by the detector efficiency. In the calculation it was assumed that, to reduce the γ background, 2.5 cm of lead was placed in front of the lithium hydride (or water) block.

Figure 5 shows the angular distributions of fluxes of fast neutrons with energy $E > 0.7$ MeV emerging from 15-cm and 45-cm layers of water, and also results calculated for water by the transmission-matrix method. The experimental and theoretical data were normalized for $\theta=30^\circ$ for 15 cm of water. As will be seen from the figure, the agreement between theory and experiment is fair. The same figure plots experimental results from [2], the angular distributions of the neutron dose rate for a barrier of polyethylene*, and also the present authors' experimental data for lithium hydride. On comparing the angular distributions of fast neutrons emerging from such hydrogen-containing media as lithium hydride, water, and polyethylene, we see that these distributions differ little, except at very large and very small angles. For example, in the case of lithium hydride and water, for $\theta \approx 20-60^\circ$ the difference between the shapes of the angular distributions is less than the experimental error (10-20%), while for values of θ greater than 60° or less than 20° , the fluxes of fast neutrons emerging from water are less than those for lithium hydride by a factor of 1.2-1.3 for corresponding angles.

LITERATURE CITED

1. V. A. Dulin et al., *Atomnaya Énergiya*, 17, 486 (1964).
2. R. Henty et al., *Transactions ANS*, 7, 40 (June 1964).
3. R. French, *Nuclear Sci. and Engng*, 23, 28 (1965).
4. R. French and J. Eggen, *Nucleonics*, 18, No. 3, 117 (1960).
5. T. A. Germogenova, A. P. Suvorov, and V. A. Utkin, In symposium "Topics in the Physics of Reactor Shielding", ed. by D. L. Broder et al., No. 2, Moscow, Atomizdat, p. 18 (1966).

* Data of I. V. Goryachev, V. I. Kukhtevich, and L. A. Trykov.

PASSAGE OF FAST NEUTRONS THROUGH THICK LAYERS OF LITHIUM HYDRIDE

G.M. Bozin, S.F. Degtyarev,
V.I. Kukhtevich, B.I. Sinitsyn, V.B. Staroverov,
V.K. Tikhonov, and S.G. Tsypin.

UDC 539.125.5:539.121.72

We have studied the attenuation of the flux (dose rate) of fast neutrons in lithium hydride of density 0.5 g/cm^3 .

We used a plane unidirectional neutron source, with the spectrum given in [1].

The shield under study was a block of lithium hydride, containing channels for the detector. During the measurements, the empty channels were filled with bungs of the same material. The cross sections of the shielding blocks were so chosen that a detector inside the shielding would be in the so-called infinite geometry.

To determine the build-up factor in lithium hydride, we measured the neutron attenuation in good geometry with careful collimation of the source and detector. For these measurements we used 5.5 cm diameter samples of lithium hydride.

The fast neutron flux was registered by a scintillation counter with a tablet of ZnS (Ag) mixed with Plexiglas (tablet diameter 4 cm, thickness 0.4 cm). The energy-sensitivity curve of this detector is

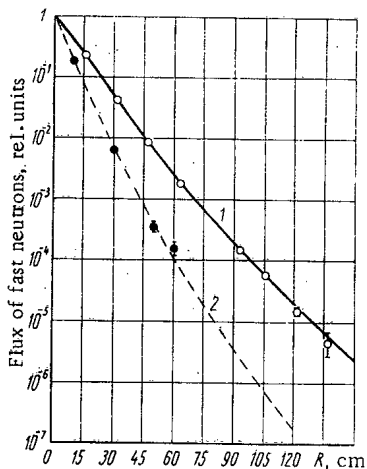


Fig. 1. Attenuation of neutrons with energies $E > 0.7$ MeV in lithium hydride, versus thickness R of shielding barrier, in poor (1) and good (2) geometries: O, ● experimental, —, - - - -) calculated.

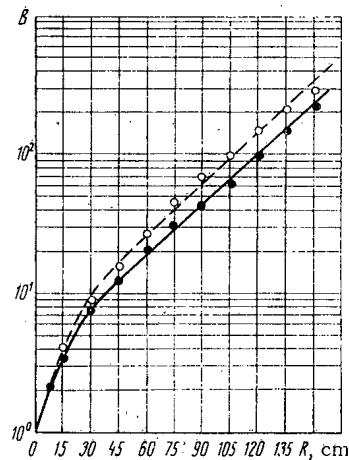


Fig. 2. Build-up factor B for fast neutrons with energies $E > 0.7$ MeV, versus thickness R of shielding barrier: O) build-up factor for neutrons with fission spectrum; ●) build-up factor for neutrons with spectrum given in [1].

Translated from *Atomnaya Énergiya*, Vol. 21, No. 5, pp.394-395, November, 1966. Original article submitted July 5, 1966.

given in [1]. To determine the effective energy threshold of the detector we used various neutron spectrums formed in hydrogen-containing media when the spectrum of the incident neutrons is close to the fission spectrum. Estimates made by a method suggested in [2] showed that the effective energy threshold of the ZnS (Ag) counter for lithium hydride is close to 0.7 MeV.

Figure 1 plots data on the attenuation of a flux of fast neutrons in poor (wide) and good (narrow) geometries in lithium hydride. This figure also shows the calculated results.

For narrow geometry, the calculation was performed for the total cross sections of lithium (Σ_t^{Li}) and hydrogen (Σ_t^{H}), allowing for the spectral distribution of the incident neutrons, $S(E)$, and the variation of detector efficiency $\varepsilon(E)$ with energy, by the formula

$$\Phi_{\text{narrow}}(R) = \int_0^{\infty} S(E) \varepsilon(E) e^{-(\Sigma_t^{\text{H}} + \Sigma_t^{\text{Li}})R} dE, \quad (1)$$

where R is the thickness of the lithium hydride shielding.

The attenuation of a flux of fast neutrons in lithium hydride for an incident spectrum $S(E)$ from a plane unidirectional source in wide geometry was calculated by a method which is described in [3]:

$$\Phi(R) = \int_0^{\infty} S(E) \varepsilon(E) e^{-\Sigma_t^{\text{H}}(E)R} [1 + \Sigma_t^{\text{H}}(E)R] e^{-k \Sigma_t^{\text{Li}}(E)R} dE, \quad (2)$$

where $k = 0.6$ is an empirical coefficient linking the extraction cross section with the total cross section for incident neutrons with continuous spectra.

There is good agreement between the calculated and experimental data for both types of geometry, up to attenuations of about six orders (for poor geometry).

Figure 2 plots the build-up factors of scattered neutrons with energies $E > 0.7$ MeV in lithium hydride, for the incident-neutron spectrum given in [1] and also for fission-spectrum neutrons. The experimental values of the build-up factor were obtained for lithium hydride thickness up to 60 cm ($\rho_{\text{LiH}} = 0.5 \text{ g/cm}^3$). In this range of thicknesses the errors were below 20%. For large thicknesses the build-up factor was determined less accurately, owing to the lack of experimental data on the neutrons in narrow geometry. It follows from (1) and (2) that the calculated build-up factors for $R > 150$ cm may have errors of more than 50% due to errors of only 2-3% in the values of the total cross sections.

It will be seen from Fig. 2 that the build-up factors vary little with the form of the spectra in lithium hydride, while they depend almost exponentially on the thickness.

Sinitsyn and Tsy-pin [3] have shown that (2) adequately expresses the attenuation of fast neutrons in hydrogen-containing media, such as water or polyethylene, for which the energy dependence of the extraction cross section is well known. It must be emphasized that the calculations were performed for neutrons with energies $E > 1.4$ MeV. In [3] the results of calculations using (2) are compared with the experimental data for neutrons with energies of 3 MeV in lithium hydride. Good agreement was found between the calculated and experimental data.

The present authors' experimental results showed that (2) can be used to calculate the attenuation of fluxes of neutrons with energies $E > 0.7$ MeV in lithium hydride and other hydrogen-containing media, up to attenuations of 10^6 .

LITERATURE CITED

1. S.F. Degtyarev et al., *Atomnaya Énergiya*, 21, 395 (1966)
2. B.I. Sinitsyn and S.G. Tsy-pin, In symposium "Topics in the Physics of Reactor Shielding", ed. by D.L. Broder et al., Moscow, Gosatomizdat, p.75 (1963).
3. B.I. Sinitsyn and S.G. Tsy-pin, *Bulletin of the Information Centre for Nuclear Data*, No.2. Moscow, Atomizdat, p.291 (1965).

BUILD-UP FACTOR OF FAST NEUTRONS VERSUS THE RELATIVE POSITIONS OF SHIELDING AND DETECTOR

S. F. Degtyarev, V. I. Kukhtevich,
V. K. Tikhonov, and S. G. Tsy-pin

UDC 539.125.52:539.121.72

The flux (dose rate) of monoenergetic neutrons at a distance R from a shield of thickness t (see Fig. 1) can be written as follows*:

$$\Phi(R, L, E_0) = \Phi_0 G(R, L) B(E_0, t, R, L) e^{-\Sigma_t(E_0)t} \quad (1)$$

where $G(R)$ is the geometrical attenuation factor, Φ_0 is the flux of neutrons before reaching the shielding, $B(E_0, t, R, L)$ is the build-up factor (of the flux or dose rate) of scattered radiation at a distance R from the outer end of the shielding barrier, and $\Sigma_t(E_0)$ is the total macroscopic cross section of interaction of neutrons with energy E_0 . Equation (1) can be written in terms of the relaxation length, which in this case also depends on the distance R :

$$\Phi(R, L, E_0) = \Phi_0 G(R, L) e^{-\frac{t}{\lambda(E_0, t, R, L)}} \quad (2)$$

Equation (1) can be generalized for any kind of neutron spectrum incident on a shielding barrier, for corresponding averaging of $\Sigma_t(E_0)$ and $B(E_0, t)$.

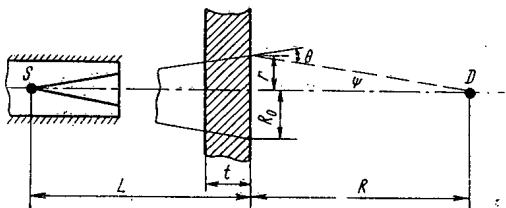


Fig. 1. Experimental setup.

The present article gives experimental results and calculations on the relation between the flux of fast neutrons (with energies $E > 0.7$ MeV) and the distance R , for constant source-shielding distance L (see Fig. 1). Figure 2 shows the spectrum of the source.

The shielding barriers were lithium hydride plates 45 and 60 cm thick, with density $\rho_{\text{LiH}} = 0.5 \text{ g/cm}^3$. The lateral cross sections of these plates were chosen so that a detector placed inside the shielding or at its surface would be in so-called "infinite" geometry.

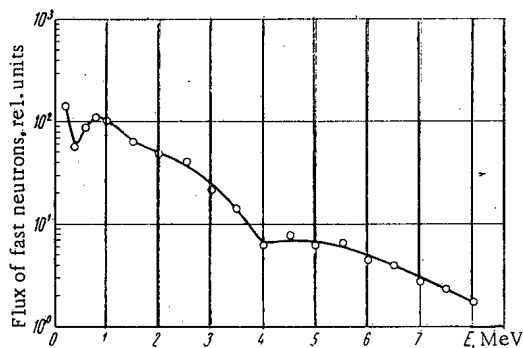


Fig. 2. Energy spectrum of neutrons from radiation sources.

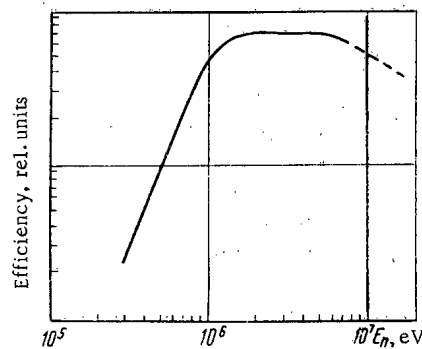


Fig. 3. Efficiency of ZnS (Ag) detector, versus initial neutron energy.

* An expression of this type (1) was used in [1, 2].

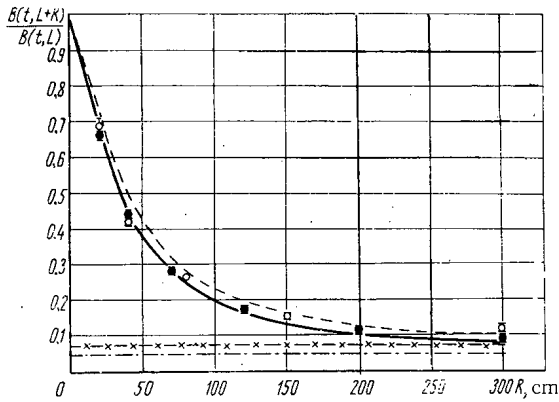


Fig. 4. Build-up factor versus shielding-detector distance R: ○) experimental shield thickness $t=45$ cm; ---) calculated, for $R_0=25$ cm, $t=45$; - ×-) experimental, $t=60$ cm; —) calculated for $R_0=25$ cm, $t=60$ cm; - - -) experimental (direct-radiation), $t=60$ cm.

where $B(t, L)$ and $B(t, L + R)$ are the build-up factors of scattered neutrons at the surface of the shielding barrier and at a distance R from it, respectively.

On the other hand, it can be shown that

$$\frac{B(t, L+R)}{B(t, L)} = \frac{1}{B(t, L)} + \frac{1}{B(t, L) \Phi_{\text{unsc}}(t, L+R)} \times \int_0^{2\pi} d\varphi \int_0^{\text{arctg} \frac{R_0}{R}} \frac{d\Phi}{d\Omega} \sin \psi d\psi, \quad (4)$$

since

$$\Phi_{\text{sc}} = \int_0^{2\pi} d\varphi \int_0^{\text{arctg} \frac{R_0}{R}} \frac{d\Phi}{d\Omega} \sin \psi d\psi$$

and

$$B(t, L+R) = 1 + \frac{\Phi_{\text{sc}}(t, L+R)}{\Phi_{\text{unsc}}(L+R, t)},$$

where Φ_{sc} and Φ_{unsc} are the fluxes of scattered and unscattered (direct) neutrons, respectively, R_0 is the radius of the neutron beam at the exterior surface of the shielding barrier, and $(d\Phi/d\Omega)(\theta)$ is the angular distribution of the flux of neutrons with energies $E \geq 0.7$ MeV emerging from the outer surface of the shielding barrier and going in direction θ , per unit solid angle (see Fig.1). Degtyarev et al. [4] have shown that the angular distribution of a flux of fast neutrons emerging from lithium hydride can be represented by the expression

$$\frac{d\Phi}{d\Omega}(\theta) = \frac{1 + \frac{1}{\theta_0^2}}{2\pi \left(1 - \frac{1}{\theta_0} e^{-\frac{\pi}{2\theta_0}}\right)} [B(t, L) - 1] e^{-\theta/\theta_0}, \quad (5)$$

where θ_0 is a constant for any given material. For a particular geometry (plane unidirectional source) and material, it was shown [4] that $\theta_0 = (28 \pm 2)^\circ$. Equation (5) was derived on the assumption that $B(t, L)$ is constant and that the angular distributions at all surfaces of the shielding turned towards the detector have the same form. The absolute values of $B(t, L)$ for lithium hydride (as a function of thickness t) were taken from [5].

When $R_0 \ll L$ (as was the case in our own experiment: $R_0 = 0.25$ m, $L = 6.7$ or 6.9 m), (4) can be rewritten with the aid of (5) as [1]

* Data of S.F. Degtyarev, V.I. Kukhtevich, and V.V. Tarasov

The neutron fluxes were recorded by means of a fast-neutron scintillation counter with a tablet of Plexiglas and ZnS(Ag) (diameter 8 cm, thickness 0.7 cm). Figure 3 gives the relation* between the detector efficiency and the neutron energy. The effective energy threshold of the detector was determined by the method described in [3]. Here we used neutron spectra formed by hydrogen-containing media when the incident-neutron spectrum was close to the fission spectrum. The effective energy threshold of the detector was estimated to be close to 0.7 MeV for lithium hydride.

During the experiment we made direct measurements of the fast-neutron flux at the surface of the shielding barrier, $\Phi(t, L)$, and the flux at distance R from the barrier, $\Phi(t, L + R)$. The background was measured by suppressing the primary effect by means of additional shielding. By (1) we have

$$\frac{B(t, L+R)}{B(t, L)} = \frac{\Phi(t, L+R)}{\Phi(t, L)} \cdot \left(\frac{L+R}{L}\right)^2, \quad (3)$$

$$\frac{B(t, R+L)}{B(t, L)} = \frac{1}{B(t, L)} + \frac{[B(t, L)-1]}{B(t, L)} \times \frac{\left[1 - \exp\left(-\frac{1}{\theta_0} \operatorname{arctg} \frac{R_0}{R} \cdot \frac{R_0/(R\theta_0+1)}{\sqrt{1+(R_0/R)^2}}\right) \right]}{\left(1 - \frac{1}{\theta_0} e^{-\pi/2\theta_0}\right)} \times \left(1 + \frac{R}{L}\right)^2. \quad (6)$$

If $R_0/R \leq 0.2$ and $R_0/L \leq 0.3$, (6) takes the form

$$\frac{B(t, L+R)}{B(t, L)} = \frac{1}{B(t, L)} + \frac{B(t, L)-1}{B(t, L)} K [1 - e^{-Z(1+Z)}], \quad (7)$$

where

$$K = \frac{1 + \theta_0^2}{e^{-\pi/2\theta_0} - \theta_0}; \quad Z = \frac{R_0}{R\theta_0} \left(1 + \frac{R}{L}\right).$$

Figure 4 gives curves for the build-up factors of fast neutrons with energies $E \geq 0.7$ MeV in front of shielding barriers made of lithium hydride of thickness 40 or 60 cm ($\rho_{\text{LiH}} = 0.5 \text{ g/cm}^3$), plotted versus the distance R from the outer surface of the shielding. The experimental results are plotted in the form of (3), while the calculated data were obtained from (6) and (7). Figure 4 shows that there is good agreement between the experimental and theoretical values of $[B(t, L+R)]/[B(t, L)]$. From the curves in Fig. 4 we can conclude that as the distance from the shielding increases, the proportion of scattered radiation in the total neutron flux decreases (and that of unscattered radiation increases). For example, immediately outside a lithium hydride shield of thickness 60 cm, $\Phi_{\text{sc}}/\Phi_{\text{unsc}} \approx 0.05$, while at about 3 m distance $\Phi_{\text{sc}}/\Phi_{\text{unsc}} \approx 0.5$, i.e., the scattered and unscattered radiations are equal. Clearly, at greater distances this ratio will be still higher.

Motteff and Osgood [6] showed that, for a neutron beam with 1 m^2 cross section and shielding consisting mainly of lithium hydride, the attenuation of the radiation by the shielding increases with increasing R (as found by the present authors). For example, when $L + R = 2.7 \text{ m}$, the attenuation increases by a factor of 3.7, while at 15 m the factor is 9.5*.

LITERATURE CITED

1. Yu. A. Kazanskii, V.I. Kukhtevich, and S.G. Tsy-pin, Information Bulletin of the Center for Nuclear Data, No.2. Moscow, Atomizdat, p.305 (1965).
2. Yu. A. Kazanskii et al., Atomnaya Energiya, 21, 424 (1966).
3. B.I. Sinitsyn and S.G. Tsy-pin, Topics in the Physics of Reactor Shielding, ed. by D.L. Broder et al. Moscow, Atomizdat, p.75 (1963).
4. S.F. Degytarev et al., Atomnaya Energiya, 21, 392 (1966).
5. G.M. Bozin et al., Atomnaya Energiya, 21, 394 (1966).
6. J. Motteff and H. Osgood, Trans. Amer. Nucl. Soc., 5, 403 (1962).

* This is the true attenuation by the shielding material; that due to the distance R is eliminated by multiplying by $[(L+R)/R]^2$.

PASSAGE OF GAMMA RAYS THROUGH SPHERICAL AND
CYLINDRICAL SHIELDING BARRIERS

A.V. Larichev, O.F. Partolin,
E.D. Chistov, and O.M. Zараev

UDC 621.039.58

The attenuation of gamma radiation during passage through shielding is known to depend on the shape of the shield. For example, the attenuation imposed by a cylindrical lead shield is much greater than that imposed by plane-barrier shielding of the same thickness on gamma rays from Co^{60} , Cs^{137} or Au^{198} sources [1]. Umeda and Hyodo [2] have shown that the dose build-up factor for gamma rays from linear Co^{60} or Cs^{137} sources passing through the walls of steel tubes is less than for passage through flat barrier shields. A similar effect was observed by Osanov [3] for a distributed cylindrical Co^{60} source. The present authors have found [4] that the attenuation of gamma rays from point sources due to cylindrical tungsten, lead or iron shields is greater than that due to flat barrier shields. Umeda [5] used the Monte Carlo method to calculate the numerical and energy spectra associated with the passage of gamma rays from point isotropic Co^{60} and Cs^{137} sources through lead and iron shields. It was shown that the current build-up factors for gamma rays in spherical barriers are less than those in cylindrical barriers.

The present letter gives the results of experiments on the attenuation of gamma rays from Co^{60} , Cs^{134} , and Tm^{170} in cylindrical and spherical shielding barriers. The isotope activities were 0.5-5 g-equ Ra. The measurements were made with a DIM-60 standard roentgenometer— at energies of 0.06-1.5 MeV the error of this instrument was $\pm 7\%$ (the ionization chamber volumes were 5 and 800 cm^3) — and an MRM-1 microroentgenometer with a special ionization chamber of volume 1000 cm^3 , for which the energy dependence was below 10% for energies from 0.06 to 1.5 MeV.

The source-detector distance was 50 or 100 cm. At these distances the gamma rays could be taken as coming from point sources. The spherical and cylindrical barriers were sets of hollow hemispheres and hemicylinders of various thicknesses which were fitted into one another. The shielding thickness increased towards the detector. The spherical screens of lead, iron and aluminum had maximum thicknesses of 75 mm, while those of VNM-2-3 tungsten alloy had maximum thicknesses of 41 mm (converted to density 19.3 g/cm^3). The cylindrical barriers of lead, iron and aluminum had maximum thicknesses of 100 mm.

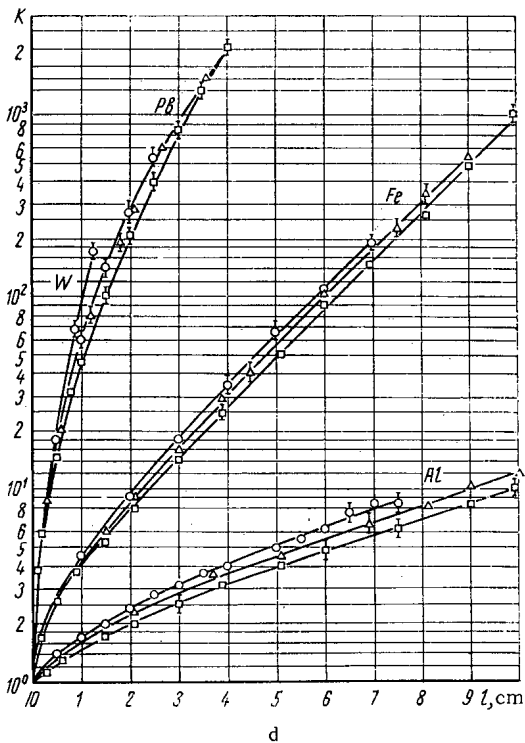
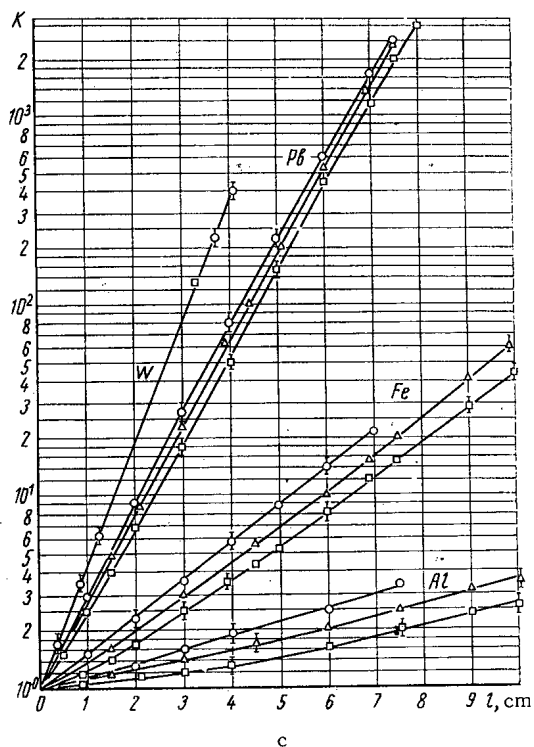
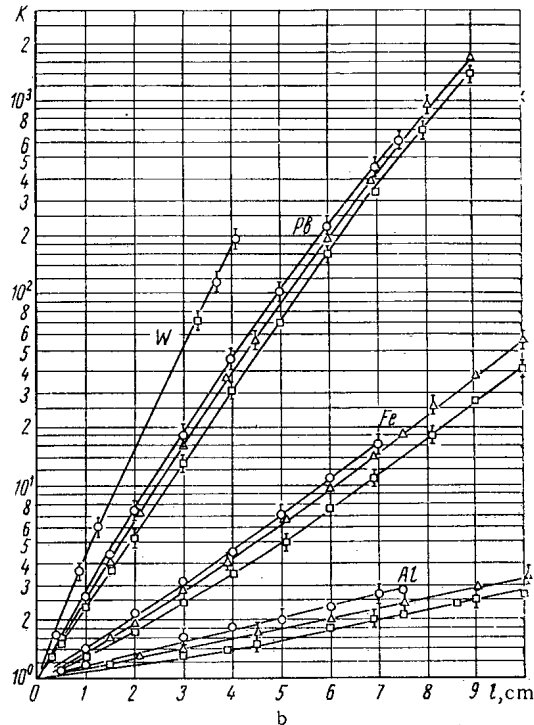
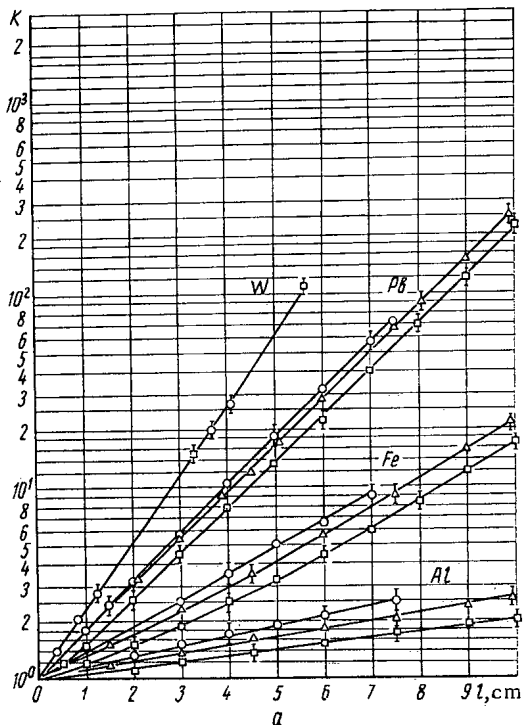
Similar measurements were made in the same conditions for flat barrier shields which consisted of lead, iron, and aluminum sheets up to 100 mm thick and blocks of tungsten alloy. During all the measurements the source was placed at the center of the shielding screen. For each shielding thickness, five to eight detector readings were taken. The attenuation factor for gamma rays was calculated from the formula

$$K = \frac{P_0}{P_x} \quad (1)$$

where P_0 is the detector reading without the shielding and P_x is the detector reading with shielding of thickness x .

The figure plots the dose rate attenuation factor for gamma rays from Co^{60} , Cs^{134} , Cs^{137} , and Tm^{170} versus the thicknesses of spherical, cylindrical and plane-barrier shields of various materials. The results obtained for various source-detector distances agreed to within the experimental error (maximum error 10%). For the same shield thickness, the attenuation of gamma rays by a cylindrical shield is characteristically greater than that by a plane-barrier shield, and less than that due to a spherical shield. The results for plane-barrier shields agree, to within the experimental error, with the results in [6-8], while those for cylindrical lead shields and Co^{60} radiation agree with the data in [1].

Translated from *Atomnaya Energiya*, Vol. 21, No. 5, pp.398-400, November, 1966. Original article submitted June 23, 1966.



Attenuation factor K for gamma rays from Co^{60} (a), Cs^{134} (b), Cs^{137} (c), and Tm^{170} (d), versus shielding thickness l : \circ) spherical; Δ) cylindrical; \square) flat barrier

The relative deviations, δ_1 and δ_2 respectively, of the attenuation factors for spherical and cylindrical screens from the factors for the same thicknesses of plane-barrier shields, in units μx , for sources of monoenergetic radiation, were calculated from the formula

$$\delta_{1(2)} = (K_{\text{sph(cyl)}} - K_{\text{pl}}) / K_{\text{pl}}. \quad (2)$$

Both δ_1 and δ_2 increase with decreasing gamma-ray energy and with decreasing atomic number of the shielding material. For example, for gamma rays from Co^{60} , with shield thickness $\mu x = 3$, $\delta_1 = 30\%$ and $\delta_2 = 20\%$ for lead, while $\delta_1 = 50\%$ and $\delta_2 = 30\%$ for iron. For Cs^{137} , for the same shield thickness δ_1 and δ_2 are 50 and 30% for lead and 70 and 40% for iron.

Similar behavior of the attenuation of gamma rays by variously-shaped shields is observed for isotopes with complex radiation energy spectra (Cs^{134} , Tm^{170}). We should, however, mention that for radiation from such isotopes as Tm^{170} and Se^{75} the shape of a lead shield has an appreciable influence on the attenuation factor only for shields of low thickness (2-3 cm). For lighter shielding materials, the shape of the barrier affects the gamma attenuation factor for thick shields also.

To get a theoretical explanation of the observed differences in attenuation factors between differently-shaped shields, we carried out a calculation in the single-scattering approximation. We found that the observed effect is caused by the different contributions made by the scattered radiation to the dose rate at the detector site for differently-shaped shields, since the contribution made by unscattered radiation is independent of the shape of the shield, other things being equal. The single-scattering approximation is valid for scatterers with sizes of order $1\mu x$ [9]. We carried out calculations for lead, iron and aluminum shields of thickness $\mu x = 1$ for gamma-ray energies of 1.25 and 0.661 MeV and source-detector distances of 50 and 100 cm. For example, with iron shielding and 1.25 MeV gamma rays, for $R = 50$ cm the contribution made to the dose rate at the point of detection by radiation scattered once in a spherical lead shield was found to be 30% less than the analogous contribution for a plane-barrier shield.

The above experimental data on attenuation of gamma rays from certain isotopes by spherical and cylindrical shields can also be used in the design of various types of shielding (protective casings for gamma-ray equipment, containers, etc.).

In conclusion, the authors would like to thank N.G. Gusev for valuable advice on the interpretation of our results, and A.G. Shcheglov for assistance with the experiments.

LITERATURE CITED

1. Z.S. Aref'eva et al., *Atomnaya Énergiya*, 11, 186 (1961).
2. J. Umeda and T. Hyōdo, *Nucl. Structural Engng*, 2, 335 (1965).
3. D.P. Osanov, *Atomnaya Énergiya*, 15, 331 (1963).
4. S.S. Gurvits et al., In symposium "Scientific Work of the Institute of Labor Protection of the All-Union Central Council of Trade Unions (VTsSPS)", No.3 (23). Moscow, Profizdat, p. 51 (1963).
5. J. Umeda, *J. Nucl. Sci. and Technol.*, 1, 87 (1964).
6. N.G. Gusev and E.E. Kovalev, *Nomograms for Design Calculations on Shielding against Gamma Rays from Ra^{226} , Co^{60} , Cs^{137} , and Ir^{192}* , Moscow Atomizdat, (1959).
7. L.M. Mikhailov and Z.S. Aref'eva, *Tables and Nomograms for Designing Gamma-ray Shielding*, Moscow, "Meditsina," (1965).
8. R. Beigno and M. Laughead, *Radiology*, 76, 281 (1961).
9. *Reactor Shielding Design Manual*, Ed. by T. Rockwell, Van Nostrand, Princeton, N.J. (1956).

YIELDS OF NUCLEAR REACTIONS FOR MAKING Na^{22}
IN A CYCLOTRON

N.N. Krasnov and P.P. Dmitriev

UDC 539.172.817

Na^{22} ($T_{1/2} = 2.62$ years) is the only long-lived isotope of sodium. Some data on the cross sections and yields of reactions which lead to its formation are given in [1-13]. However, as will be seen from the accompanying table, these data are contradictory and incomplete.

Working with the $1\frac{1}{2}$ -meter cyclotron of the FEI [14], the present authors measured the yield curves of Na^{22} for the two most efficient methods of obtaining sodium without a carrier. The Na^{22} yields were determined by recording gamma rays with energy 1280 keV. The accuracy of the yield determinations was $\pm 15\%$. The proton and deuteron energies were varied by means of filters. The details of the method were described in [15]. The results are shown in the accompanying figure. The table gives the principal data for four methods of obtaining Na^{22} . It will be seen from the table and figure that the most efficient method of obtaining Na^{22} is irradiation of magnesium by deuterons.

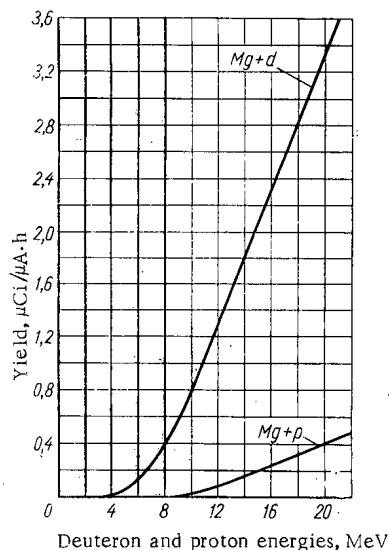
Principal Data on Methods of Obtaining Na^{22}

Method of making Na^{22}	Formation reaction	Energy threshold of reaction (MeV)	Content of initial isotope in natural mixture, %	Published data on yields of Na^{22}		
				Particle energy, MeV	Yield, $\mu\text{Ci}/\mu\text{A}\cdot\text{h}$	Source
$\text{Mg} + d$	$\text{Mg}^{24}(d, \alpha)$ $\text{Mg}^{25}(d, \alpha n)$	— 5.8	78.6 10.1	20	3.3	*
				10.6	0.87	[8]
				14	1	[1]
				14	1.78	[6]
				14	3.1	[7]
				14	2.1 †	[7]
				15	1.5	[4]
				15	2	[3]
				20	2.5	[9]
				25	3.2	[5]
30	2	[2]				
$\text{Mg} + p$	$\text{Mg}^{25}(p, \alpha)$ $\text{Mg}^{26}(p, \alpha n)$	3.2 14.8	10.1 11.3	22	0.5	*
				20.8	0.64	[12]
				22	0.4	[10]
				22	0.51	[13]
$\text{Na} + p$	$\text{Na}^{23}(p, pn)$ $\text{Na}^{23}(p, 2n)$	12.9 19	100 100	22	3.1	[10]
$\text{Na} + d$	$\text{Na}^{23}(d, t)$	3.4	100	15	0.11	[11]
				25	0.43	[5]

* Data from present article.

† Value derived by present authors from excitation function measured by Vlasov et al. [7].

Translated from *Atomnaya Energiya*, Vol. 21, No.5, pp. 400-401, November, 1966. Original article submitted June 18, 1966.



Yield of Na^{22} , plotted versus energies of deuterons and protons for thick magnesium target.

LITERATURE CITED

1. W. Garrison and J. Hamilton, *Chem. Revs.*, **49**, 237 (1951).
2. A. Aten and J. Halberstadt, *Philips Techn. Rev.*, **16**, No.1 (1954).
3. J. Cruverman and P. Kruger, *Internat. J. Appl. Rad. and Isotopes*, **5**, 21 (1959).
4. K. Chackett et al., *Nucl. Instrum. and Methods*, **14**, 215 (1961).
5. H. Moeken, *Production of Radioisotopes with Charged Particles*, Dissertation, Amsterdam, (1957).
6. J. Irvine and E. Clarke, *J. Chem. Phys.*, **16**, 656 (1948).
7. N.A. Vlasov et al., *Atomnaya Énergiya*, **2**, 169 (1957).
8. P.P. Dmitriev et al., In book "Proceedings of Conference on the Preparation and Use of Isotopes" (Moscow, 1957). Moscow, Izd. AN SSSR, p. 28 (1957).
9. M.Z. Maksimov, *Ibid.*, p. 31.
10. J. Martin et al., *Nucleonics*, **13**, No.3, 28 (1955).
11. Z. Bowen and J. Irvine, *Phys. Rev.*, **127**, 1698 (1962).
12. G. Glason et al., *Intern. J. Appl. Rad. and Isotopes* **13**, 223 (1962).
13. B. Cohen et al., *Phys. Rev.*, **96**, 1617 (1954).
14. N. N. Krasnov et al., *Pribory i Tekhnika Éksperimenta*, No. 4, 22 (1965).
15. N. N. Krasnov and P. P. Dmitriev, *Atomnaya Énergiya*, **20**, 57, 154 (1966).

EFFECT OF ACCELERATING VOLTAGE ON INTENSITY IN THE DUBNA SYNCHROCYCLOTRON

V. I. Danilov, I. B. Enchevich,
É. A. Polferov, and A. N. Safonov

UDC 621.384.611

Recent studies seeking ways of improving the efficiency of synchrocyclotrons [1-4] have been encouraged primarily by the reliability and stability in operation which these machines have demonstrated.

The pattern of variation in intensity as the accelerating voltage U_g and the modulation frequency F_M are increased proportionately is of interest here. Since $\cos \varphi_S$ does not vary with the orbit radius in this case, the intensity will be determined, in the absence of phase losses, by bunching conditions of the accelerated ions during the capture time. We can assume that the principal losses occur near the center through breakdown of vertical stability, since the focusing forces (forces due to the fall-off of the magnetic field, the bias across the dee etc.) are weaker than the space-charge defocusing forces of the ion bunch in that region. We should also note that particle losses due to scattering in the gas occur near the ion source [5]. If $\cos \varphi_S$ increases radially, then phase losses are also possible. In that case it will be better to study the intensity variation with acceleration voltage at small radii, since the difference in the decay of phase oscillations owing to the dependence of the number of those oscillations on U_g might severely distort the variation pattern.

MacKenzie [6] and Lawson [7] have attempted to theoretically find a relationship between the accelerated ion current and the voltage across the dee by taking space charge forces into account. MacKenzie made a few simplifying assumptions on the particle distribution in the beam and on the nature

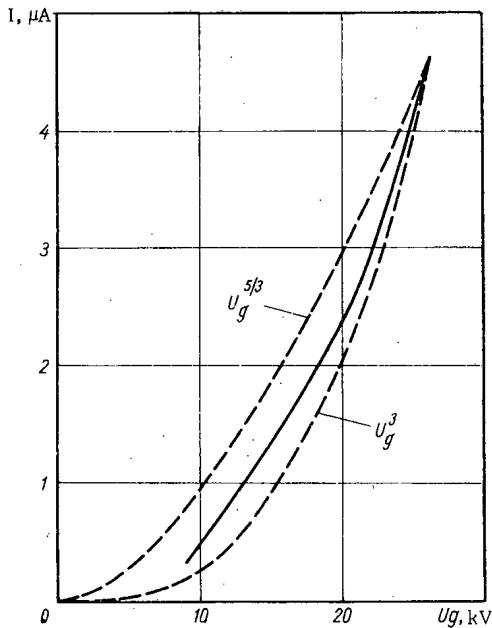


Fig. 1. Accelerating voltage dependence of the proton current at radius 90 cm.

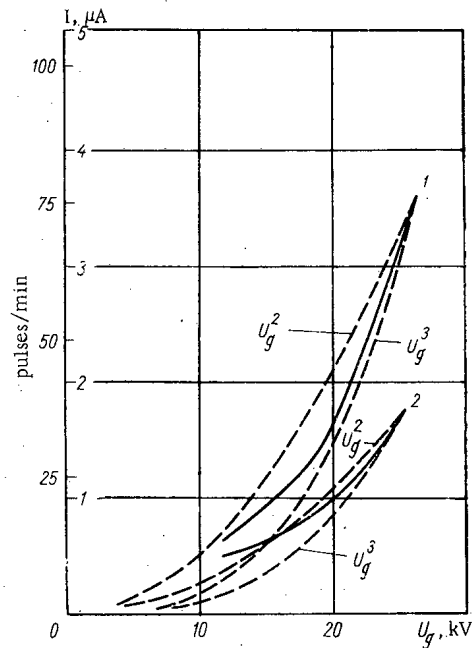


Fig. 2. Accelerating voltage dependence of proton beam intensity at finite radius. 1) $U_f = -11$ kV; 2) $U_f = 0$.

Translated from *Atomnaya Énergiya*, Vol. 21, No. 5, pp. 402-403, November, 1966. Original article submitted May 17, 1966.

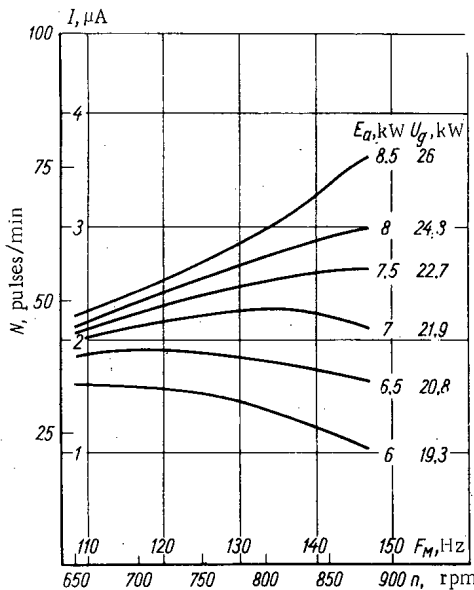


Fig. 3. Variation of proton beam intensity at finite radius with modulation frequency for several oscillator anode voltages.

The diagram also shows two curves, one a cubic parabola, the other plotted for $U_g^{5/3}$. These curves are fitted on the end-point of the experimental curve for comparison. Clearly, the proton current rises with the accelerating voltage at a slower rate than U_g^3 , but yet at a faster rate than $U_g^{5/3}$.

The relationship between intensity and accelerating voltage was also measured at the finite radius $r_k = 274.5 \text{ cm}$ by recording neutrons generated on a beryllium target. The increase in intensity at a finite radius as the accelerating voltage U_g was stepped up in the presence (1) and absence (2) of electrostatic focusing can be seen in Fig. 2, where the number of pulses recorded by a neutron monitor is plotted as ordinate, as is the current at the finite radius. The relationship between the beam current and the neutron monitor readings was found by using beam current data under operating conditions, reported elsewhere [4]. For comparison, the diagram also shows curves $I \sim U_g^2$ and $I \sim U_g^3$ fitted to the experimental curves at the end points. Clearly, the experimental intensity dependences are close to $I \sim U_g^{5/2}$ over a finite region. Extrapolation of the experimental curves to the voltage $U_g \sim 30 \text{ kV}$ yields a current $5.3 \mu\text{A}$ at $U_f = -\text{kV}$, and $2.75 \mu\text{A}$ at $U_f = 0$. The rpm of the buncher n , must then rise to 1000-1200 ($F_M \sim 200 \text{ Hz}$).

Variation of intensity with n from 650 to 880 rpm ($F_M = 108$ to 146 Hz) and at constant anode voltage $E_a = 6$ to 8.5 kV when $U_f = -11 \text{ kV}$ was ascertained to secure information on a possible increase in the beam current of the Dubna synchrocyclotron by stepping up the oscillator anode voltage and raising the modulation frequency. The Dubna synchrocyclotron is usually operated at $E_a = 7.2 \text{ kV}$ and $n = 680 \text{ rpm}$ ($F_M = 113 \text{ Hz}$). As the diagram shows, intensity increases 25% when the E_a is raised to 7.5 kV and n is raised to 860-880 rpm. We then have $I = 2.6\text{-}2.7 \mu\text{A}$; $U_g \sim 22.6 \text{ kV}$; $F_M = 125 \text{ Hz}$.

Increasing the accelerating voltage U_g to 26 kV (corresponding to $E_a = 8.5 \text{ kV}$) and n to 880 rpm leads, as is clear from Figs. 2 and 3, to a rise in intensity 1.65 times above the existing level ($I = 3.5 \mu\text{A}$).

Analysis of the experiments shows that the beam current in the Dubna synchrocyclotron can be brought up to $10 \mu\text{A}$, when the accelerating voltage is raised to 40 kV and the F_M correspondingly to about 300 Hz , if the pattern of variation $I \sim U_g^{5/2}$ is retained as the intensity increases. Note that optimum beam shaping in the accelerator center region will yield even higher current.

The authors conclude by thanking Yu. M. Kazarinov and Yu. N. Simonov for their kind assistance in neutron monitor measurements of the beam intensity.

of the coulomb forces, neglected dependence of the ion energy increment on the orbit radius, and found that the beam current varies with the accelerating voltage as U_g^3 . His assumption here is that the magnetic focusing forces begin to act in steps starting with a certain radius r_m . Lawson considered the effect of magnetic forces from the accelerator dead center, assuming a quadratic law of fall-off of the magnetic field, and found the beam current to be proportional to $U_g^{5/3}$.

A series of experiments designed to find the relationship between the current of accelerated particles and the dee voltage was arranged to verify these theoretically derived dependences and to shed some light on a possible further rise in the intensity of the Dubna synchrocyclotron.

Since we still experience certain difficulties in attempting to measure the accelerating voltage in a synchrocyclotron, the method advanced by Safonov [8] was employed.

The relationship between beam current and accelerating voltage U_g was determined at two different radii, and $F_M/U_g = \text{const}$. The intensity was measured with a current probe at $r = 90 \text{ cm}$ while the accelerating voltage was varied from 11 to 26 kV with a corresponding variation in modulation frequency. Figure 1 shows $I = I(U_g)$ for $F_M/U_g = \text{const}$ and with a constant voltage across the focusing electrodes, $U_f = -\text{kV}$ [3]. The dia-

LITERATURE CITED

1. Conference on High Energy Cyclotron Improvement, College of William and Mary, Williamsburg, Va., USA, (1964).
2. V.I. Danilov et al., Dubna Joint Institute for Nuclear Research preprint, R-1985, Dubna (1965).
3. V.I. Danilov et al., Dubna JINR preprint, R-1853, Dubna (1964).
4. V.I. Danilov et al., Article in: Proceedings of the international accelerator conference (Dubna 1963). Moscow, Atompress, p.591 (1964).
5. J. Richardson et al., Phys. Rev., 73, 424 (1948).
6. K. MacKenzie, Nucl. Instrum. and Methods, 31, 139 (1964).
7. J. Lawson, Nucl. Instrum. and Methods 34, 173 (1965).
8. A.N. Sofonov, Dubna JINR preprint; R-2730. Dubna (1966).

DETERMINATION OF ACCELERATOR PERTURBATIONS FROM
INFORMATION ON PARTICLE LOSS DISTRIBUTION

I. P. Karabekov

UDC 621.384.612.22

The method for determining the perturbations of accelerator parameters from information on the beam secured without destroying the beam has a serious shortcoming: The devices measuring the beam trajectory variables are not sufficiently accurate in the initial phase of acceleration. The chief reasons for this are: the low signal/noise ratio at the outputs of the sensors at the time of injection, and the fact that the beam is not yet bunched at the time of injection. We therefore have to find methods for determining deviations of the accelerator parameters from their predicted values on the basis of an analysis of the azimuthal distribution of particles hitting the vacuum chamber walls during the first few revolutions.

This article takes up a method for analyzing the azimuthal distribution of particles lost, a method which in principle allows for adjustment of the adjustment system, determination of field perturbations in the accelerator magnetic system, and measurement of coherent phase oscillation variables.

Suppose that the particles injected at the point of entry to the annular chamber are distributed arbitrarily over the phase plane r_0, r'_0 . In the absence of perturbations of the accelerator variables, only those particles will be captured which are inside the phase ellipse of the annular accelerator (the a-ellipse). Particles outside the a-ellipse will be lost. But each point on the phase plane matches a point on the azimuth where the condition

$$|C_i| |F(\theta)| \cos C_i^* F(\theta) = \frac{A}{4} \quad (1)$$

holds. Here A is the diameter across the vacuum chamber for the given degree of freedom; $F(\theta)$ is the instantaneous value of the Floquet functions; C_i and C_i^* are the complex-conjugate constants in the solution of the particle equation of motion:

$$C_i = \frac{1}{2} (r_{0i} F_{0i}^* - i r'_{0i} F_{0i}^*) \quad (2)$$

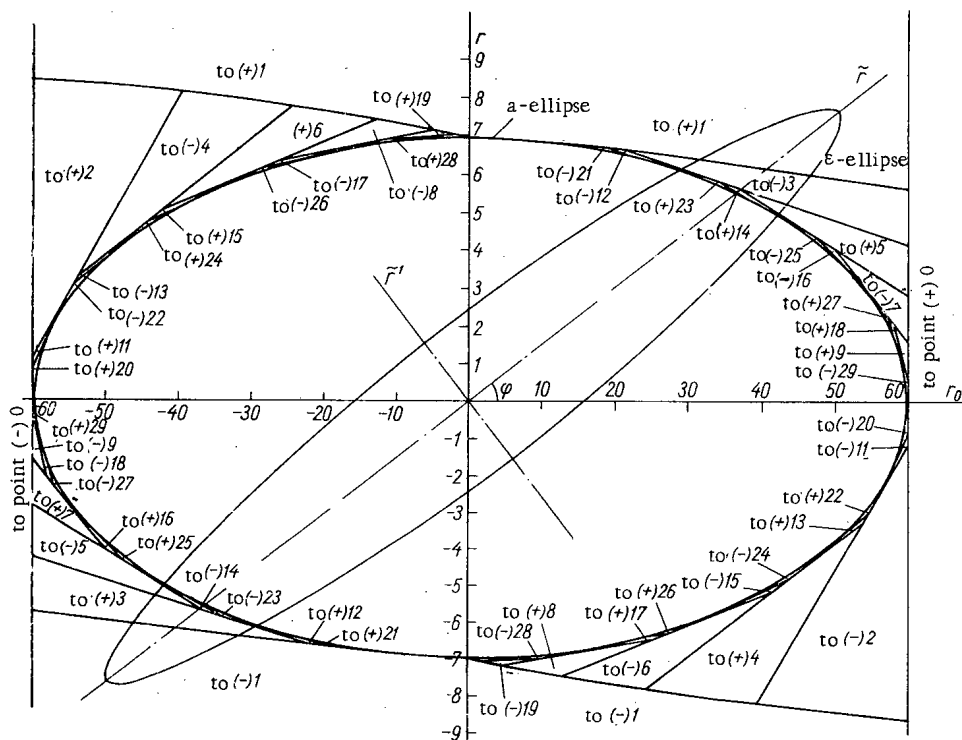
We can readily find the regions on the r_0, r'_0 plane in which a particle will fall in the specified azimuthal region, by using formulas (1) and (2). By measuring the distribution of particles falling in different intervals of the annulus, we can then reconstitute the particle distribution on the phase plane at the time of injection.

The diagram shows the phase a-ellipse computed for the Erevan cyclic electron accelerator †. The regions are shown around the ellipse, and those azimuthal intervals where these regions will be lost are duly noted. Clearly, particles will be lost on ascending intervals $|F(\theta)|$ up to the point $|F(\theta)|_{\max}$. The number of such azimuthal intervals is 24 per revolution in the case of the Erevan accelerator. On this diagram the number assigned to the region corresponds to the number designating the interval between the $\Phi\Phi$ -halves counting from the azimuthal interval where the particles were injected. Plus and minus signs indicate the direction in which particles are propelled; (+) toward the center of the annulus and (-) away from the center. The diagram clearly shows that the further a specified azimuthal interval lies from the particle injection point, the smaller the corresponding region on the phase plane will be. Note also that these regions are localized around points $|F_i(\theta)|_{\max}$ lying on the same a-ellipse.

Suppose that sensors measuring the number of particles lost are placed in certain azimuthal intervals, and that the injected ellipse occupies some arbitrary position on the r_0, r'_0 plane. In that case

† Yu.G. Agbalyan et al., Article in: Proceedings of the International Accelerator Conference. Dubna, 1963. Moscow, Atom press, p.235, 1964.

Translated from Atomnaya Énergiya, Vol.21, No.5, pp.404-406, November, 1966. Original article submitted December 21, 1965; revised April 9, 1966.



particle losses will be observed in those azimuthal intervals (see diagram) whose counterpart regions on the phase plane are covered by the phase ellipse of the injected beam (the ϵ -ellipse). We can then arrive at the ratio of ϵ -ellipse axes at which one small region will be covered at the point where the ϵ -ellipse and the a -ellipse intersect; this can be done by placing lenses on the injection interval. To visualize this, we can rotate the axis of the ϵ -ellipse to maximize the number of particles falling on the azimuthal interval selected and then, by altering the ratio of axes, minimize the number of particles lost in adjacent regions. The rotation angle φ of the axes of the ϵ -ellipse can then be found to within $\pm\Delta\varphi$, where $\Delta\varphi$ is determined by the angular extent of the small region.

The centers of the two ellipses will coincide, in the absence of perturbations, in the accelerator magnet system and when deflectors are precision-adjusted. In that case the number of particles lost on azimuthal intervals corresponding to diametrically opposed regions will be the same regardless of the rotation angle of the ϵ -ellipse axes. Consider the case where we have to deal simultaneously with field perturbations in the magnetic system and with errors in the adjustment of the deflector system, with a resulting shift in the center of the ϵ -ellipse. Since some particle density distribution must inevitably take place in the direction of the ϵ -ellipse axes, the shift of the center will bring about a difference in the number of particles falling in the diametrically opposed regions.

The deflectors must be adjusted as follows. By rotating the ϵ -ellipse, we find the difference in the number of particles lost in diametrically opposed regions over the whole perimeter of the a -ellipse. We can next achieve a proportionate decrease in this difference, by a suitable choice of deflector parameters, as the angle φ is varied over 2π . The sequence of operations enables us to determine the parameters of the deflectors at which the shift of the ellipse centers will be minimized. The uncompensated part of the shift will then be held accountable to magnetic field perturbation.

The amplitude and phase of the perturbation harmonic of the field must be determined by rotating the ϵ -ellipse and then measuring the magnitude and sign of the difference in charged particles on azimuthal intervals separated by a quarter-wavelength of the betatron oscillations. Familiar methods for determining the amplitude and phase of the perturbation harmonic then come into play.

Next we estimate the exactness with which we can measure the shift of the center of the ϵ -ellipse from the origin. Clearly, this degree of exactness will determine the resolution of the proposed method.

Since the shape of the particle density distribution along the axes of the ε -ellipse is not known exactly, the best course is to take a normal (Gaussian) distribution. And since the area of the small region is much smaller than the area of the ε -ellipse, the number of particles lost on that region can be approximated by the formula

$$N_i = A \frac{S_i}{\sigma} e^{-\frac{\rho_i^2}{2\sigma^2}}, \quad (3)$$

where N_i is the number of particles in the i -th region; S_i is the area of the i -th region; A is a constant determined by the total intensity of the injected beam; σ is the normal distribution parameter; and ρ_0 is the radius vector to the center of the i -th region.

We shift the center of the ε -ellipse a slight distance $\Delta\rho$ in the direction of the radius vector. We then have, in the first approximation

$$\frac{N_{i(+)} - N_{i(-)}}{N_{i(+)} + N_{i(-)}} = \frac{2\rho_0\Delta\rho}{\sigma^2}, \quad (4)$$

where $N_{i(+)}$ and $N_{i(-)}$ state the number of particles lost on azimuthal intervals matching the diametrically opposed regions on the phase plane. We have from Eq.(4) that the smaller the distribution parameter σ , the larger the difference in number of particles lost for small displacements $\Delta\rho$ of the center of the ellipse. Hence, if we assume $\sigma = (1/2)\rho_0$, the displacement $\Delta\rho/\rho_0 = 0.01$ will result in a relative difference 0.08 in the number of particles lost [see the left-hand side of Eq.(4)]. If this value is practically realizable, i.e., if the difference in number of particles lost can be measured to within $\approx \pm 10\%$, then $\Delta\rho/\rho_0$ can be found to within $\approx \pm 1\%$.

After the magnetic field and the deflectors have been corrected, we must then bring like axes of the two ellipses into coincidence and achieve similarity through an appropriate choice of ratio of semi-axes of the ε -ellipse. In practice, this step must reduce to setting $\varphi = 0$ and completely inscribing the ε -ellipse in the α -ellipse with the aid of focusing devices placed at the injection interval.

Particle losses due to phase oscillations occur at maxima of the function $\psi(\theta)$, which we can find from

$$r_{\text{lost}} = \psi(\theta) \frac{\Delta E}{E_0}, \quad (5)$$

where $\Delta E/E_0$ is the deviation of the particle energy from nominal value. If the particles execute only free incoherent oscillations about the equilibrium phase, then the beam will expand at points where $\psi(\theta)$ is maximized. Accordingly, the number of particles striking the surface of the chamber on both sides of the beam axis will be the same.

Coherent phase oscillations are responsible for time-varying differences in the number of particles lost on the chamber walls on both sides of the beam axis:

$$N_{i(+)} - N_{i(-)} \approx \frac{\Delta E}{E_0} (t). \quad (6)$$

Analysis of the difference (6) yields the amplitude and frequency of the coherent phase oscillations. How correctly the injection time was chosen becomes clear from that difference too. If there is a delay between the time the particles are injected and the time when the field H_{0z} attains the required value, then differences of type (6) must be of the same sign at all points $\psi(\theta)_{\text{max}}$. We can then minimize this difference by selecting the time of particle injection into the annular chamber.

In conclusion, the author thanks Yu. F. Orlov, S. M. Rubchinskii, A. A. Vasil'ev, A. I. Dzerkach, N. L. Sosenskii, A. A. Kuz'min, and G. I. Batskikh for their valuable comments, and M. A. Garzoyan for his kind assistance in the calculations.

EFFECTIVE METHOD OF PERFORMING
MULTIGROUP REACTOR CALCULATIONS

V. V. Khromov and A. M. Kuz'min

UDC 621.039.51.13

The solution of spatial and energy problems of reactor engineering is frequently very cumbersome and consumes a great deal of machine time. It is therefore desirable to have a method which ensures good accuracy of the calculated values of fundamental reactor parameters with a small expenditure of machine time. Recently such methods have begun to be developed intensively.

Schemes have been proposed [1, 2] based on the assumption that the neutron spectrum in the reactor may be represented by a finite sum of terms in which the spatial and energy variables are separated. The energy (or spatial) dependence of these terms is postulated and equations are determined for the coefficients as functions of the spatial (energy) variables. The trouble with this method is that the accuracy of the calculations is intrinsically dependent on how good a guess is made for the postulated dependence. The method described below is not open to this objection.

To simplify the calculation let us consider a one-dimensional, multi-region, quasicritical reactor with axial symmetry in the diffusion approximation. The generalization of the method to the neutron transport equation in principle presents now difficulty. We write the multigroup equations in vector-matrix form

$$-\nabla \hat{D} \nabla \Phi(r) + \hat{P} \Phi(r) = \frac{1}{K} \chi [\nu \Sigma_f, \Phi(r)] \quad (1)$$

subject to the condition that the neutron flux $\Phi(r)$ vanishes at the outer boundary of the reactor $r=R$. In eq. (1) the matrix \hat{D} characterizes the diffusion of neutrons and matrix \hat{P} their absorption and scattering, both elastic and inelastic; the vector χ is the fission spectrum and $\nu \Sigma_f$ is the product of the number of neutrons per fission, ν , and the fission cross section Σ_f ; the order of all matrices and vectors is equal to the number of energy groups N . Henceforth we will suppose that the properties of the medium are constant within a zone of thickness Δr_i ($i = 1, 2, \dots, n$).

Let us divide the energy range into m intervals each of which contains several energy groups Δ_α , where $\sum_{\alpha=1}^m \Delta_\alpha = N$. Let us suppose that in the interval Δr_i the group fluxes $\Phi_k(r)$ in energy interval α all have the same spatial dependence, i.e., for all $k \in \Delta_\alpha$:

$$\Phi_k(r) = I_k \varphi_\alpha(r). \quad (2)$$

For each reactor zone we introduce the functions

$$f_\alpha^{(i)}(r) = \varphi_\alpha(r) \sum_{k \in \Delta_\alpha} I_k^{(i)}; \quad (3)$$

$$F_k^{(i)} = I_k^{(i)} \int_{\Delta r_i} \varphi_\alpha(r) r dr, \quad (4)$$

where $f_\alpha^{(i)}(r)$ is the neutron flux in zone i summed over the groups in energy interval α , and $F_k^{(i)}$ is the integrated neutron flux in group k in zone i . Summing Eq.(1) over the groups in energy interval α and using assumption (2) we obtain the equations ($\alpha = 1, 2, \dots, m$)

$$-\langle D \rangle_\alpha^{(i)} \Delta f_\alpha^{(i)}(r) + \langle \Sigma \rangle_\alpha^{(i)} f_\alpha^{(i)}(r) - \sum_{\beta=1}^{\alpha-1} \langle \Sigma \rangle_{\beta \rightarrow \alpha}^{(i)} f_\beta^{(i)}(r) = \frac{1}{K} \langle \chi \rangle_\alpha^{(i)} \sum_{\beta=1}^m \langle \nu \Sigma_f \rangle_\beta^{(i)} f_\beta^{(i)}(r). \quad (5)$$

which must be solved subject to the continuity of the functions $f_\alpha(r)$ and $\langle D \rangle_\alpha \nabla f_\alpha(r)$ and the vanishing of $f_\alpha(r)$ at the reactor boundary. In Eq. (5) the quantities in brackets represent few-group macroscopic cross sections averaged by the formulas

Translated from *Atomnaya Énergiya*, Vol.21, No.5, pp.406-408, November, 1966. Original article submitted June 9, 1966.

$$\left. \begin{aligned}
 \langle D \rangle_{\alpha}^{(i)} &= \frac{1}{A_{\alpha}^{(i)}} \sum_{h \in \alpha} D_h^{(i)} F_h^{(i)}; \\
 \langle v \Sigma_f \rangle_{\alpha}^{(i)} &= \frac{1}{A_{\alpha}^{(i)}} \sum_{h \in \alpha} (v \Sigma_f)_h^{(i)} F_h^{(i)}; \\
 \langle \Sigma \rangle_{\alpha}^{(i)} &= \frac{1}{A_{\alpha}^{(i)}} \sum_{h \in \alpha} \left(\Sigma_h^{(i)} F_h^{(i)} - \sum_{j \in \alpha} \Sigma_{j \rightarrow h}^{(i)} F_j^{(i)} \right); \\
 \langle \chi \rangle_{\alpha}^{(i)} &= \sum_{h \in \alpha} \chi_h^{(i)}; \\
 \langle \Sigma \rangle_{\beta \rightarrow \alpha}^{(i)} &= \frac{1}{A_{\beta}^{(i)}} \sum_{j \in \beta} \sum_{h \in \alpha} \Sigma_{j \rightarrow h}^{(i)} F_j^{(i)}; \quad A_{\alpha}^{(i)} = \sum_{h \in \alpha} F_h^{(i)}.
 \end{aligned} \right\} \quad (6)$$

We obtain the equations for the integrated fluxes $F_k^{(i)}$ by integrating Eq.(1) over the volume of each reactor zone ($i=1, 2, \dots, n$):

$$-\hat{D}^{(i)} \nabla \Phi(r) \Big|_{r=r_{i-1}}^{r=r_i} + \hat{P}^{(i)} F^{(i)} = \frac{1}{K} \chi^{(i)} (v \Sigma_f^{(i)}, F^{(i)}). \quad (7)$$

Using assumption (2) and the continuity of $\Phi(r)$, $\hat{D} \nabla \Phi(r)$ we write the k^{th} component of the vector $\hat{D}^{(i)} \nabla \Phi(r) \Big|_{r=r_i}$, belonging to energy interval α , in two different forms

$$D_h^{(i)} \nabla \Phi_h(r) \Big|_{r=r_i} = \begin{cases} \kappa_{\alpha}^{(i)}(r_i) D_h^{(i)} F_h^{(i)}, & \text{if } \nabla f_{\alpha}(r) \Big|_{r=r_i} < 0; \\ \kappa_{\alpha}^{(i+1)}(r_i) D_h^{(i+1)} F_h^{(i+1)}, & \text{if } \nabla f_{\alpha}(r) \Big|_{r=r_i} > 0; \end{cases} \quad (8')$$

$$D_h^{(i)} \nabla \Phi_h(r) \Big|_{r=r_i} = \left[\frac{1}{4} \gamma_{\alpha}^{(i+1)}(r_i) + \frac{1}{2} \kappa_{\alpha}^{(i+1)}(r_i) D_h^{(i+1)} \right] F_h^{(i+1)} - \left[\frac{1}{4} \gamma_{\alpha}^{(i)}(r_i) - \frac{1}{2} \kappa_{\alpha}^{(i)}(r_i) D_h^{(i)} \right] F_h^{(i)}, \quad (8'')$$

where the parameters $\kappa_{\alpha}^{(i)}$; $\gamma_{\alpha}^{(i)}$; $\kappa_{\alpha}^{(i+1)}$; $\gamma_{\alpha}^{(i+1)}$ are given by

$$\kappa_{\alpha}^{(i)}(r_i) = \frac{\nabla f_{\alpha}^{(i)}(r_i)}{A_{\alpha}^{(i)}}; \quad \gamma_{\alpha}^{(i)}(r_i) = \frac{f_{\alpha}^{(i)}(r_i)}{A_{\alpha}^{(i)}}; \quad \kappa_{\alpha}^{(i+1)}(r_i) = \frac{\nabla f_{\alpha}^{(i+1)}(r_i)}{A_{\alpha}^{(i+1)}}; \quad \gamma_{\alpha}^{(i+1)}(r_i) = \frac{f_{\alpha}^{(i+1)}(r_i)}{A_{\alpha}^{(i+1)}}. \quad (9)$$

Forms (8') and (8'') for the neutron currents at the zone boundaries lead to two types of equations for the multigroup integrated fluxes $F_k^{(i)}$.

Eqs. (5) and (7) form a complete set of equations which may be solved by the source iteration method [3].

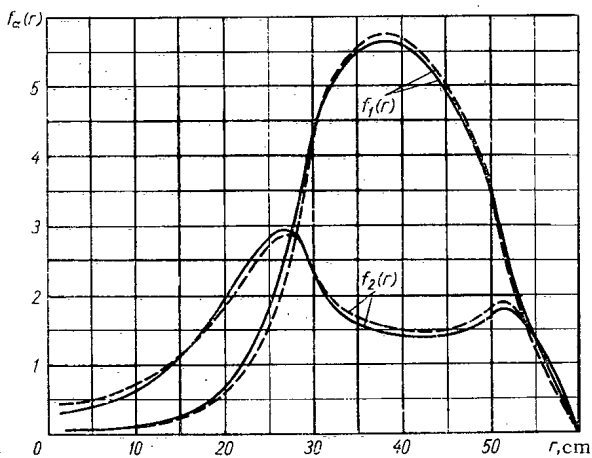


Fig.1. The spatial distribution of neutrons $f_{\alpha}(r)$ summed over the groups in energy interval α ($\alpha=1, 2$). Exact solution —; effective method - - -.

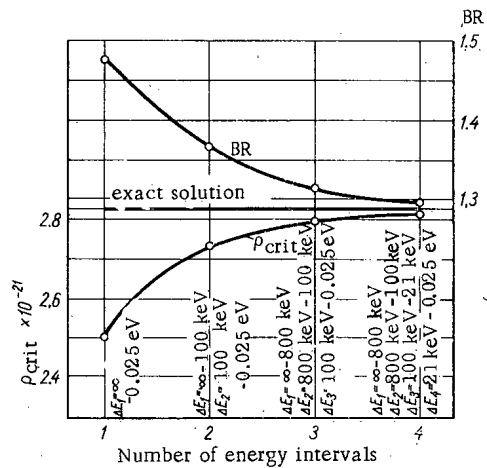


Fig.2. ρ_{crit} for Pu and BR as functions of the number of energy intervals selected. ΔE_{α} ($\alpha=1, 2, 3, 4$) are the energy intervals of the subdivisions.

Nuclear Densities ($\times 10^{24}$ nuclei/cm³)

Element	Zone number and dimensions		
	1 (0-30 cm)	2 (30-50 cm)	3 (50-60 cm)
U ²³⁸	0.01821	0.01800	0.01445
Pu ²³⁹	-	0.00273	-
Pu ²⁴⁰	-	0.00030	-
Fission products	-	0.00078	-
Sodium	0.00254	0.00635	0.00508
Steel	0.01696	0.00509	0.02544
Carbon	0.09104	-	0.07225
Niobium	-	0.00218	-

The use of the relation

$$\langle v \Sigma_f^{(i)}, F^{(i)} \rangle = \int_{\Delta r_i} \sum_{\alpha=1}^m \langle v \Sigma_f \rangle_{\alpha}^{(i)} f_{\alpha}(r) r dr \quad (10)$$

reduces the calculation of the integrated fluxes in each iteration to the problem of solving a set of inhomogeneous algebraic equations. For kth neutron group these equations may be written in the form

$$a_k^{(i-1)} F_k^{(i-1)} - b_k^{(i)} F_k^{(i)} + c_k^{(i+1)} F_k^{(i+1)} = -q_k^{(i)} \quad (11)$$

and solved by the factorization method like ordinary finite-difference equations with the number of points equal to the number of reactor zones.

To test the method a program was set up and calculations were performed for a fast reactor with an annular core whose composition and dimensions are given in the table. A comparison of the results obtained by the effective method with the straightforward solution of Eq. (1) shows good agreement for the total neutron distribution $f_{\alpha}(r)$ (Fig. 1.), the critical concentration of Pu²³⁹ (ρ_{crit}), and the breeding ratio BR (Fig. 2). The data presented in Figs. 1 and 2 were obtained by using form (8') for the neutron currents at the zone boundaries. Calculations show that form (8'') for the currents decreases the error in ρ_{crit} and BR by about a factor of two.

In conclusion we note that the effective method consumes only a fifth to a third as much machine time as ordinary multigroup calculations.

LITERATURE CITED

1. G. Calame and F. Federighi, Nucl. Sci. and Engr., 10, 190 (1961).
2. G. Pomraning, Nukleonik, Mai, 192 (1965).
3. G. I. Marchuk, Methods of Calculating Nuclear Reactors [in Russian], Moscow, Gosatomizdat (1961).

CALCULATING THE DOPPLER TEMPERATURE COEFFICIENT
OF REACTIVITY FOR HOMOGENEOUS REACTORS

F. M. Mitenkov, B. A. Averbakh,
L. M. Gorbunov, and O. B. Samoilov

UDC 621.039.512.26

The temperature derivative of the neutron resonance escape probability or the temperature derivative of the effective resonance integral must be taken into account in calculations of the Doppler temperature coefficient of reactivity for reactors. Results for a heterogeneous media with plates of resonance absorber separated by moderator layers can be found in [1]. This article deals with the problem for homogeneous media.

The q -th resonance escape probability is given in [2] as:

$$\langle \varphi \rangle_q = e^{-\frac{\rho_n}{\xi \Sigma_{sn}} J_{\text{eff}}^{(q)}} \quad (1)$$

where ρ_n is the concentration of resonance absorber nuclei in the homogeneous medium; Σ_{sn} is the potential macroscopic scattering cross section of the medium; J_{eff} is the effective resonance integral; ξ is the mean logarithmic energy decrement.

The formula for the temperature variation of the effective resonance integral, given proper assumptions (references [2, 3]) is given as

$$J_{\text{eff}}^{(q)} = J_R^{(q)} \frac{2a_q}{\pi} f(\xi, a_q) \quad (2)$$

Here $J_R = \frac{\pi}{2} \sigma_{0q} \frac{\Gamma_V^{(q)}}{E_q}$ is the resonance integral for an infinitely dilute medium; $a_q = \frac{\Sigma_{sn}}{\rho_n \sigma_{0q}}$; E_q is the energy for the q -th resonance maximum; $\Gamma_V^{(q)}$, $\Gamma^{(q)}$ are respectively the radiation level width and total level width; σ_0 is the total cross section at the resonance maximum; $\xi_q = \frac{\Gamma^{(q)}}{\Delta_q}$; $\Delta_q = 2 \sqrt{\frac{kT_{\text{eff}} E_q}{A}}$; k is Boltzmann's constant; T_{eff}^* is the effective temperature of the medium in $^{\circ}\text{K}$; and A is the atomic weight of the resonance absorber.

The temperature function of the resonance self-shielding factor is

$$f(\xi_q, a_q) = \int_0^{\infty} \frac{\psi(\xi_q, x)}{\psi(\xi_q, x) + a_q} dx, \quad (3)$$

where

$$\psi(\xi, x) = \frac{\xi}{2\sqrt{\pi}} \int_{-\infty}^{\infty} \frac{\exp\left[-\frac{1}{4}\xi^2(x-y)^2\right]}{1+y^2} dy.$$

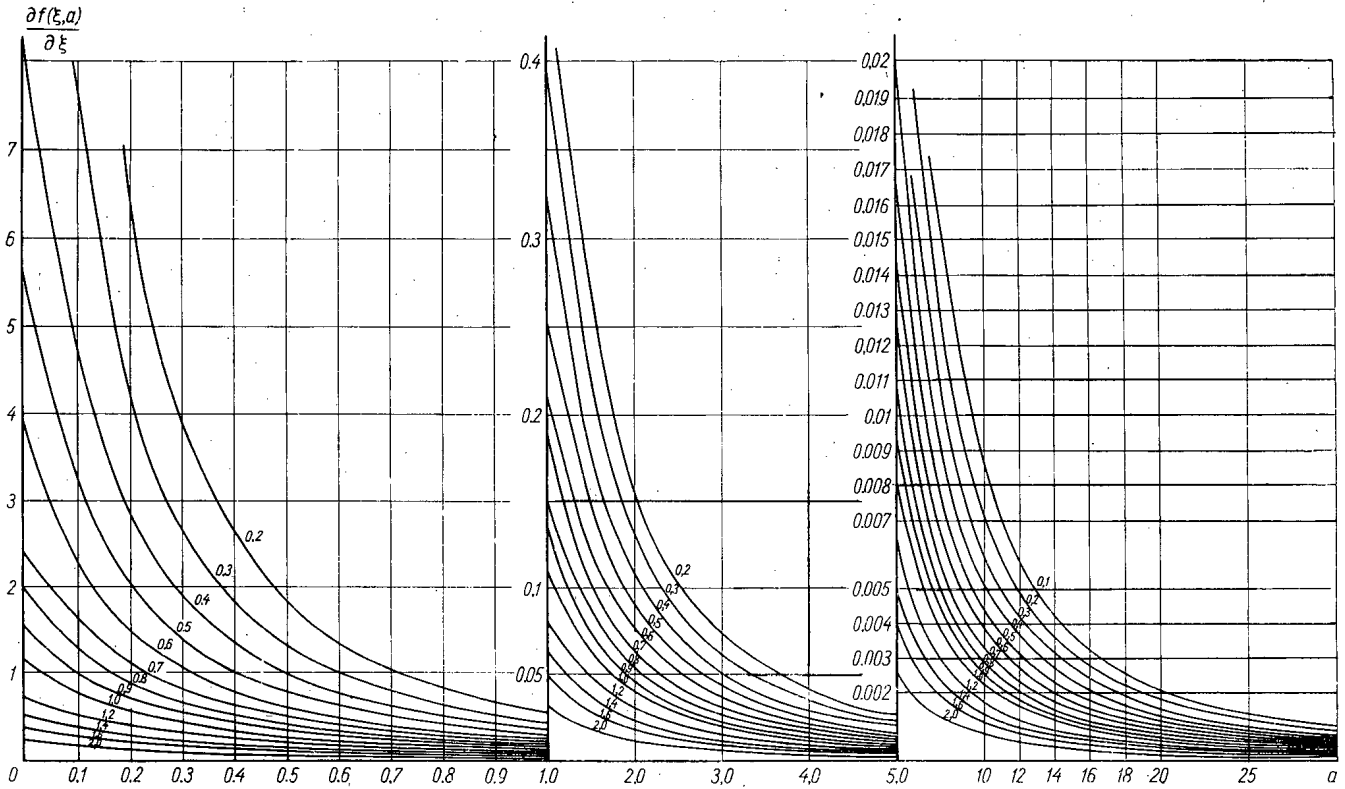
We can derive, from (1), a formula for the temperature derivative of $\langle \varphi \rangle_q$

$$\frac{\partial \langle \varphi \rangle_q}{\partial T} = -\langle \varphi \rangle_q \frac{\rho_n}{\xi \Sigma_{sn}} J_R^{(q)} \frac{2a_q}{\pi} \left[\frac{\partial f(\xi, a)}{\partial T_{\text{eff}}} \right]_q \frac{\partial T_{\text{eff}}}{\partial T}, \quad (4)$$

where

$$\left[\frac{\partial f(\xi, a)}{\partial T_{\text{eff}}} \right]_q = \frac{\partial f(\xi, a) \Big|_{\xi=\xi_q, a=a_q}}{\partial T_{\text{eff}}} = \left[\frac{\partial f(\xi, a)}{\partial \xi} \cdot \frac{\partial \xi}{\partial T_{\text{eff}}} \right]_q = - \left[\frac{\partial f(\xi, a)}{\partial \xi} \right]_q \frac{\xi_q}{2T_{\text{eff}}}. \quad (5)$$

* When the temperature of the medium $T > T_D$ (T_D is the Debye temperature), $T_{\text{eff}} = T$; when $T < T_D$, the effective temperature is a function of both the temperature of the medium and the Debye temperature [4, 5].



Graph of the function $\partial f(\xi, a)/\partial \xi$ (figures on the curves indicate ξ values).

According to [5], the function $\frac{\partial f(\xi, a)}{\partial \xi}$ has the form

$$\frac{\partial f(\xi, a)}{\partial \xi} = -\frac{4a}{\xi^3} \int_0^{\infty} \left[\frac{\partial \psi(\xi, x)}{\partial x} \right]^2 [\psi(\xi, x) + a]^{-3} dx. \tag{6}$$

On differentiating $\psi(\xi, x)$ with respect to x and substituting the result into formula (6), we obtain, after some transformations:

$$\frac{\partial f(\xi, a)}{\partial \xi} = -a\xi \int_0^{\infty} [\psi(\xi, x) + a]^{-3} \times \left[\frac{1}{2} \chi(\xi, x) - x\psi(\xi, x) \right]^2 dx, \tag{7}$$

where

$$\chi(\xi, x) = \frac{\xi}{\sqrt{\pi}} \int_{-\infty}^{\infty} \frac{\exp \left[-\frac{1}{4} \xi^2 (x-y)^2 \right]}{1+y^2} y dy.$$

The functions $\psi(\xi, x)$ and $\chi(\xi, x)$ are related to the real part $u(x, y)$ and imaginary part $v(x, y)$ of the complex probability integral by the formulas

$$\psi(\xi, x) = \xi \frac{\sqrt{\pi}}{2} u \left(x \frac{\xi}{2}, \frac{\xi}{2} \right); \tag{8}$$

$$\chi(\xi, x) = \xi \sqrt{\pi} v \left(x \frac{\xi}{2}, \frac{\xi}{2} \right). \tag{9}$$

When we substitute formulas (8) and (9) into (7), we end up with

$$\frac{\partial f(\xi, a)}{\partial \xi} = -\frac{a\xi^3 \pi}{4} \int_0^{\infty} \left[\xi \frac{\sqrt{\pi}}{2} u \left(x \frac{\xi}{2}, \frac{\xi}{2} \right) + a \right]^{-3} \times \left[v \left(x \frac{\xi}{2}, \frac{\xi}{2} \right) - xu \left(x \frac{\xi}{2}, \frac{\xi}{2} \right) \right]^2 dx. \tag{10}$$

The function $df(\xi, a)/d\xi$ was computed on the basis of formula (10) over the ranges $0.2 \leq \xi \leq 2$ and $0 \leq a \leq 30$. Numerical integration was performed on the URAL-2 electronic computer by a program using the method described in [6] to compute functions u and v . The results of these calculations are plotted in the diagram as curves of the function $df(\xi, a)/d\xi$.

LITERATURE CITED

1. G. Roe, The Absorption of Neutrons in Doppler Broadened Resonances. USAEC Report KAPL-1241 Knolls Atomic Power Laboratory, October 15 (1954).
2. G. I. Marchuk, Numerical Methods in Nuclear Reactor Calculations, Moscow, State atom press [in Russian] (1961).
3. I. V. Gordeev, V. V. Orlov, and T. Kh. Sedel'nikov, Atomnaya Énergiya, 9, 252 (1957).
4. I. V. Gordeev, D. A. Kardashev, and A. V. Malyshev, Nuclear Physics Constants, Moscow, State atom press [in Russian] (1963).
5. L. Dresner, Resonance Absorption in Nuclear Reactors, Moscow, State atom press [in Russian] (1962).
6. V. N. Faddeeva and N. M. Terent'ev, Tables of Values of Function $W(2)$ for Complex Argument, Pergamon, N. Y. (1961).

EFFECTIVENESS OF A SYSTEM OF CONTROL RODS DISTRIBUTED THROUGH A REACTOR CORE AND REFLECTOR

V. I. Nosov

UDC 621.039.51

In reactor engineering practice the commonest method of controlling the reactivity of reactor is by the insertion of rods made of material having a large neutron absorption cross section. Using the results of [1-3] the present report considers rods distributed over the cross section of a homogeneous thermal reactor with an arbitrary density.

In a cylindrical reactor with an arbitrary distribution of absorbing rods through the core and radial reflector, the matrix form of the solution for the fast flux Φ_1 and the thermal flux Φ_2 has the form

$$\Phi^I \equiv \begin{bmatrix} \Phi_1^I \\ \Phi_2^I \end{bmatrix} = \begin{bmatrix} S_1 & S_2 \\ 1 & 1 \end{bmatrix} \begin{bmatrix} L^I \\ T^I \end{bmatrix}; \Phi^{II} \equiv \begin{bmatrix} \Phi_1^{II} \\ \Phi_2^{II} \end{bmatrix} = \begin{bmatrix} S_3 & 0 \\ 1 & 1 \end{bmatrix} \begin{bmatrix} L^{II} \\ T^{II} \end{bmatrix} \quad (1)$$

Here

$$\begin{aligned} \begin{bmatrix} L^I \\ T^I \end{bmatrix} &= \sum_{n=0}^{\infty} \begin{bmatrix} J_n(\alpha r) & 0 \\ 0 & J_n(\beta r) \end{bmatrix} \begin{bmatrix} A_{1n} \cos n\varphi + E_{1n} \sin n\varphi \\ A_{2n} \cos n\varphi + E_{2n} \sin n\varphi \end{bmatrix} + \sum_{k=0}^{\infty} \sum_{s=0}^M \begin{bmatrix} Y_k(\alpha \rho_s) & 0 \\ 0 & K_k(\beta \rho_s) \end{bmatrix} \times \begin{bmatrix} B_{1ks} \cos k\omega_s + P_{1ks} \sin k\omega_s \\ B_{2ks} \cos k\omega_s + P_{2ks} \sin k\omega_s \end{bmatrix} \\ \begin{bmatrix} L^{II} \\ T^{II} \end{bmatrix} &= \sum_{n=0}^{\infty} \begin{bmatrix} I_n(\nu r) (C_{2n} \cos n\varphi + F_{2n} \sin n\varphi) + K_n(\nu r) (D_{2n} \cos n\varphi + H_{2n} \sin n\varphi) \\ I_n(\mu r) (C_{1n} \cos n\varphi + F_{1n} \sin n\varphi) + K_n(\mu r) (D_{1n} \cos n\varphi + H_{1n} \sin n\varphi) \end{bmatrix} \\ &+ \sum_{m=0}^{\infty} \sum_{i=1}^N \begin{bmatrix} K_m(\nu \rho_i) & 0 \\ 0 & K_m(\mu \rho_i) \end{bmatrix} \times \begin{bmatrix} B_{2mi} \cos m\omega_i + P_{2mi} \sin m\omega_i \\ B_{1mi} \cos m\omega_i + P_{1mi} \sin m\omega_i \end{bmatrix} \end{aligned} \quad (2)$$

where M and N are the numbers of rods in the core and reflector respectively; I and II refer to the core and reflector respectively; s and i number the rods in the core and reflector respectively; s=0 refers to the central rod (for it k=0); r is the distance from the center of the reactor to an arbitrary point P'; ρ_s and ρ_i are the distances from the centers of rods s and i to point P'; φ , ω_s , ω_i are the azimuthal angles in systems of polar coordinates fixed respectively at the reactor center and at the centers of rods s and i [1-3]; A, B, C, D, E, F, H, and P, with appropriate subscripts are constants; S_1, S_2 , and S_3 are coupling constants.

From the conditions for the continuity of fluxes and currents of fast and thermal neutrons at the core-reflector boundary $r=R_{\text{core}}$

$$\Phi_1^I = \Phi_1^{II}; \quad \Phi_2^I = \Phi_2^{II}; \quad \frac{d\Phi_1^I}{dr} = \gamma_2 \frac{d\Phi_1^{II}}{dr}; \quad \frac{d\Phi_2^I}{dr} = \gamma_0 \frac{d\Phi_2^{II}}{dr} \quad (3)$$

it follows that

$$\begin{aligned} (A_{2n}, E_{2n}) &= (A_{1n}, E_{1n}) f_n - \sum_{m=0}^{\infty} \sum_{i=1}^N \times [B_{2mi} \bar{\Phi}_{nm}(\cos n\varphi_i, \sin n\varphi_i) \mp P_{2mi} \bar{\Phi}_{nm}(\sin n\varphi_i, \cos n\varphi_i)] + \sum_{k=0}^{\infty} \sum_{s=0}^M [B_{1ks} \Psi_{nk} \\ &\times (\cos n\varphi_s, \sin n\varphi_s) \mp P_{1ks} \bar{\Psi}_{nk}(\sin n\varphi_s, \cos n\varphi_s)] - [B_{2ks} \bar{\Phi}_{nk}(\cos n\varphi_s, \sin n\varphi_s) \mp P_{2ks} \bar{\Phi}_{nk} \times (\sin n\varphi_s, \cos n\varphi_s)]; \\ (A_{1n}, E_{1n}) &= \sum_{m=0}^{\infty} \sum_{i=1}^N [(B_{1mi} R_{nm} + B_{2mi} T_{nm}) \times (\cos n\varphi_i, \sin n\varphi_i) \mp (P_{1mi} \bar{R}_{nm} + P_{2mi} \bar{T}_{nm}) \\ &\times (\sin n\varphi_i, \cos n\varphi_i)] + \sum_{k=0}^{\infty} \sum_{s=0}^M [(B_{1ks} R_{nk} + B_{2ks} T_{nk}) \times (\cos n\varphi_s, \sin n\varphi_s) \mp (P_{1ks} \bar{R}_{nk} + P_{2ks} \bar{T}_{nk}) \times (\sin n\varphi_s, \cos n\varphi_s)] \end{aligned} \quad (4)$$

Translated from *Atomnaya Energiya*, Vol. 21, No. 5, pp. 410-412, November, 1966. Original article submitted March 22, 1966; revised May 19, 1966.

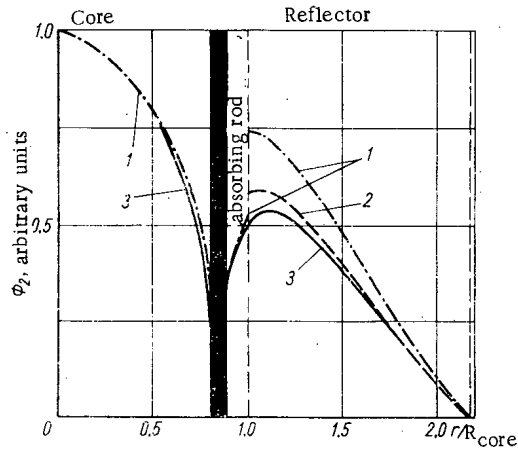


Fig. 1. The radial distribution of the thermal neutron flux Φ_2 with one rod in the core ($R_r = 0.84 R_{\text{core}}$); $\varphi = 0$ corresponds to a radial line through the center of the reactor and the center of the rod. 1) $n=0, k=0$; 2) $n=0-2, k=0-8, k=0$ ($n=0-8, k=1$).

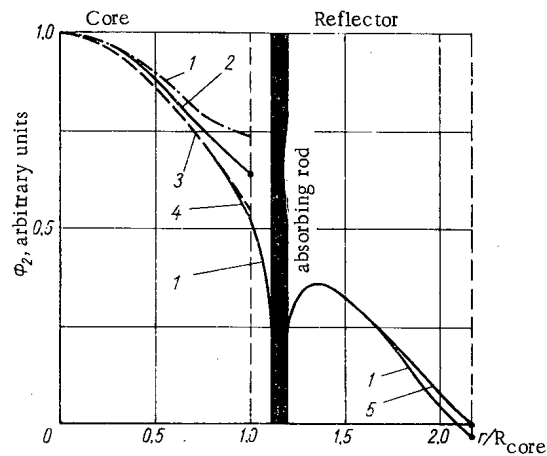


Fig. 2. The radial distribution of the thermal neutron flux Φ_2 with one rod in the radial reflector ($R_r = 1.16 R_{\text{core}}$, $\varphi = 0$). 1) $n=0, k=0-2$; 2) $n=0-2, k=0$; 3) $n=0-7, k=0$; 4) $n=0-10, k=1$; 5) $n=0-7, k=0$ ($n=0-10, k=1$).

The functions $f_n, \Phi_{nm}, \dots, R_{nk}, T_{nk}$ have the same form as the corresponding function $f_n, \Phi_{nm}, \dots, T_{nk}$ in [1, 3]; similar relations may be written for the constants C_{1n}, F_{1n} and C_{2n}, F_{2n} . In obtaining Eq. (4) use was made of the appropriate addition theorems for Bessel functions [4] and relations between the constants D_{1n}, D_{2n} , and H_{1n}, H_{2n} , which follow from the boundary conditions for Φ_1 and Φ_2 at the surface of the reactor (at $r = R_{\text{ext}}, \Phi_1^I = \Phi_2^I = 0$) [3].

Using the boundary conditions for Φ_1 and Φ_2 [$(d\Phi_1/d\rho)\Phi_1^{-1} = d^{-1}$, $(d\Phi_2/d\rho)\Phi_2^{-1} = \gamma^{-1}$] at each of the absorbing rods in the core and reflector, we obtain equations similar to Eq. (5) of [3]. The criticality condition is obtained by requiring that the determinant of the system of linear homogeneous algebraic equations vanish. The effectiveness of the system of rods is determined by the difference of the effective neutron multiplication constants in the presence and absence of the absorbing rods in the reactor.

In most practical cases the calculation of rod effectiveness may be limited to the zero order approximation $m=k=n=0$, particularly if the rods are symmetrically placed in the reactor [1, 2]. For an asymmetric arrangement of rods the calculation of the radial flux distribution without taking into account the higher order terms in the expansion leads to fluxes which do not join at the core-reflector boundary.

Figures 1 and 2 show the radial distribution of the thermal neutron flux Φ_2 with rods in the core and reflector. It is assumed that the 2.2 cm diameter rods are absolutely black for thermal neutrons and neither slow down nor absorb fast neutrons. Beryllium oxide of density 2.8 g/cm^3 is used as a moderator in the core and as reflector material; neutron data and the physical characteristics of the system are listed in [5, Table 3]. The radius of the reactor $R_R = 2.18 R_{\text{core}}$; the equivalent core height is $H_{\text{core}}^{\text{eq}} = 1.65 R_R$. As is clear from Figs. 1 and 2, the higher order terms in the expansion have a significant effect on the neutron flux distribution, particularly at points close to the core-reflector boundary. At the same time the calculated rod effectiveness, as follows from the tabulated data (cf. also [1, 2]) does not change much when higher order terms are taken into account.

Figure 3 shows the thermal neutron flux distribution when eight rods are symmetrically placed in the reflector. The distribution was calculated by taking into account two terms ($n=0-1$) in the expansion for the angular dependence over the reactor, and the first term ($k=0$) in the series giving the azimuthal dependence at the surface of an absorbing rod. As may be seen from Fig. 3, the latter terms in the expansion need not be taken into account for this symmetric arrangement of rods.

The results presented were calculated on the M-20 computer. The program for this machine allows the calculation of the effective multiplication constant k_{eff} and the neutron flux distribution over

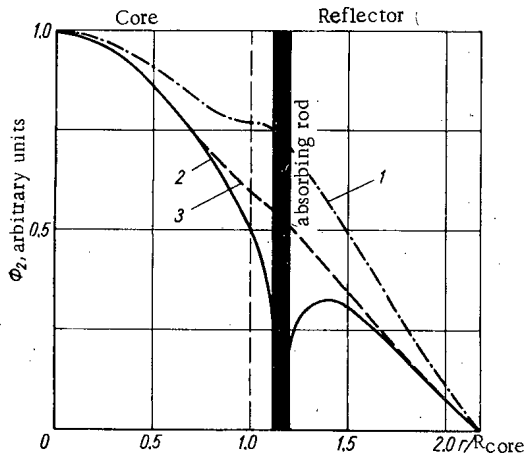


Fig. 3. The radial distribution of the thermal neutron flux Φ_2 with eight rods uniformly spaced in a ring in the reflector ($\Delta k_{eff} = 11\%$). 1) Reactor without rods; 2) $\varphi = 0$; 3) $\varphi = \pi/8$.

Values of Δk_{eff} (in %) for a Rod of Diameter 2.2 cm Calculated in Various Approximations

R_T / R_{core}	$k = 0$			$k = 1$	
	$n = 0$	$n = 0-2$	$n = 0-7$	$n = 0-2$	$n = 0-7$
0.84	3.18	3.08	3.07	3.03	3.03
1.16	1.48	1.48	1.49	1.45	1.45
1.35	0.847	0.852	0.855	0.832	0.835

Note: R_T is the distance from the center of the reactor to the center of the rod.

the cross section of a reactor with one rod or with a system of absorbing rods arranged symmetrically in the core or reflector. Values of k_{eff} and the neutron flux distribution may be computed either by taking into account the angular dependence over the reactor ($n=0-10$) and on the surface of a rod ($k=0, 1$) or in the approximation $k=n=0$.

The author thanks N. N. Ponomarev-Stepnom and E. S. Glushkov for their help, and gratefully acknowledges the large contribution to setting up the M-20 program made by S. G. Zlobin.

LITERATURE CITED

1. V. I. Nosov, *Atomnaya Energiya*, 9, 262 (1960).
2. V. I. Nosov, *Atomnaya Energiya*, 10, 269 (1961).
3. V. I. Nosov, *Atomnaya Energiya*, 15, 71 (1963).
4. G. N. Watson, *Theory of Bessel Functions*, Cambridge U.P., N.Y.
5. I. I. Bondarenko et al., paper No. 362 presented by USSR at the Third International Conference on the Peaceful Uses of Atomic Energy, Geneva (1964).

SEMICONDUCTOR (GERMANIUM) γ -RAY SPECTROMETER
DETERMINES BURNUP IN FUEL ELEMENTS

L. V. Groshev, A. M. Demidov,
G. A. Kotel'nikov, and O. A. Miller

UDC 539.107.8:621.039.548.3

Determinations of nuclear fuel burnup by the intensity of γ -radiation from fission product isotopes is a method which is gaining in popularity. Rassmussen et al. [1], followed later by Rochlin et al. [2], suggested using a γ -ray diffraction spectrometer to record the γ -ray emission of irradiated fuel elements. Groshev and Demidov suggested using a magnetic Compton spectrometer [3], Owen [4], Diggle and Blackader [15] suggested using a NaI crystal γ -ray spectrometer, Higatsberger et al. suggested a silicon detector γ -ray detector [6, 7]. The intensity of γ -ray emission from a variety of long-lived nuclides (Cs^{137} , Ce^{144} , Ba^{140} , etc.) was measured by the above authors in their nuclear fuel burnup determinations.

The isotope best suited for fuel element depletion determinations is Cs^{137} with its very extended half-life ($T_{1/2} = 30$ years), its rather high fission yield, and the almost one hundred percent gamma yield per single beta decay event. Cs^{137} burnup determination is also attractive in the burnup can then be measured under practical fuel irradiation conditions, with long irradiation and exposure times and, most important of all, when the precise irradiation conditions are not known.

Note, however, that it is no easy job to detect the Cs^{137} 661 keV γ -emission line in an irradiated fuel element spectrum since we have to use a fairly high-resolution (better than 1%) γ -ray spectrometer in that γ -energy region, with a quite high spectrometer luminosity. We can get all this with the germanium detector γ -ray spectrometer, which possesses distinct advantages over the γ -ray spectrometers used in the work described in [1-7].

The work described here was undertaken in order to examine the possible use of germanium γ -ray detectors to determine burnup in fuel elements, and that is why the experiments were carried out not on the whole element, but on a part of the element weighing 180 mg.

The sample was housed in lead shielding at a distance of 100 cm from the detector. The γ -beam was collimated by a 10-mm diameter diaphragm. Pulses from the germanium detector were presented

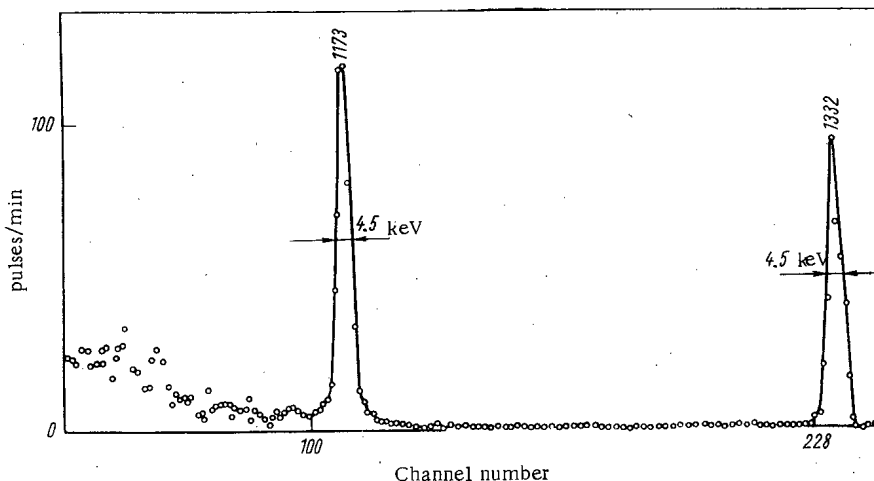


Fig.1. Co^{60} γ -emission spectrum.

Translated from *Atomnaya Energiya*, Vol. 21, No.5, pp. 412-415, November, 1966. Original article submitted June 13, 1966.

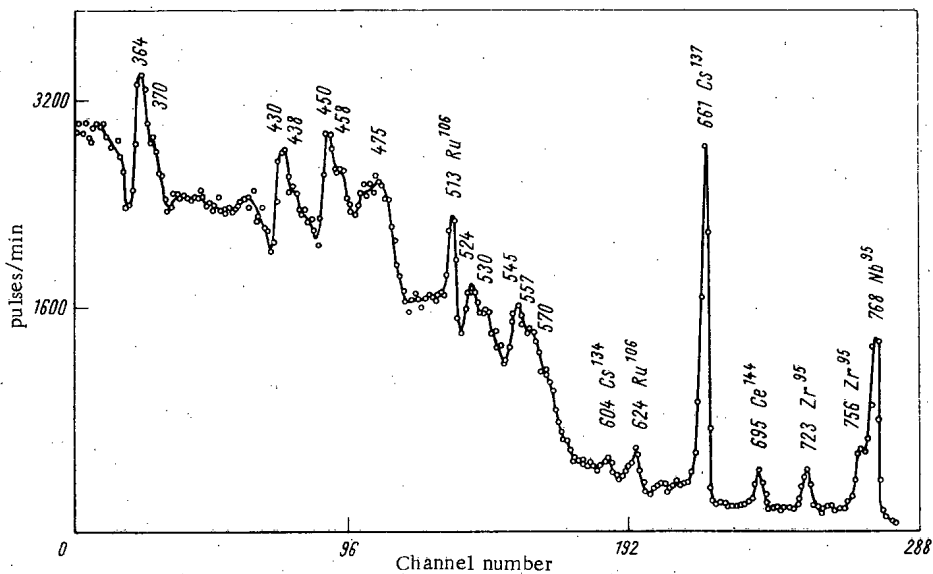


Fig.2. Fuel element γ -emission spectrum. $E_\gamma = 0.3$ to 0.8 MeV.

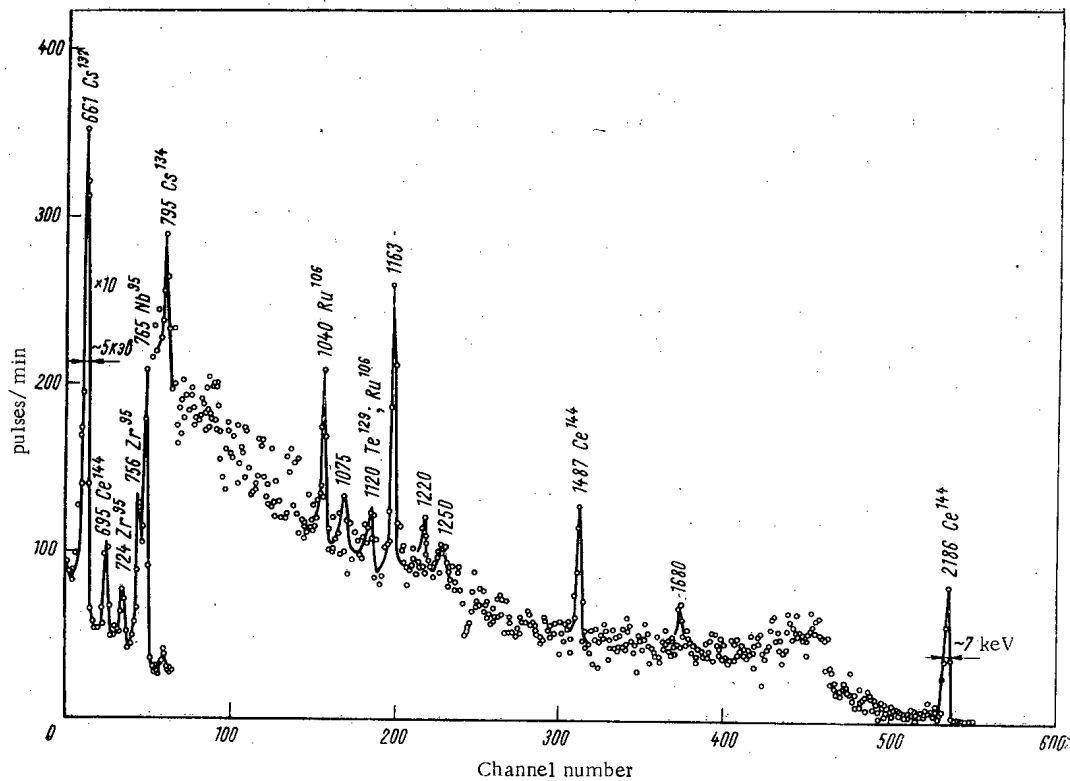


Fig.3. Fuel element γ -emission spectrum. $E_\gamma = 0.6$ to 2.2 MeV.

to a preamplifier with a low noise level, and then to an amplifier, a pulse-height discriminator, and finally to a 512-channel pulse-height analyzer.

Energies and Intensities of γ -Lines Identified in Fuel Element Spectrum

E_γ , keV	I_γ , relative units	Nuclide	$T_{1/2}$	E_γ , keV	I_γ , relative units	Nuclide	$T_{1/2}$
2186 *	100	Ce ¹⁴⁴	284 Days	795 (5)	40	Cs ¹³⁴	2.07 Years
1680	12	(2186—511)	284 »	765 (4)	630	Nb ⁹⁵	35 Days
1487 *	43	Ce ¹⁴⁴	284 »	756 (4)	30	Zr ⁹⁵	65 »
1250 (5)	11	—	—	724 (4)	120	Zr ⁹⁵	65 »
1220 (5)	14	—	—	695 (4)	200	Ce ¹⁴⁴	284 Days
1163 (3)	74	2186—1022	284 Days	661,6 *	1050	Cs ¹³⁷	30 Years
1120 (5)	13	Ru ¹⁰⁶	366 Days	624 (4)	110	Ru ¹⁰⁶	366 Days
		Te ¹²⁹	41 Days	604 (4)	50	Cs ¹³⁴	2.07 Years
1075 (5)	13	—	—	513 (4)	180	Ru ¹⁰⁶	366 Days
1040 (4)	40	Ru ¹⁰⁶	366 Days				

Remark. Asterisks denote γ -lines used as references. The energy of the 1163-keV line was determined by using a Co⁶⁰ source. Errors are in parentheses.

The germanium detectors used in this work were fabricated at the I. V. Kurchatov Institute of Atomic Energy. p-Type lithium-drifted germanium was used. The detectors were placed in a special cryostat on a copper rod cooled with liquid nitrogen. Absorbents such as zeolite and silica gel with palladium aided in maintaining a high vacuum in the cryostat. Two detectors were employed in the work: the first detector was 3 mm thick, 14 mm in diameter, and had an operating voltage of 300 V; the second detector was 8 mm thick, 19 mm in diameter, and had an operating voltage of 850 V.

The circuit of the low-noise preamplifier is basically similar to the one described in [8]. The relationship between the input capacitance noise of the preamplifier is of the form

$$\text{HPW(keV)} = 1.8 + 0.05C \text{ (pf)},$$

where HPW denotes the width at half the peak height of the instrumental line. The spectrometer resolution at the preamplifier input self-capacitance 14 pf and 17 pf is 4 keV, for both detectors, at the Cs¹³⁷ 661 keV line.

Figure 1 shows the Co⁶⁰ γ -spectrum as measured by the 8-mm thick detector. The stability of the analyzing instruments was about 0.2% in 1 h at 661 keV.

The fuel element γ -spectrum measured with the 3-mm and 8-mm thick detectors can be found in Figs. 2 and 3. The energy and intensity of the fission fragment γ -lines are tabulated. Note the sharp discrimination of the Cs¹³⁷ 661 keV γ -line. This means that the germanium semiconductor spectrometer is capable of nondestructive burnup testing (and for the particularly crucial case where the fuel-element performance history is obscure).

A Na²² source of known intensity was employed to find the absolute intensity of the 661 keV Cs¹³⁷ γ -emission line. Fuel depletion was ~6% as determined by this method.

Note also that the use of the germanium detector makes it possible to discern a large number of γ -lines in the fuel element spectrum. This number can be increased still further by obtaining better statistics in the spectrum scan, and by varying the irradiation time and cooling time of the fuel elements.

Once the intensities of these lines are known, we can determine the yields of the corresponding fission fragments and the content of various impurities of other elements in the fuel element. But this goes beyond the scope of this article.

Information has appeared recently [9] on distortion of the Cs¹³⁷ content distribution in fuel elements through migration of the Cs¹³⁷, and this appears to restrict the use of this isotope in burnup determinations.

LITERATURE CITED

1. N. Rassmussen et al., Report RNR/39, IAEA Vienna Symposium (1960).
2. J. Rochlin et al., Third Geneva International Conference on the Peaceful Uses of Atomic Energy, P/416 (1964).
3. L. V. Groshev and A. M. Demidov, Atomnaya Énergiya, 13, 458 (1962).

4. T. Owen, Brit. J. Appl. Phys., 14, 456 (1963).
5. W. Diggle and W. Blackader, Nucleonics, 23, No.3, 71 (1965).
6. M. Higsberger et al., Third Geneva Conference on the Peaceful Uses of Atomic Energy, p.399 (1964).
7. M. Higsberger et al., Nucleonics, 23, No.1, 32 (1965).
8. V. G. Brovchenko and Yu. D. Molchanov, Pribory i Tekhnika Éksperimenta, No.2, 5 (1964).
9. W. McGonnagle, Report SM-67/46, IAEA Symposium on Administrative and Nuclear Materials Management Problems, 1965. Vienna, IAEA (1965).

FLUORITE ACTIVATION ANALYSIS ASSAY IN ORE SAMPLES AND IN ORE BENEFICIATION PRODUCTS

V. I. Prokopchik and T. I. Subbotina

UDC 543.53:539.172.4

Fluorine content in fluorite ore samples and in fluorite concentrates and products can be assayed by activation analysis using the nuclear reaction $F^{19}(n, \alpha)N^{16}$ [1]. The energy threshold of this reaction is 1.57 MeV [2], and the effective cross section is 260 mb at 6 MeV neutron energy [3].

The nuclide N^{16} ($T_{1/2} = 7$ sec) emits 6.13 MeV γ photons (55%) and 7.11 MeV γ photons (21%) as it decays. The effect of gammas emitted by Al^{28} ($E\gamma = 1.79$ MeV) formed in the reaction $Si^{28}(n, p)Al^{28}$ is counteracted by discrimination at the 2 MeV level. The oxygen reaction $O^{16}(n, p)N^{16}$ occurring in activation using a polonium-beryllium source can be neglected, since the energy threshold of this reaction is 10.22 MeV [2].

Records of γ emission at higher than 2 MeV energy thus provides us with readings proportional to the number of F^{19} nuclei present in the activated sample.

A laboratory arrangement devised for fluorite activation analysis now makes it possible to irradiate samples in sequence, using fast flux from a polonium-beryllium source, and then to swiftly transfer the samples to a detector and record the γ emission there.

The measuring equipment included a scintillation counter (NaI crystal, Tl-activated, 40 by 50 mm in size, with FÉU-13 photomultiplier tube), integrated pulse-height discriminator, and scaler. The neutron source had a capacity of 30 to 200 neutrons/sec.

Samples for analysis, weighing 200 to 500 g, are placed in shaped plastic cuvetts (Fig. 1).

The activation analysis cycle involves activation (42 sec), transfer of the sample (3 sec), and measurement (30 sec). Roughly 70% of the radiation is measured, of the amount available for activation measurements up to the saturation level. Five cycles are run to enhance the precision of the analytical procedure. This stretches the total analysis time to 7-8 min for one sample. Measurements show the relationship between the recorded γ -ray intensity and fluorite content to be a linear relationship over the 0 to 100% CaF_2 range.

Fluorite content in the samples is given by the formula

$$C_t = C_s (N_t P_t / N_s P_t),$$

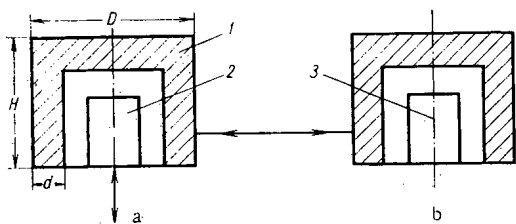


Fig. 1. Schematic diagram of sample during irradiation (a) and measurement (b): 1) cuvet with sample ($D = 91$ mm, $H = 65$ mm, $d = 12$ mm); 2) neutron source; 3) γ -ray counter.

where C_t and C_s are respectively the percentage fluorite content in the test samples and standard samples; N_t and N_s are the number of pulses recorded (background subtracted) when the test sample and standard sample are measured respectively (in pulses per 150 sec); P_t and P_s are the respective weights of test sample and standard, in grams. A carefully analyzed sample was used as the standard. Cuvets were filled completely in each case to keep the geometry of the measurements consistent.

The sensitivity threshold of the analysis is given by the formula

$$L_{\min} = (2 \sigma_b / K, Q, P) \% CaF_2,$$

Translated from *Atomnaya Énergiya*, Vol. 21, No. 5, pp. 415-417, November, 1966. Original article submitted April 11, 1966.

Comparison of Results of Activation Analysis and Chemical Analysis for Fluorite

CaF ₂ content, %	Activation analysis								Chemical analysis			
	3·10 ⁶ to 6.4·10 ⁶ neutrons/sec source				18·10 ⁶ to 20·10 ⁶ neutrons/sec source				number of measure- ments	Average CaF ₂ con- tent, %	rms error in mea- surements, % CaF ₂	relative rms err- or, %
	number of measure- ments	Average CaF ₂ con- tent, %	rms error in mea- surements, % CaF ₂	relative rms err- or, %	number of measure- ments	Average CaF ₂ con- tent, %	rms error in mea- surements, % CaF ₂	relative rms err- or, %				
0-5	19	2.9	0.51	18.3	30	1.9	0.26	13.8	30	3.0	0.36	12.1
5-15	21	9.4	0.74	7.8	14	10.2	0.71	6.9	12	8.0	0.46	5.8
15-50	52	28.6	1.16	4.1	35	25.6	0.79	3.1	9	34.0	0.82	2.4
50-100	13	72.9	1.31	1.8	-	-	-	-	7	61.2	0.71	1.2

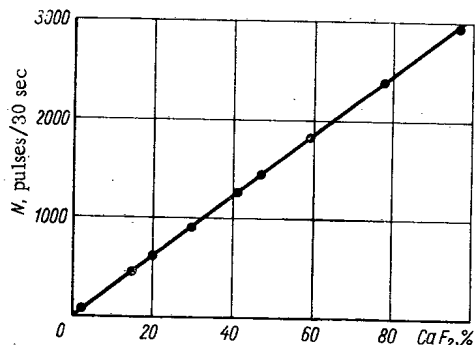


Fig. 2. Number of pulses recorded plotted versus fluorite content in samples.

where σ_b is the rms error in the background determination, in pulses per 150 sec; Q is the neutron source capacity, $\times 10^6$, in neutrons/sec; K is the number of pulses recorded in 150 sec when a sample weighing one gram and containing 1% CaF₂ is activated by a 10^6 neutrons/sec source in the activation-measurement cycle indicated above; and P is the weight of the sample, in grams.

A sensitivity threshold at 0.2% CaF₂ was obtained with this procedure when using a $20 \cdot 10^6$ neutrons/sec source, and a 0.5% CaF₂ threshold when using a $5 \cdot 10^6$ neutrons/sec source.

Statistical treatment of the results of two-stage analyses, using activation and chemical techniques (see table), shows that the results of the activation assay yield very little in the way of precision to results of chemical analysis, while the speed of the activation analysis technique is far superior.

There were no systematic discrepancies between results obtained by the two rival methods. The accuracy of the activation analysis can be improved slightly by automating the performance of the analytical equipment, and by optimizing the activation-measurement cycle.

Calculations show the optimum cycle to be one in which activation and measurement are extended 14 sec each with a 2 sec sample-transfer pause in-between. 12 such optimized cycles can be carried out in the time it takes to complete five cycles by the approach described above, and the total number of pulses recorded ends up 1.7 times higher than in the first case. Statistical error is reduced 1.3-fold in the bargain.

Special studies showed that a change in the actual composition of the samples, particularly a rise in lead content from 0 to 50%, has practically no effect on the results.

Activation analysis can be used successfully in a large number of analyses. It provides reliable accuracy with high reproducibility of results and lower cost than chemical analysis.

The authors are indebted to A. P. Bushkov and V. L. Shashkin for their kind assistance.

LITERATURE CITED

1. O. Anders, *Anal. Chem.*, **33**, 1706 (1961).
2. R. Rochlin, *Nucleonics*, No. 1, 54 (1959).
3. J. Marion and R. Brugger, *Phys. Rev.*, **100**, 69 (1955).

VAPOR-PHASE CHROMATOGRAPHIC SEPARATION AND
 GAMMA-RAY SPECTROMETRIC ANALYSIS OF GASEOUS
 EFFLUENTS OF THE VVR-M REACTOR

V.A. Solov'ev, O.V. Stepanets,
 and V.D. Trenin

UDC 621.039.58

Some lines of research call for data on the content of radioactive argon, krypton, and xenon isotopes frequently present in trace concentrations (below 10^{-7} vol. %) in the research object. Gamma-ray spectrometric and mass spectrometric analysis of multicomponent mixtures of radioactive inert gas isotopes have been made a lot easier in preliminary separation of the gas mixture. A simple and comparatively rapid gas chromatographic procedure for separating inert gas fractions for subsequent gamma-ray spectrometric analysis has been worked out at the reactor facility of the A. F. Ioffe Physics and Engineering Institute, USSR Academy of Sciences. This procedure has been applied to qualitative and quantitative determinations of the composition of the reactor gaseous effluent streams.

The chief components of the gas chromatography arrangement are the gas chromatographic adsorbent column, detectors sensing heat conduction or radioactivity, and a device for injecting gas samples into the column and removing them at the column exit for gamma-ray spectrometric examination (Fig. 1). Helium, from the cylinder 1, is employed as the sweep gas, and sweep flowrate is controlled by a pressure reducing valve 2 and check valve 3. The gas mixture is separated in a gas chromatographic column 7 made of glass U-bends with a total length of 4 meters and diameter of 4 mm; the glass tubing is filled with type 5A molecular sieves of Soviet manufacture. The grain size of the molecular sieves is 30 to 50 mesh. The molecular sieves are activated, before being charged into the column, by heating at $\sim 450^\circ\text{C}$ for 3h, and are later heated at 180°C after removal from the column in an inert gas stream, for 2 h. A meter long silica gel-packed column 6 is placed upstream of the column with the molecular sieves in order to trap moisture and aerosols.

Macroconcentrations (from 0.1% up) of the separated gases are sensed by the heat conduction detector 4, and trace concentrations of the radioactive gases are sensed by the radioactivity detector 8. The signal from the heat conduction detector is presented to the automatic recorder 15. Pulses from the

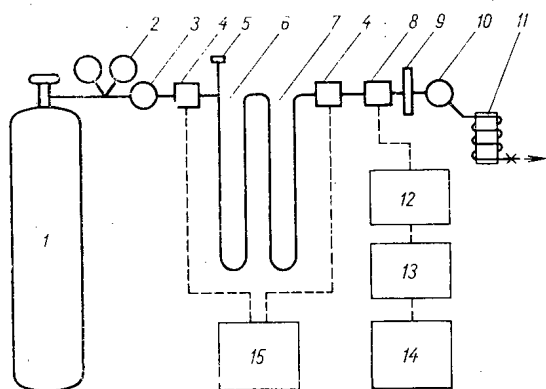


Fig. 1. Diagram of gas chromatography arrangement.

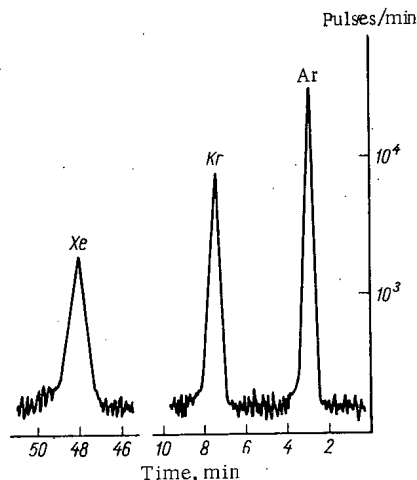


Fig. 2. Radioactivity chromatogram.

Translated from *Atomnaya Énergiya*, Vol. 21 No.5, pp. 417-418, November, 1966. Original article submitted November, 11, 1965; revised August 20, 1966.

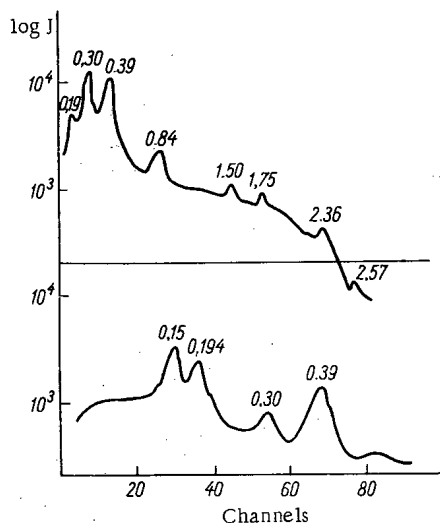


Fig. 3. Instrumental gamma-ray spectrum of krypton isotopes (log J is logarithm of number of pulses in channel of pulse height analyzer).

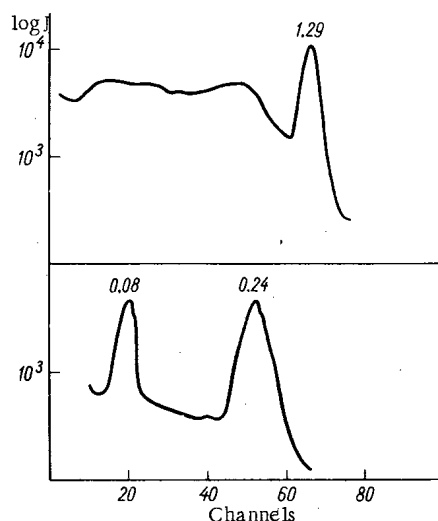


Fig. 4. Instrumental gamma-ray spectrum of argon isotopes (top-curve) and xenon (bottom curve).

radioactivity detector are passed through the scaler 12 and integrator 13 to the recorder 14. The gas-chromatography column and the heat conduction sensor are in thermostat enclosures. The sweep flow-rate is monitored with a froth measurement device 9.

The procedure for separation of the gas mixture was first elaborated to handle macroconcentrations (ranging 1 to 10 vol. %) of the components in question. The most efficient separation was obtained at a helium sweep rate of 100 ml/min.

Below, we list the retention time found for several components:

Gas analyzed	Retention time, min
H ₂	1.5
O ₂	3.0
Ar	3.0
N ₂	5.5
Kr	7.5
Xe	48.0

It is quite apparent from these data and chromatograms that excellent separation of all the constituent gases, with the exception of the argon-oxygen separation, was achieved. One reason for the failure to separate argon and oxygen is that the half-lives of the oxygen isotopes are very short and interfere with gamma-ray spectroscopic analysis of argon. The gas chromatographic separation was carried out at room temperature (~ 20°C).

The samples of radioactive gas were injected into the column in 3 ml batches. The chromatogram recorded by the radioactivity sensor (Fig. 2) revealed complete agreement in the retention times of trace quantities and macroscopic quantities of these gases.

Separated fractions were led to polyvinyl chloride tube vessel 3 m long and 4 mm in tube diameter. The fractions were sampled for radioactivity at the time the peak appeared on the chromatogram. A three-way directional valve 10 (Fig. 1) was employed to fill the PVC tube vessel 11 with argon, krypton, and xenon successively without interrupting the separative process.

The vessels of PVC tubing were wound on polyethylene cores which later enclosed the crystal (40×40 mm) of the gamma-ray spectrometer; this approach improved the efficiency in recording gammas emitted by the gases under analysis. An absolute sensitivity of 10^{-12} Ci/ml was reported in the gamma-ray spectrometer determination of the activities of those gases.

Gamma-ray spectra of argon, krypton, and xenon isotopes appear in Figs. 3 and 4. Not a single gamma-ray spectrometer detected gamma emission lines belonging to isotopes of other elements, a clear indication of the purity of the gas chromatographic separation. Each isotope was identified from the energies of photopeaks in the spectra and from the half-lives. The nuclides A^{41} , Kr^{85m} , Kr^{87} , Kr^{88} , Xe^{133} , Xe^{135} were detected.

The gas chromatographic separation of trace concentrations of radioactive gases through the use of Soviet-made type 5A molecular sieves opens the way for a comparatively rapid and clean separation of trace concentrations of carrier-free radioactive gases. Similar procedures [1-3] developed for efficient separation in minimum time involved heating the columns, greatly increasing the sweep gas speed, or carrying out the separation at temperatures far removed from room temperature.

The authors are indebted to K. A. Konoplev for his invaluable remarks on the method, and to Yu. P. Grigor'ev for his kind assistance.

LITERATURE CITED

1. R. Koch, G. Grandy, *Nucleonics*, 18, 76 (1960).
2. R. Koch, G. Grandy, *Anal. Chem.*, 33, 43 (1961).
3. R. Aubean et al., *J. Chromatog*, 6, 209 (1961).

NEWS OF SCIENCE AND TECHNOLOGY

ALL-UNION CONFERENCE ON PHASE DIAGRAMS
OF METALLIC SYSTEMS

I. A. Markova

A conference on phase diagrams of metallic systems viewed as the theoretical basis for alloy development in sophisticated industrial techniques was held June 7-9, 1966 in Moscow at the A. A. Baikov Institute of Metallurgy of the USSR Academy of Sciences. Over 250 metallurgists representing almost 60 organizations from 16 different cities throughout the Soviet Union participated in the conference.

The principal reports, which will be included in a specially published collection of articles, constitute reviews of published phase diagrams of refractory metals base systems (groups IV A, V A, VI A, rhenium, rare earths, platinum, the light metals). Some of the papers give results of construction of ternary state diagrams of either practical or theoretical interest [tungsten - molybdenum - zirconium (titanium), tungsten (molybdenum) - zirconium - titanium, aluminum - beryllium - magnesium, etc.]. Theoretical problems and experimental techniques for investigating phase diagrams of metallic systems were also taken up in the papers.

Papers on study of phase diagrams sketched out the general regularities observable in the formation of solid solutions, chemical compounds, as affected by the position of elements in Mendeleev's Periodic Table, and by the electronic structure of the constituent atoms. The required determination of the most important mechanical, physical, magnetic, electrical, and miscellaneous physical properties at room temperature and elevated temperature, so useful in compiling phase diagrams, at the same time provides information on practically important characteristics of alloys, and in the process facilitates the development of new materials for various applications in new and advanced techniques.

Academician I. V. Tananaev drew attention, in his introductory remarks, to the excellent timing of this conference on phase diagrams of metallic systems, which constitute the basis of physicochemical analysis, and, in the definition given by N. S. Kurnakov, directly relate the properties of the materials investigated to their composition. The new requirements imposed on physicochemical analysis necessitate the development of new research methods, improvements in technical equipment, deeper theoretical knowledge of fundamentals, and closer ties with the production line.

The conference saw as its task a critical review of phase diagrams for systems based on metals of industrial importance, in the light of the needs felt by different branches of industry for new metallic materials with a specified set of physical, chemical, technological, and operational properties.

Yu. F. Efimov devoted his report, "Phase diagrams of vanadium binary systems," to an investigation of phase diagrams of refractory metals of the V A and VI A groups: vanadium, niobium, tantalum, chromium, molybdenum, and tungsten. E. M. Savitskii and A. M. Zakharov presented "Phase diagrams and basic research trends in the creation of new niobium alloys." I. A. Tsyganova and M. A. Tylkina presented "Phase diagrams of tantalum," I. I. Kornilov, L. I. Pryakhina, and R. S. Polyakova presented "Chromium, molybdenum, and tungsten phase diagrams," containing a survey of data reported by both Soviet and foreign authors on the physicochemical interaction of the three metals. Features of the phase diagrams of those metals were demonstrated as functions of the position of the second component in the periodic table, on the basis of analysis of the available experimental data, and basic trends in future research designed to seek out new production alloys with special properties were singled out (properties of interest include refractoriness, thermal emissivity, superconductivity, corrosion resistance, etc.). These alloys are important in meeting the needs of aviation design and rocket design, electronics, nuclear power, and other new fields. The work of E. M. Savitskii and I. I. Kornilov and associates, as well as that of V. N. Svechnikov, Yu. A. Kocherzhinskii, A. K. Shurin, V. M. Pan, and others has resulted in the compilation of phase diagrams

Translated from *Atomnaya Énergiya*, Vol. 21, No. 5, pp. 420-421, November, 1966.

for niobium with practically all other elements which, when introduced as alloying elements, are capable of contributing to refractory niobium alloys.

The conference also discussed reports on phase diagrams of beryllium, magnesium, aluminum, titanium, zirconium, hafnium, rhenium, platinum and rare earth metals. Industrial requirements in fairly high-strength and refractory alloys of minimal specific weight has prompted an expansion of research work on the creation on new magnesium base and aluminum base alloy compositions. The need has arisen to study binary, ternary, and even more complex phase diagrams of these metals with exotic metals, rare earth metals, alkali metals, alkaline earth metals, and refractory metals. A review of data on phase diagrams of magnesium base and aluminum base alloys and outlook for future research in this field can be found in detailed coverage in papers submitted by M. E. Drits et al. "Phase diagrams of magnesium base alloys" and "Phase diagrams of aluminum base alloys" are the titles. A. E. Gol'denberg et al. studied the phase diagram of the aluminum-beryllium - magnesium system. N. D. Nagorskaya took part in the discussion, presenting a review of phase diagrams of binary beryllium systems.

Metals in the IV A group (titanium, zirconium, and hafnium) and alloys based on them are now acquiring prominence in the aviation and rocket design fields, in nuclear power work, in the development of superconducting material, and in other applications, thanks to their complex of mechanical, physical, and other properties. Reports by I. I. Kornilov and P. B. Budberg, "Equilibrium diagrams of metals of the IV group: titanium, zirconium, and hafnium," by I. I. Kornilov et al., "Investigation of interaction of titanium and zirconium with oxygen," by V. Ya. Markov et al., "Investigations of phase equilibria and crystalline structures of compounds in the titanium - iron (cobalt, nickel) - silicon systems," dealt with investigations of phase diagrams of metals in the IV A group.

The interest in rhenium and rhenium alloys is due to the needs of advanced industry for materials with special physical and chemical properties (thermal emissivity, elasticity, magnetic behavior, electrical properties, thermoelectric properties, contact properties, miscellaneous), and also to the effect of rhenium on the physicomechanical properties of molybdenum and tungsten.

In a review paper, "Phase diagrams of rhenium," K. B. Povarova et al. collected an extensive fund of material on phase diagrams of rhenium alloyed with other elements, gave a critical analysis of the data they accumulated, and pointed the way to future work in this area. They also discussed the papers by O. Kh. Khamidov and E. M. Savitskii "Binary systems of rhenium and rare earths," and Yu. B. Kuz' ma et al. "Ternary systems of rhenium with transition refractory metals and with carbon." L. I. Dashevskaya reported on the interaction of rhenium with thorium, lanthanum, and praseodymium.

Phase diagrams of the platinum series and the outlook for the applications of metals or alloys based on these were examined in detail in a paper by V. P. Polyakova. Interest in platinum metals has been aroused by the need for new materials with special physical properties which will satisfy the exacting requirements of today's high-precision instrument specifications. At present, much attention is being given to ruthenium base and palladium base alloys as possible replacements for expensive and rare platinum, rhodium, iridium, and their alloys. Generalizations on the nature of the physicochemical interaction of palladium with metals of groups IV—VIII provide some useful information on the outlook for palladium base alloys.

A report by V. F. Terekhova and E. M. Savitskii, "Phase diagrams of the rare earth metals," presented a brief survey of phase diagrams of the rare earths, compiled and reported in the literature 1962—1965. The recently intensifying interest in rare earths and rare earth alloys and the development of research on the phase diagrams of these metals owes to the unique physicochemical and special properties of these metals.

The conference also discussed papers on theoretical aspects of this research, and experimental methods for constructing phase diagrams of metallic systems. Interest was shown in a report by V. S. Shtein on the possible application of electronic digital computers in phase diagram work.

An extended discussion unfolded after the conclusion of a report by V. M. Vozdvizhenskii, who used statistical techniques and relied on volume and thermal factors to derive relationships theoretically predicting the possible formation of unlimited solid solutions and the appearance of a minimum on the solidus curve, and also after reports by Yu. V. Efimov, "Some regularities in $A \rightleftharpoons B + C$ type

transformations in binary systems, " which examined the effect of the temperature factor on the basic parameters (temperature and composition) of singularities of this type of transformations in binary systems, and by B. B. Gulyaev, in which existing phase diagrams of binary systems of alloys based on some of the more abundant metals are generalized and prognoses are offered for systems which have either not been studied to date or which have received insufficient study. Delegates participating in the discussion noted that work in the theory of diagram construction and in alloy development must be deepened and expanded, and drew particular attention to the close tie between the electronic structure of metals, their phase diagrams, and thermodynamical research.

The most interesting papers on experimental research techniques were those by A. M. Zakharov on a study of quaternary phase diagrams of metallic systems using the microhardness method and by Yu. A. Kocherzhinskii on differential thermal analysis at high temperatures.

It was agreed to schedule phase diagram conferences regularly every two years, and 1967 plans call for a conference on experimental and theoretical research techniques in the study and construction of phase diagrams.

BRIEF COMMUNICATIONS

British Scientists Visit the USSR. Under the terms of an agreement on collaboration in the peaceful utilization of atomic energy, concluded between the State Committee on the Peaceful Uses of Atomic Energy of the USSR and the United Kingdom Atomic Energy Authority, a delegation of British scientists active in the field of accelerators and nuclear physics visited the Soviet Union from June 13 through June 27, 1966.

The delegation included eight scientists: E. Bretcher (who headed up the delegation), D. Allan, D. Perring, G. Diarnelly, S. Attlee (Harwell) and T. Pickavance, Walkenshaw and Manning (Rutherford Laboratory).

The British scientists visited the P. N. Lebedev Institute of Physics, the Power Physics Institute (Obninsk), the High Energy Physics Institute (Serpukhov), the Institute of Theoretical and Experimental Physics, the Nuclear Physics Institute (Novosibirsk), the Khar'kov Physics and Engineering Institute, the Research Institute for Electrophysical Equipment (Leningrad), and the Joint Institute for Nuclear Research (Dubna).

The level of research conducted by Soviet scientists and the unique facilities available to research physicists at Novosibirsk, Serpukhov, Khar'kov, and Dubna made a deep impression on the visiting British scientists.

Translated from Atomnaya Energiya, Vol. 21, No. 5, page 426, November, 1966.

BOOK REVIEWS

K. Röhrdanz, NUCLEAR ENGINEERING IN A NUTSHELL*

This popular science book has the following 11 short chapters: 1) the special theory of relativity, wave and particle dualism, and quantum mechanics; 2) physics of the atomic nucleus; 3) nuclear physics measurement techniques; 4) particle accelerators; 5) nuclear weapons and nuclear radiation; 6) nuclear reactor theory; 7) types of nuclear reactors; 8) reactor materials; 9) reactor control; 10) uses of radioactive isotopes; and 11) synthesis of nuclei.

The contents of the book cover the various fields of nuclear engineering quite fully and the treatment is concise, simple, and lucid. Each chapter cites only the basic points, laws, reactor types, accelerator types, instruments, etc. Each chapter thus manages to cover many concrete and important points in a small volume (14 to 18 pages at the most) while giving a good presentation of the particular subject. The book presents quite a few useful formulas and constants in common use. It is well illustrated with rich photographs and diagrams.

The book is written for a broad readership, with young students the primary target.

PROCEEDINGS OF THE THIRD INTERNATIONAL CONFERENCE ON THE PEACEFUL USES OF ATOMIC ENERGY. VOL. 2. REACTOR PHYSICS†

Reviewed by Yu. I. Mityaev

This volume comes in four sections, and contains papers presented at one session of the conference.

Papers in the first two sections deal with analytic and numerical methods in calculating slow neutron spectra with neutron thermalization taken into account, and study resonance neutron absorption in fast and thermal reactors, as well as treating transport theory and methods for solving the Boltzmann kinetic equation.

Neutron thermalization and methods for calculating slow neutron spectra are dealt with in review papers by G. I. Marchuk et al. (USSR) and J. Beister et al. (USA), in papers by H. Küsters (West Germany), J. Pop-Jordanov (Yugoslavia), M. Cadilnac (France), I. Purica (Poland), and partially in papers dealing with the theory and methods of physical reactor calculations (R. Naudet et al., France; E. Wachspress et al. (USA).

The theory and methods of calculating resonance neutron absorption in fast and thermal reactors may be found in papers presented by A. Abogyan et al. (USSR), J. Chernick and M. Levine (USA), and J. Codd et al. (Britain).

* Würzburg, Vogel-Verlag, [in German], 120 pages (1964).

† United Nations, N. Y., 443 pages (1965).

Translated from Atomnaya Énergiya, Vol. 21, No. 5, pp. 427-432, November, 1966.

Several review papers and original contributions were devoted to neutron transport theory and to various methods for solving the transport equation. These include papers by J. Bell et al. (USA), S. Ermakov et al. (USSR), and scientists from Austria, Poland, and Czechoslovakia. The first two sections include papers by British specialists on methods for calculating temperature fields and power distribution fields in a three-dimensional reactor, a paper by the Hungarian scientist L. Pál on the statistical theory of nuclear chain reactions, and two papers on probabilistic determinations of several physical reactor characteristics.

Methods and results of experimental research on some characteristics of multiplying and non-multiplying systems are found in the papers grouped in the third section. These are papers by V. Mostovoi's team (USSR) on neutron thermalization in uranium-water reactors, by E. Doil'nitsyn et al. (USSR) on neutron thermalization in hydrogenous media, a review of experimental methods employed in France in thermal reactor investigations (D. Breton and P. Lafore), and also papers on scattering cross sections and diffusion characteristics of organic substances (L. Pal et al., Hungary; S. Hoki et al., Japan), zirconium hydride, ordinary water and heavy water (T. Springer et al., West Germany), slowing-down properties of water and other hydrogenous substances (L. Yurov et al., USSR; U. Dahlborg et al., Sweden). A review paper by W. Murgatroyd et al. describes reactor physics experiments conducted in British universities. Two papers discuss a pulsed method for studying neutron thermalization and neutron diffusion.

The papers appearing in the concluding section of the volume are concerned with nuclear physics constants. Papers by E. Roe et al. (Britain) and N. Mateescu (Rumania) cite results of a determination of the nuclear constants of U^{238} , U^{235} , iron, and water, and discuss the temperature variation of neutron scattering cross sections of heavy water, while papers by L. Maiorov et al. (USSR), G. Cecchini et al. (Italy), and M. Humi et al. (Israel) describe methods and programs for computing slow neutron group constants and methods for determination of systems of group constants based on integrated measurements.

Acquisition, processing, and dissemination of information on nuclear physics constants for reactor calculations are the subject material of papers by C. Westcott et al. (IAEA) and J. Story et al. (Britain).

All the papers were published in one of the four conference working languages (Russian, English, French, Spanish) with abstracts in the other three languages.

A. B. Clegg, HIGH ENERGY NUCLEAR REACTIONS*

This book, written by the director of the nuclear physics laboratory at Oxford University, forms part of the well-known "Oxford Library of the Physical Sciences" series. The compact monograph consists of seven chapters, a small appendix (with the mathematical derivation of some formulas used), a list of pertinent literature (113 titles) and a subject index. The short introduction (Chapter 1) is followed by a description of the principal aspects of the mechanism underlying nuclear reactions (Chapter 2) and a brief report on the potentialities inherent in different experimental techniques (Chapter 3). The next three chapters analyze elastic collisions (Chapter 4), inelastic collisions (Chapter 5), and nucleon knockout reactions (Chapter 6), in detail. The book ends with the short (Chapter 7) on star formation reactions. Particular attention is given to the possibility of studying the structure of atomic nuclei on the basis of results of observations of reactions of the types described at high particle energies (on the order of 100 MeV and higher).

* Oxford, Clarendon Press, VIII + 130 pp. (1965).

D. C. Layman and G. Thornton. REMOTE HANDLING OF
MOBILE NUCLEAR SYSTEMS *

Reviewed by M. Orlov

Various portable or transportable nuclear facilities requiring not only remote control but also complex equipment for remote servicing and maintenance, remote-controlled rigging and dismantling operations, have been built in recent years. This book by D. Layman and G. Thornton, of unusual interest, is intended, in the authors' view, to show practical applications of remote operation of a direct air cycle nuclear propulsion engine.

In the first chapter, the authors outline the essence of the direct air cycle nuclear propulsion engine project developed by the board of aviation nuclear engines of General Electric. Photographs, models of nuclear turbojet engines of both single (XNJ14OE) and twin (XMA-1) types, are presented, critical assemblies (HTRE-I, II, III), planning and functions of various test installations at the Idaho national testing station (USA) are discussed.

The next five chapters discuss various technological processes for complete remote assembly and dismantling of a nuclear reactor, of shielding, of a turbojet engine and its subassemblies into distinct and easily transportable modular units. Designs of various devices for extracting fuel elements from the reactor, supporting stands, assembling and disassembling rigs, turntables, and platforms are presented. General-purpose and special-purpose mechanisms and instruments are described in detail: manipulators of different designs, viewing and observation systems (viewing windows, binoculars, periscopes, conventional and stereoscopic television circuits); automatic shielded doors and barriers; a variety of mechanical equipment (mechanical and pneumatic wrenches, shears, cut-off abrasive grinding wheels, etc.), and mobile equipment for transportation of nuclear facilities cross-country or within the confines of machine and assembly shops in testing stations (locomotive with special radiation shielding, automotive cranes, shields, "Crab" type cabs, booths, rigs equipped with manipulators and a variety of observation systems). Appropriate methods are presented, and materials are recommended for deactivation of equipment, plants, floor and wall coatings. The technique and practice of collection, hauling, and disposal of radioactive wastes is described.

The seventh, eighth, and ninth chapters offer data on the physical fundamentals of radiation safety, on the properties of radioactive radiations, and on capture cross sections, fission products, and shielding calculations.

A description of a wall-type beam crane, the 550 model manipulator, instructions for installing manipulator assemblies in hot caves, instructions for handling remote-operated electrical connectors, calculations of induced activity, and dose rate determinations in buildings and shielded enclosures at the Idaho national testing station fill five appendices at the end of the book.

The book familiarizes specialists on the operation and planning of different atomic facilities with the techniques and methods of remote maintenance of radiation-hazard equipment and plant installations, and with several concepts on the design of remote control accessories and their technical potential.

Each chapter in the book features photographs, diagrams, nomograms, and a bibliography.

*Oak Ridge (Tennessee), USAEC Division of Technical Information Extension, 649 pages (1966).

CRITICALITY CONTROL OF FISSILE MATERIALS *

Reviewed by Yu. K.

IAEA has published a collection of material presented at the criticality control symposium held in Stockholm, November 1-5, 1965. 45 papers were presented at the symposium, and are grouped here under the headings: "Basic data," "Theoretical research," "Experimental research," "Special problems," "Design and operation of facilities," "Existing criticality control practice," "Determination and prevention of criticality accidents."

The record of the discussions on these topics is presented. The symposium materials cover practically all aspects of criticality, from initial data for calculations all the way to administrative and juridical questions. The first symposium on this topic dates back to 1961. Significant progress in this area has been achieved in the time elapsed from the first 1961 symposium till the Stockholm symposium, of course, so that the proceedings of the 1965 symposium are more voluminous.

The attention given to criticality of nuclear fuel reprocessing plants is typical of the symposium's work, and is traceable to the universal interest in a closed nuclear power fuel cycle. One distinguishing feature of most of the material in the symposium is the practical approach, the engineering side predominating in the discussion.

On the whole, the symposium will be unquestionably useful to a wide range of specialists on safety in handling critical masses of fissible materials.

RADIOISOTOPE INSTRUMENTS IN INDUSTRY AND GEOPHYSICS †

Reviewed by L. P.

A symposium was held in Warsaw, October 18-22, 1965, on applications of radioisotope instruments in industry and geophysics. The symposium was organized by IAEA with the collaboration of the Polish government. 222 specialists from 23 countries and three international organizations took part in the proceedings.

59 scientific papers were read and discussed; four of these were tutorial review presentations. The first volume groups together those papers devoted to the development and application of radioisotope devices in various branches of industry. Close attention is given to discussion of the design and utilization of radioisotope devices to analyze the composition of matter based on the use of isotope sources, secondary x-radiation caused by fluorescence. J. Rothery (USA) pointed out the possibility of gaining significant yields of characteristic and monoenergetic x-radiation in work with α -sources, in his paper "Advances in the USAEC program on radioisotope device development." Information was also given on the development of a device utilizing a tritium bremsstrahlung x-ray source to determine iron content in ocean bottom rock samples. Excellent agreement between results found by this method and results of fast-neutron activation analysis was demonstrated.

* Vienna, IAEA, 757 pages (1966).

† Proceedings of a symposium, Warsaw, October 18-22, 1965. Vienna, IAEA, Vol. I, 575pp; Vol. II, 477pp, 1966.

Development of a gold content determining instrument, in which Xe^{133} emitting 0.08 MeV gammas is used as a radiation source exciting x-radiation characteristic of gold in objects containing gold on the surface, has been completed.

The volume of work carried out in Japan in the design of equipment for analyzing the composition of matter through the use of isotope radiation sources is quite striking. A report by S. Enomoto et al. demonstrated the possibility of raising the intensity of x-ray K-emission of chromium, iron, and nickel by a factor of 8 to 12, when β -radiation is used to excite the K-radiation. K. Uchida et al. described an industrial-scale equipment for simultaneous quantitative analysis of a mixture of raw material used in cement production to assay content of magnesium, aluminum, silicon, iron, and calcium.

J. Rhodes et al. (Britain), J. Niwodniczanski (Poland), and A Dearnley (Britain) reported on devices for determining copper content in alloys and ores, in their papers.

A paper presented by M. Stoeppler et al. (West Germany) described the design of a device for continuous analysis of the composition of effluent gases for SO_2 , HCl, and Cl_2 content. A tritium radiation source is used, and fluorescent x-radiation is recorded by proportional counters.

J. Robin et al. (France) presented the results of laboratory investigations showing that in which zinc sulfide was added to paper pulp in the preparation of postage stamps ("Application of x-ray fluorescence in automation of postal sorting work"). By irradiating envelopes carrying postage stamps containing zinc, the characteristic 8.6 keV K-emission of the zinc is excited by bremsstrahlung by Pm^{147} isotope source and is recorded by a proportional counter. The collimation center is designed so that the postage stamp can be located on a 60 mm \times 40 mm area with a probability greater than 99%. Use of this device makes it possible to raise and rotate the envelopes in such a way that all addresses are lined up in the same position, and the sorting speed can be brought up to 10,000 letters an hour.

H. Miwa et al. (Japan), and J. Cavallier et al. (France) reported on devices for continuous monitoring on the thickness of zinc plating on steel. In the first case the thickness of the plating was determined by recording changes in the intensity of reflected β -radiation by means of compensated ionization chambers and platings in the 5 to 20 mg/cm² thickness range are measured to within ± 0.4 mg/cm². In the second case, an Am^{241} bremsstrahlung source exciting zinc K-radiation is employed, and the K-radiation is recorded by a proportional counter, so that zinc platings 10 μ and 50 μ thick are monitored continuously at a speed of 1 meter/sec.

Several papers dealt with devices designed for automatic analysis of aqueous suspensions and dry powers, uranium and plutonium content determinations in slurries, etc.

V. Mott et al. (USA) reported the use of equipment incorporating neutron sources to determine hydrogen content in hydrocarbons. M. Beresz (Hungary) reported the use of neutron activation analysis in studies of manganese-bearing ores.

Radioisotope devices for hydrologic research were discussed in papers by G. Papadopoulos et al. (USA) and by T. Florkowski and J. Cameron (IAEA).

A facility continuously analyzing the composition of matter moving on a conveyor belt was described in a paper by T. Martin et al. (USA). It consists of a Cockroft-Walton neutron generator, fast neutron recording equipment, spectrometers, and data processing and analyzing equipment. Results of an experimental check run on this facility to determine the content of carbon, oxygen, aluminum, and silicon in coal were cited. M. Nagy and K. Varga (Hungary), A. Trost (France) and J. Rhodes et al. (Britain) presented results of their work on development of radioisotope devices to determine ash content in coal.

Six papers presented by specialists from Austria, Hungary, Canada, West Germany, and Poland dealt with the development of radioactive gages for measuring thickness, density, and liquid level and level of granular bulk materials. One interesting instrument gages the thickness of synthetic fibers (developed by Atomic Energy of Canada Ltd.). The method is based on recording the intensity of x-radiation scattered from a bundle of short fibers. The relative precision in the measurements is 1 to 4 mg/cm, which is $\pm 1\%$ of the amount gaged.

The second volume contains 26 papers on the development and use of radioisotope instruments for geophysical research, or for exploration and mining of minerals; 12 papers in this group were contributed by Soviet specialists. Papers by K. Tittle (USA) and F. A. Alekseev (USSR) gave a review of application of radioisotope instruments in the USA and the USSR. D. Kozhevnikov (USSR) discussed

the status of theoretical research in nuclear geophysics in the USSR, and R. Caldwell et al. (USA) reported on research on theoretical and experimental models with the object of determining shot-hole parameters in neutron lifetime logging. Sh. A. Guberman et al. (USSR) presented results using the theory of similitude in studying radiation transport processes; S. A. Denisik et al. (USSR) gave an account of Monte Carlo solutions of several problems in nuclear geophysics.

A paper by F. A. Alekseev, D. F. Bespalov et al. (USSR) described a pulsed neutron generator fabricated in quantity production in the USSR, and discussed its potential use, while a report by A. V. Antonov et al. (USSR) communicated results of use of the IGN-1 generator to determine the diffusion parameters of rocks and ore fluids. Papers submitted by USSR scientists (E. M. Filippov, K. I. Yakubson, K. Eife, A. Blyumentsev et al.) presented several procedures for utilizing neutrons in rock assay.

Papers by P. Dodd, R. F. Drullard (USA), "Logging system and computer program for determining density of rock in uranium occurrences," J. Czubek (Poland) and G. Gitton (France), "Gamma-gamma logging in determining density of uraniferous ores at occurrences, and by J. Czubek, "Physical potentialities of gamma-gamma logging techniques," handled different aspects of the application of this logging method to exploration and development of uranium deposits.

S. Sano and H. Kanaya (Japan) reported on the use of radioactive standards in observations of partial rock compression. M. Izvekova et al. (USSR) discussed the use of data obtained with nuclear geophysics computer-oriented research programs to locate oil-bearing strata. A paper by V. V. Larionov and M. D. Shvartsman (USSR), "Natural radioactivity of carbonate rocks," showed the relationship between uranium content, thorium content, potassium content, and content of their derivatives to the clayiness of carbonate rocks, while A. K. Berzin et al. (USSR) discussed several physical prerequisites for selective analysis of the content of distinct elements in rocks and ores.

Three papers discussed possible errors in measured density and humidity data obtained with radioisotope devices; four reports dealt with designs of various radioisotopes devices measuring the physical characteristics of soils.

Review papers worthy of special note are "Application of radioisotope instruments in USSR industry" by P. S. Savitskii, "Review of radioisotope device designs and applications in industry" by C. Clayton (Britain) and G. Cameron (IAEA), and "Fabrication and future developments in the production of quantity-manufactured radioisotope source instruments" by S. Margolin (France).

RADIOISOTOPE SAMPLE MEASUREMENT TECHNIQUES IN MEDICINE AND BIOLOGY*

Reviewed by Yu. V. Sivintsev

This is a collection of the proceedings of the IAEA Vienna May 1965 conference on radiometric methods in medicine and biology. 54 papers (most of them in English, but nine in French and one in Russian) are distributed over eight sections.

Section 1 deals with γ -ray spectrometry, and contains 11 papers. A high-sensitivity multidimensional γ -ray spectrometer is described by J. Nielson and W. Kornberg (USA). This spectrometer makes fast work of measuring levels of radioactive contamination of biological samples commonly

* Vienna, IAEA, 724 pp. (1965).

encountered in today's practice (levels below 1 decay per minute per kg), or measuring the content of a large group of elements in the tissue and in blood by activation analysis (concentrations on the order of $10^{-4}\%$). A paper by V. Gwynn (USA) reported determinations on trace amounts of γ -ray emitters reliable recorded by NaI(Tl) crystals of different sizes. G. Warde et al. presented data on radioactive fallout measured in the USA from 1962 through 1965. V. Jackson (Canada) reported a simple method for stabilizing an analyzer when recording low-energy quanta (below 100 keV). Highly sensitive methods employed in measuring Co^{60} and $\text{Ag}^{110\text{m}}$ in marine organisms and $\text{Na}^{24}/\text{Na}^{22}$ ratio in ion transfer through biological membranes are described in papers by T. Folsom et al. (USA) and K. Wagner and M. Landmann (West Germany). γ -ray spectrometric methods for analyzing thorium present in human and animal tissues were analyzed by R. Papp (USA), and the effect of specimen volume and density on the γ -ray spectrum of the specimen was discussed by O. Kastren (Finland). I. Gallet et al. (France) described a spectrometer using a NaI(Tl) crystal 216 mm in diameter and 190 mm high placed in a well, with sensitivity around 10^{-10} to 10^{-11} curie/liter. D. Nicolesco-Tinc and T. Mateu (Rumania) described iodine radiometry techniques in isolated preparations involving the use of scintillation counters. A paper by C. Lamson et al. (USA) dealt with the design of an automatic sample changer for γ -ray spectrometry work.

Section 2 contains five papers on computer applications in spectrometer data processing. A very detailed paper by A. de Haan et al. (USA) juxtaposes different methods for analyzing mixtures of γ -ray emitters by the position of photopeaks, and an equally detailed report by compatriots V. Dearman et al. deals with half-lives of nuclides.

The next six papers (section 3) refer to activation analysis techniques and radioactive tracer methods. R. Spencer and C. Brody (USA) analyzed the possible inclusion of radioactive halogen isotopes in a variety of organic compounds. P. Mulway et al. (USA) gave an account of the sensitivity of iodine activation analysis in biological specimens, on the basis of bremsstrahlung intensity. R. Hori (Japan) evaluated sodium and potassium measurements in biological specimens, using the same method. An original method for estimating amounts of uranium in secretions from delayed neutron intensity when the specimens are exposed to thermal neutrons was described by Y. Brooks (Britain). Methods for preparing biological specimens for analysis were reviewed systematically by L. Akers (USA). S. Hyman and J. Roels (France) reported on application of activation analysis to the study of salts in human bone slices.

Section 4 contains seven papers on different aspects of instrumental radiometric techniques: automation of chromatographic analyses (F. Berthold, West Germany), of H^3 and C^{14} vapor-phase chromatography in biological specimens (H. Simon et al., West Germany), use of proportional counters in H^3 and C^{14} radiometry (R. Tykva, Czechoslovakia), radiometry of secretions for Pu^{241} assay (G. Dalton, Britain), analysis of colloidal solutions with Au^{198} and P^{32} (Y. Cohen et al., France), applications of γ -ray tracers in investigations of precipitation reactions (L. Bonev et al., Bulgaria), and a radiochemical method for Sr^{90} determinations in milk (K. Cenvar et al., Turkey).

Close attention was paid to liquid scintillator techniques at the conference (section 5). E. Bush and D. Hansen (USA) reported improved efficiency of liquid scintillation counters through optimized radiation detector compositions in H^3 and C^{14} measurements. The effect of quenching agents was analyzed by G. Rossi (USA) and T. Iwakura and Y. Kashida (Japan). A. Smith and J. Read (Britain) gave a basis for optimized liquid scintillator compositions in H^3 and Co^{57} measurements in biological samples. Ca^{45} scintillation counting methods were analyzed by T. Carr and B. Parsons (Britain). Simple C^{14}O_2 collecting apparatus for subsequent analytical work was described in a paper by K. Miras et al. (Greece). W. Müller et al. (West Germany) reported the simultaneous use of three isotopes (Ca^{45} , Sr^{85} , P^{32}) in bone metabolism research. Various liquid scintillation techniques for γ -ray emitter counts were analyzed by H. Ilom et al. (West Germany). A. Geimbach et al. (USA) reported on scintillation ion exchange resins used for the same purposes. F. Spider (USA) submitted a paper on zone scanning and autoradiographic scanning of thin-layer chromatograms.

Section 6, which is quite short, contains three papers on improved autoradiography of biological specimens and some applications.

High-precision techniques for calibration of radiometric equipment, γ -ray counters in particular, are discussed in detail in the six papers appearing in section 7.

Section 8 publishes five papers on the most vigorously developing field in γ -ray spectrometry: applications of semiconductor detectors. S. Friedland (USA) described a lithium-drifted germanium

detector spectrometer with a resolution of 3—10 keV. D. Camp and J. Armantraut (USA) reported the application of detectors of this type to spectrometry of β -particles and spectrometry of soft gammas. A. Hashisume et al. (France) compared results of β -ray spectrometry using semiconductor detectors of different types. C. Perry (Britain) analyzed the potentialities of these detectors for α -spectrometry, in applications in UKAEA plants. A paper by T. Folsom and associates (USA) dealt with analysis of trace amounts of Cs^{137} (0.05 to 20 pCi) in sea water on the basis of internal conversion electrons detected by silicon detectors.

Appendices to the book contain lists of session chairman, secretaries, and conference participants, and an index of authors.

RADIOISOTOPES IN ENDOCRINOLOGY. FIRST ANNIVERSARY OF THE
SOCIETY FOR NUCLEAR MEDICINE IN FREIBURG IM BREISGAU,
OCTOBER 17-19, OCTOBER 1963*.

This book contains the proceedings of the first annual gathering of the society for nuclear medicine (of West Germany) devoted to applications of radioactive isotopes in endocrinology. In addition to the list of conference participants and introductory remarks by the chairman, the book contains 50 papers in their original languages (most of them in German, nine in English). Most of the papers deal with I^{131} and I^{125} tracer applications in diagnosis and therapy, and methods for recording the γ emissions of these isotopes in living organisms. Application of H^3 , C^{14} , S^{35} in clinical research is described in ten papers, and some reports offer information on analysis of experimental results on calcium and strontium metabolism.

DOSIMETRY OF IONIZING RADIATIONS (BASIC CONCEPTS AND THEIR
TERMINOLOGY) USSR ACADEMY OF SCIENCES, COMMITTEE
ON SCIENTIFIC AND TECHNICAL TERMINOLOGY. COLLECTIONS
OF RECOMMENDED TERMS. NO. 70†.

This collection of recommended standard terms in the field of dosimetry of ionizing radiations contains definitions of 52 concepts with parallel renditions in Russian, English, French, and German.

* Published by G. Hoffman, F.K. Schattner press, Stuttgart, XXIV + 480 pages (1965).

† Moscow, Nauka press, 24 pages [in Russian] (1965).

The terms proposed cover general concepts, modes of ionizing radiations, parameters and characteristics of these radiations, and parameters characterizing interaction of ionizing radiations with the environment. The end of the book gives alphabetic symbols of Russian, British, French, and German, usages and terms. The terms recommended here have been passed on from the standpoint of language norms by the Russian Language Institute of the USSR Academy of Sciences, for use in scientific and technical literature, in the educational process, in standards, and in technical documentation.

J. S. Strettan. IONIZING RADIATIONS* .

This popular science book requires no special training in physics or knowledge of higher mathematics from the reader, and consists of eight chapters, a glossary of terms used, tables of the most important isotopes, a brief list of recommended literature, and authors and subject indexes. The book takes a consistent approach to the history of the discovery of ionizing radiations (Chapter 1), describes the operating principles and design of x-ray tubes (Chapter 2), and methods for generating x-radiation (Chapter 3). Analysis of the properties of x-radiation and γ -radiation (Chapter 4) is followed by a description of naturally radioactive substances (Chapter 5). Chapter 6 is devoted to techniques for measuring ionizing radiations, and Chapter 7 offers information on artificially radioactive substances. The final Chapter 8 deals with biological effects of ionizing radiations and safe methods for working with ionizing radiations.

G. W. Reed. PROCEEDINGS OF THE INTERNATIONAL "ENRICO FERMI" SCHOOL OF PHYSICS COURSE XXX - RADIATION DOSIMETRY†.

Reviewed by Yu. V. Sivintsev

This thirtieth number in the set of proceedings of the Enrico Fermi international school of physics contains the texts of a lecture course on radiation dosimetry given by leading Western specialists. The book opens with a historical review of the development of radiation dosimetry (F. Spears, Britain). Basic processes of absorption of radiation by matter are considered in the next section, sequentially for electromagnetic radiation, electrons, neutrons, and heavy charged particles (M. Ciosotto, Italy). The concept of dose and radiation dose unit are characterized briefly by G. Rossi (USA). Determination of exposure dose from ionization of a standard medium -- air -- is discussed in a thoroughgoing lecture

* Oxford-London, Pergamon Press, 180 pp. (1965).

† New York - London, Academic Press, VIII + 308 pages (1964).

by A. Allisi (France). Specific ionization dosimetry problems at high radiation intensity are discussed in a lecture by the British research scientist J. Bogg. He lectures briefly on high-pressure ionization chambers in the next lecture. The three next lectures, by G. Rossi (USA), deal with involved microdosimetry techniques (stressing LET spectral measurements), with neutron dosimetry and dosimetry of heavy charged particles, and with determination of the relative biological effectiveness of radiations. Calorimetric dosimetry is treated in two parts separately: intensity determination and absorbed dose determination (G. Laughlin, USA). This scientist also reports on solid state dosimetry (centering on luminescence techniques and the use of semiconductor detectors). N. Trott (Britain) described the range of application of scintillation dosimeters in detail. The course lays heavy stress on chemical dosimetry. This section begins with a brief rundown on information on elementary radiation-chemical reactions in water (Daynton, Britain), followed by a more detailed analysis of the principles and range of applicability of various methods in chemical dosimetry. This section also offers a lecture by A. Müller (West Germany) on paramagnetic resonance studies of radicals. Basic information on the capabilities of photographic dosimetry are treated in an exhaustive lecture by E. Casnati (Italy).

Standardization of reactive preparations by using different radiometric techniques and experimental arrangements is characterized exhaustively by N. Trott (Britain). His compatriot G. Reed gives a detailed analysis of clinical dosimetry (both internal and external exposures). F. Spears (Britain) reported results of his investigations on determination of doses absorbed by bone tissue in external exposure of humans and in incorporating of isotopes into soft tissues and skeletal bone. Tissue dosimetry of penetrating radiations was discussed in a lecture by G. Laughlin (USA). Background radiation doses are briefly characterized by F. Spears. He is also the author of a section on population exposure dose as a result of the use of ionizing radiations in medicine. The book ends with a short lecture on basic problems in radiobiology (L. Grey, Britain). Each of the lectures is, as a rule, accompanied by a list of literature, leaning heavily on articles in the periodical literature.

E. I. Vorob'ev et al. RADIOBIOLOGY AND CLINICAL RADIOLOGY.
 PROCEEDINGS OF THE CENTRAL X-RAY AND RADIOLOGICAL
 SCIENTIFIC RESEARCH INSTITUTE. VOLUME V.*

This collection of articles covers pathogenesis, therapy, and prophylaxis of acute radiation sickness (section I, 39 articles), remote radiation pathology and radiation genetics (section II, 10 articles), clinical radiology (14 articles), radioisotope diagnostics (3 articles), and x-ray diagnostics (5 articles). Experimental work centers on the biological effects of ionizing radiations on living organisms and the practical utilization of various forms of radiation in medical practice. The theoretical articles generalize upon experience and achievements of clinics of the Institute in radiotherapy of various forms of malignant neoplasms and nontumor illnesses, and they also discuss diagnostic applications of radioactive isotopes. Articles on x-ray diagnostics deal mostly with improved ways of spotting malignant neoplasms.

* Leningrad, 378 pages [in Russian] (1965).

RULES AND REGULATIONS FOR SAFE TRANSPORTATION
OF RADIOACTIVE MATERIALS. REVISED 1964 EDITION.
NO. 6 IN SERIES ON SAFETY. *

Reviewed by Petrenko

The IAEA council of directors approved the revised edition of "Rules and regulations for safe transportation of radioactive materials" in September 1964. This edition was prepared with the participation of member-nations of IAEA and interested organizations.

The introductory section contains abbreviations agreed upon. Part one (A) indicates the range of application of the rules and regulations, and reviews basic concepts and terms used in the rules. Part two (B) lists materials, instruments, and objects to which the third and fourth parts of the stated rules are not extended.

Part three (C) lists requirements for packaging and delivery of packages or crates for transportation. It specifies a classic classification of packages by groups depending on the maximum amount of radioactive material in the package, lists categories of shipping packages, requirements applying to shipping containers for low-level materials and fissionable materials, and describes labels, markings, and decalcomania required, as well as repeating some basic contents for the guidance of administrative bodies.

Rules for storage and shipping of radioactive materials are found in part four (D), and marking symbols in part five (E).

Appendix 1 presents tabular material: activity/mass ratios for uranium and natural thorium; classifications of radioactive isotopes by groups for shipping purposes; neutron flux levels equivalent to 1 mr/h dose rate as a function of neutron energy; values of maximum tolerable contamination, minimum distances from the surface of shipping packages depending on the number of packages present, the category, and the number of shipping indexes, and similar material.

The basic requirements applying to shipping aggregates are found in appendix 2; those applying to packages containing fissionable material are found in appendix 3, and rules and procedures for testing are described in appendix 4.

* Vienna, IAEA, 108 pages [Russian edition] (1965).

ERRATA

The Interaction of a Modulated Flow with Plasma by Ya. B. Bainberg and V. D. Shapiro [Soviet Atomic Energy, 19, No. 4, 1260-1267 (1965)]

WHERE FOUND	WAS GIVEN AS	SHOULD BE
p. 1261, line 12	$e^{-i\omega t}$	$e^{-i\omega t}$
p. 1261, line 19	e^{-ikz}	e^{ikz}
p. 1263, line 10	ε	ε^2
p. 1266, line 13	ω_1 and $w + kU$	$\omega_1 = \omega + kU$
p. 1266, line 27	is kU	is $\text{Im } \varepsilon \sim \Omega_1$. Formula (26) for ε is not applicable at resonance when kU

RUSSIAN TO ENGLISH

Scientist-translators wanted

You can keep abreast of the latest Soviet research in your field while supplementing your **income** by translating **in your own home** on a part-time basis. In the expanding Consultants Bureau publishing program, we **guarantee a continuous flow of translation** in your specialty. If you have a native command of English, a good knowledge of Russian, and experience and academic training in a scientific discipline, you may be qualified for our program. Immediate openings are available in the following fields: physics, chemistry, engineering, biology, geology, and instrumentation. Call or write now for additional information: TRANSLATIONS EDITOR



CONSULTANTS BUREAU

227 West 17 Street, New York, N. Y. 10011 • (Area Code: 212) AL-5-0713

SPECIFIC HEATS AT LOW TEMPERATURES

By E. S. R. Gopal

The Clarendon Laboratory, Oxford University

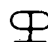
Surveys the entire field of low-temperature specific heats at a level suitable for graduate courses. After outlining the thermodynamic background, specific heat behavior (lattice, electronic, and magnetic contributions) of solids, liquids, and gases is discussed in detail. This readable and comprehensive account is kept at an elementary physical level, but full references to advanced treatments are given. Students or research workers unfamiliar with the field will find this an excellent supplementary text which functions as a bridge between basic theory and modern research work.

Considerable practical information is included on calorimetric and refrigeration problems; for example, the basic theory, tables, and supplementary information is given to enable the reader to calculate the refrigeration needed to cool any piece of apparatus to a desired point. Of special interest are six-figure tables of Einstein and Debye internal energy and specific heat functions, given in an appendix, and of use to physicists and chemists performing calculations of the thermodynamic properties of gases and solids.

CONTENTS: Elementary concepts of specific heats • Lattice heat capacity of solids • Electronic specific heats • Magnetic contributions to specific heats • Heat capacity of liquids • Specific heats of gases • Anomalies in specific heats • Miscellaneous problems in specific heats • *Appendix:* Six figure tables of Einstein and Debye internal energy and specific heat functions.

240 pages

\$11.50

 **PLENUM PRESS** 227 West 17th Street, New York, New York 10011

A DIVISION OF PLENUM PUBLISHING CORPORATION